

PLANETARY SCIENCE

The end of the lunar dynamo

Saied Mighani^{1*†}, Huapei Wang^{1,2*†}, David L. Shuster^{3,4}, Cauê S. Borlina¹,
Claire I. O. Nichols¹, Benjamin P. Weiss^{1†}

Magnetic measurements of the lunar crust and Apollo samples indicate that the Moon generated a dynamo magnetic field lasting from at least 4.2 until <2.5 billion years (Ga) ago. However, it has been unclear when the dynamo ceased. Here, we report paleomagnetic and $^{40}\text{Ar}/^{39}\text{Ar}$ studies showing that two lunar breccias cooled in a near-zero magnetic field (<0.1 μT) at 0.44 ± 0.01 and 0.91 ± 0.11 Ga ago, respectively. Combined with previous paleointensity estimates, this indicates that the lunar dynamo likely ceased sometime between ~1.92 and ~0.80 Ga ago. The protracted lifetime of the lunar magnetic field indicates that the late dynamo was likely powered by crystallization of the lunar core.

Copyright © 2020
The Authors, some
rights reserved;
exclusive licensee
American Association
for the Advancement
of Science. No claim to
original U.S. Government
Works. Distributed
under a Creative
Commons Attribution
NonCommercial
License 4.0 (CC BY-NC).

INTRODUCTION

The intensity of the present-day magnetic field across much of the lunar surface is <0.2 nT, indicating that the Moon currently does not have a global magnetic field (1). However, paleomagnetic measurements of Apollo samples indicate that the Moon once generated a core dynamo with surface field intensities of several tens of microtesla (comparable to that of Earth today) during the period 4.25 to 3.56 billion years (Ga) ago (2–7). Following this high-field epoch, the field declined by at least an order of magnitude by 3.2 Ga ago (8) and persisted in a weakened state (~5 μT) until at least 2.5 Ga ago (9). It has been unknown how long the dynamo persisted beyond this time. The youngest lunar paleointensity constraint is an upper limit of 7 μT at <7 million years (Ma) ago provided by an impact glass splash (10).

The time of the dynamo's cessation has major implications for the mechanism of magnetic field generation as well as the thermal and mechanical evolution of the lunar interior (6). For example, a core dynamo powered purely by thermal convection (11–14) is thought to only be able to persist until ~3.5 Ga ago (15). In comparison, a mechanical dynamo driven by mantle precession (16) is thought to be sustainable until sometime between ~3.4 and 2.0 Ga ago for typical lunar physical parameters (6, 9). Alternatively, a thermochemical convection dynamo powered by core crystallization could power the dynamo even until close to the present time (15, 17).

To constrain the late history of the lunar magnetic field, we studied the paleomagnetism of the young Apollo 15 breccias 15465 and 15015 (18). During the assembly of these breccias, their clasts were welded together by 60 to 90 volume % matrix melt glass formed by impact melting of the local lunar regolith (section S1) (19). Breccia 15465 was a float sample collected from the rim of Spur crater and contains clasts with diameters ranging from <1 to ~80 mm that are dominantly regolith breccias (figs. S1 and S7). Our $^{40}\text{Ar}/^{39}\text{Ar}$, $^{38}\text{Ar}/^{36}\text{Ar}$, and $^{40}\text{Ar}/^{36}\text{Ar}$ measurements, combined with previous Ar analyses, indicate that the assembly of 15465 and the formation of its matrix glass most likely occurred at 0.44 ± 0.01 Ga ago (age ranges are 1 SD), while a ~20-mm-diameter regolith breccia clast formed at >3.4 Ga

ago (section S7, table S20, and fig. S38). The latter clast contains a diversity of subclasts, including anorthosites, norites, and KREEP (potassium–rare earth element–phosphorus)–rich basalts that resemble the nearby Apollo 15 basalts (20, 21). Sample 15015 is a regolith breccia collected as float on the mare surface ~20 m from the Apollo 15 Lunar Module (19, 22). It contains <0.1- to 7-mm-diameter clasts in the form of rock, mineral, and glass fragments (figs. S2 and S11). Our $^{40}\text{Ar}/^{39}\text{Ar}$, $^{38}\text{Ar}/^{37}\text{Ar}$, and $^{40}\text{Ar}/^{36}\text{Ar}$ chronometry data indicate that 15015's matrix glass likely formed at 0.91 ± 0.11 Ga ago, consistent with previous measurements (see section S7, table S21, and fig. S39). Combined with our thermal diffusion calculations (section S2), these data indicate that the matrix melt glass, clasts smaller than ~10 mm in diameter, and the thermally equilibrated exteriors of larger clasts should have recorded any ambient lunar magnetic field at ~0.4 Ga ago (15465) and ~0.9 Ga ago (15015).

Similar to previously studied regolith breccias (9), the ferromagnetic carriers in the glassy matrices of 15015 and 15645 have exceptional magnetic recording properties compared to most lunar rocks (section S6). Our electron microscopy observations indicate that the dominant ferromagnetic minerals in the glass matrix of 15465 are kamacite ($\alpha\text{-Fe}_{1-x}\text{Ni}_x$ with $x < \sim 0.04$) and schreibersite ($\text{Fe}_{1-x}\text{Ni}_x$)₃P with $x \sim 0.1$, while the aforementioned glassy regolith breccia clast contains mostly kamacite and martensite ($\alpha_2\text{-Fe}_{1-x}\text{Ni}_x$ with $x \sim 0.08$) (fig. S24). Previous analytical electron microscopy (AEM) studies of the matrix glass in 15015 found that it contains kamacite (23), while our electron microscopy observations identified both kamacite and schreibersite (fig. S28). Our hysteresis and isothermal remanent magnetization (IRM) and first-order reversal curve (FORC) measurements of the regolith breccia clast in 15465 and the glass matrix in 15015, along with the AEM data (23), indicate a dominantly single-vortex to superparamagnetic grain size, while the glass matrix in 15465 contains grains ranging from single domain to multidomain in size (figs. S25 to S27, S29, and S30).

Given the mineralogies and compositions of the ferromagnetic grains in 15465 and 15015, these grains should have acquired mostly a total thermoremanent magnetization (TRM) in any ambient magnetic field following the last major heating event (see section S6). The degree of crystallinity in the matrix glasses of the two breccias indicates that they cooled from the 780°C Curie point of kamacite to ambient surface temperatures over >24 hours (section S2 and fig. S4). Because this time scale exceeds the estimated lifetime of putative impact-generated fields from even the largest lunar impacts (24), the matrix glasses in these breccias should have only recorded any ambient dynamo field during cooling. The lack of microfractures in the

¹Department of Earth, Atmospheric, and Planetary Sciences, Massachusetts Institute of Technology (MIT), 77 Massachusetts Avenue, Cambridge, MA 02139, USA. ²School of Earth Sciences, China University of Geosciences (Wuhan), 388 Lumo Road, Wuhan, Hubei 430074, P. R. China. ³Department of Earth and Planetary Science, University of California, Berkeley, Berkeley, CA 94720, USA. ⁴Berkeley Geochronology Center, 2455 Ridge Road, Berkeley, CA 94709, USA.

*These authors contributed equally to this work.

†Corresponding author. Email: bpweiss@mit.edu (B.P.W.); huapei@mit.edu (H.W.); smighani@mit.edu (S.M.)

glass matrices of both breccias (see figs. S1 and S2) constrains post-cooling peak shock pressures to below ~ 3 GPa (25).

We analyzed the paleomagnetism of the breccias in the Massachusetts Institute of Technology (MIT) Paleomagnetism Laboratory using a 2G Enterprises superconducting rock magnetometer (SRM), focusing on the matrix glass. Natural remanent magnetization (NRM) components were determined using alternating field (AF) and thermal demagnetization. Paleointensities were estimated using both nonthermal [i.e., anhysteretic remanent magnetization (ARM) and IRM] and double-heating (26) experiments (sections S3 and S4). To mitigate thermochemical alteration, the thermal demagnetization and paleointensity experiments were conducted in a $\text{CO}_2\text{-H}_2$ gas-mixing

controlled-atmosphere oven (27) at an oxygen fugacity of 0.5 to 1 log unit below the iron-wüstite buffer (28, 29). We measured the paleomagnetism of 8 and 22 matrix glass-rich subsamples of 15465 and 15015, respectively, 3 subsamples of the regolith breccia clast of 15465, 1 subsample of a ~ 7 -mm-diameter 15015 clast, and 2 composite 15015 subsamples each composed of a single large clast and surrounding matrix glass. Note that the matrix glass-rich subsamples from 15015 also commonly contain some small (<1 -mm-diameter) clasts. To our knowledge, the NRM of 15465 has never been previously studied. Two previous studies briefly characterized the IRM (30) of 15015 and estimated paleointensities using nonthermal experiments (31) (section S3).

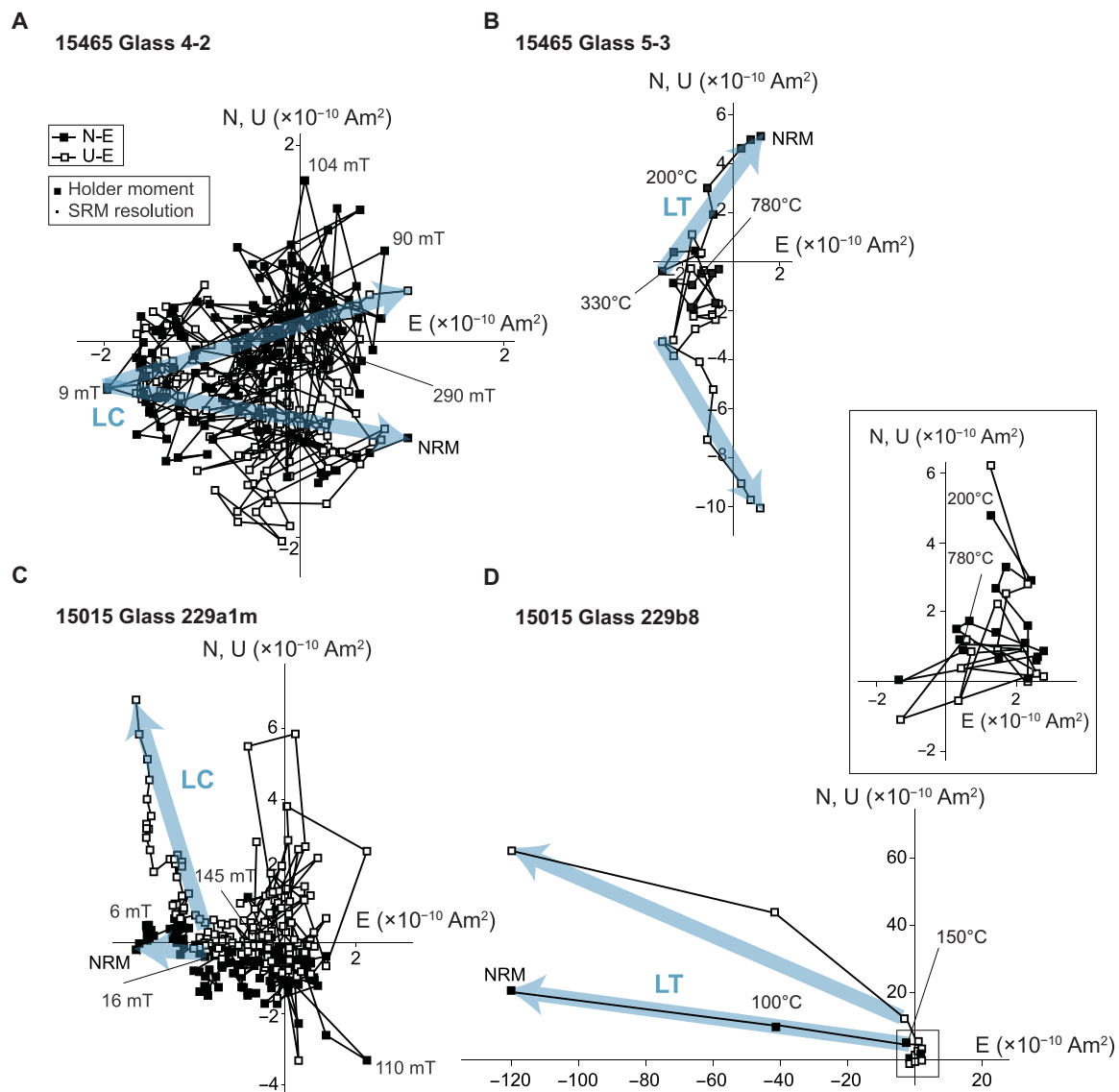


Fig. 1. NRM demagnetization of matrix glass subsamples from breccias 15465 and 15015. Shown are endpoints of the NRM vectors during progressive alternating field (AF) and thermal demagnetization. Closed and open symbols represent projections of the NRM vectors onto the horizontal (N-E) and vertical (U-E) planes, respectively. (A) 15465 subsample 4-2. (B) 15465 subsample 5-3. (C) 15015 subsample 229a1m. (D) 15015 subsample 229b8. Inset: Magnified view of HT demagnetization steps for 229b8. The legend in (A) shows the sample holder magnetic moment (denoted by the size of the large black box) and the MIT SRM moment resolution (denoted by the size of the small black box) (section S3). The initial NRM, AF levels, and temperatures for selected demagnetization steps are labeled. For both breccias, after removal of low coercivity (LC) and low temperature (LT) components (blue arrows), there is no discernible origin-trending magnetization in the high coercivity (HC)/high temperature (HT) range (as indicated by scattered vector endpoints).

RESULTS

Breccia 15465

We found that the matrix glass in 15465 contains a low coercivity (LC) and a low temperature (LT) component that unblocked by ~ 3 to 10 mT and 330° to 390°C , respectively (Fig. 1, fig. S9, and table S4). This component is non-unidirectionally oriented throughout the sample (fig. S8A). Given that the matrix glass was heated above the kamacite Curie temperature during its formation and so should have acquired a stable, unidirectional magnetization in the direction of any ambient field, the low AF and thermal stability and the non-unidirectionality of these components suggest that they are secondary

and postdate breccia formation. Blocking temperature relationships for single-domain and single-vortex iron indicate that lunar samples are expected to have viscous overprints with 1-hour blocking temperatures somewhere between $\sim 125^\circ$ and 485°C (32, 33), consistent with the observed peak unblocking temperature of the LC component. Our laboratory viscous remanent magnetization (VRM) experiments indicate that the magnitude of terrestrial VRM acquired over four decades of storage in Earth's magnetic field at Johnson Space Center (JSC) could have reached $\sim 130\%$ of the LC/LT components (section S5). Therefore, the LC/LT components are likely VRMs acquired in the geomagnetic field, although there may also

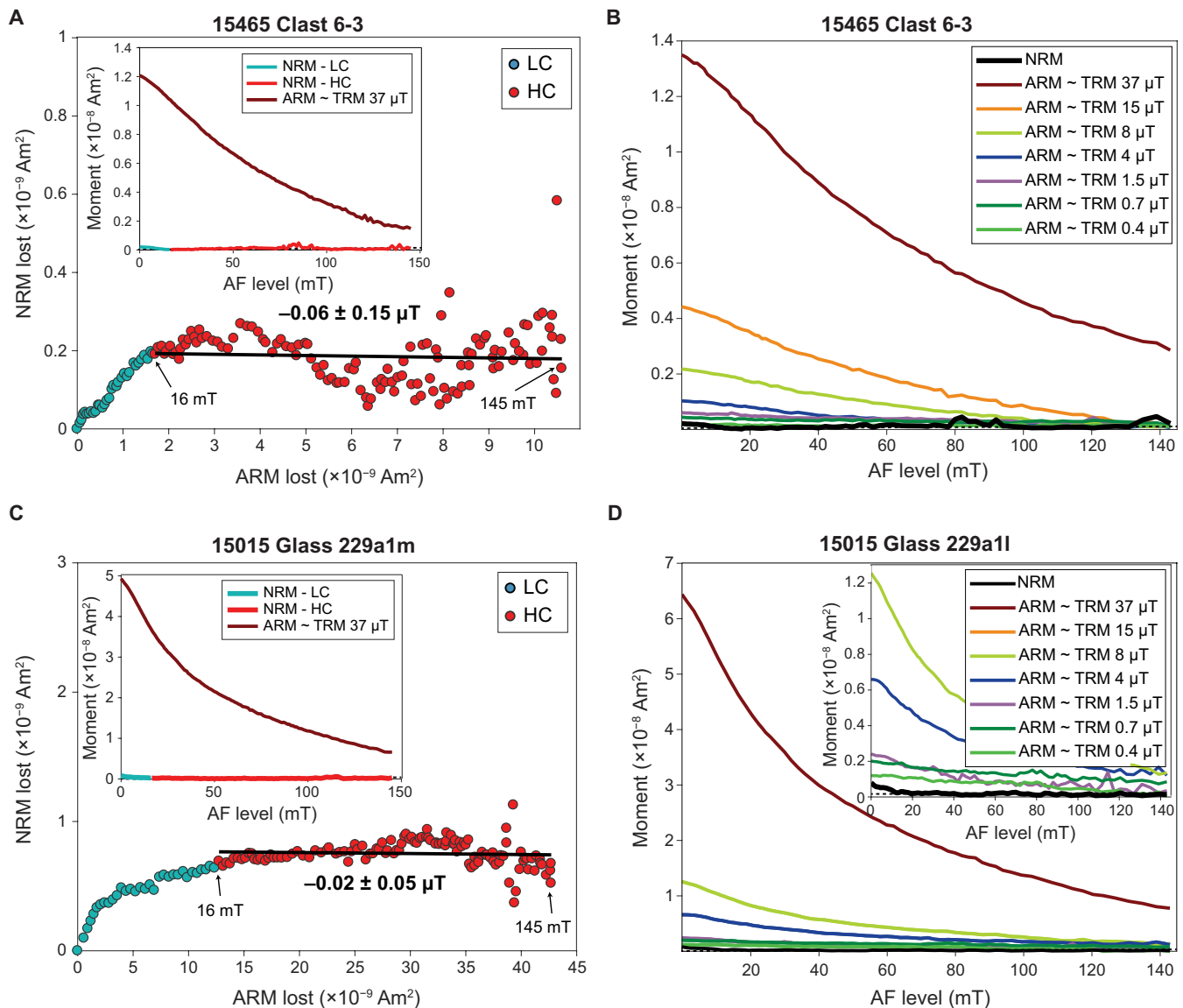


Fig. 2. Paleointensity estimates for subsamples of breccias 15465 and 15015. (A and C) ARM paleointensity experiments on 15465 subsample 6-3 and 15015 subsample 229a1m, respectively. Paleointensities are estimated from NRM lost during AF demagnetization as a function of ARM gained in a 50- μT DC bias field and a 260-mT AF. AF steps used to calculate the LC and HC paleointensities are colored blue and red, respectively. Paleointensities and their uncertainties (95% confidence intervals) are shown for the HC range. Insets in (A) and (C) show the decay of NRM and ARM during progressive AF demagnetization. (B and D) ARM paleointensity fidelity tests on 15465 subsample 6-3 and 15015 subsample 229a1m, respectively. Legends list TRM-equivalent fields for ARMs acquired in a range of DC bias fields in an AF of 260 mT and assuming ARM/TRM = 1.34 (section S4) (49). Horizontal dashed lines indicate the noise level due to acquisition of spurious ARM during AF demagnetization. Inset in (D) shows a magnified view of the moment decay.

be a contribution from exposure to stray fields during handling by the astronauts or at JSC (34). The LC/LT components for the clast subsamples unblocked by ~16 to 65 mT (fig. S9) and 200°C (fig. S10B) and likely have similar origins to those in the matrix glass (section S3).

After removal of the LC/LT components in 15465, further demagnetization of matrix glass samples produced directionally unstable moments with no consistent decay in magnitude (Fig. 1 and fig. S9). Principal components analysis (PCA) of these high coercivity (HC) and high temperature (HT) ranges yielded non-origin-trending components [deviation angle > maximum angular deviation (MAD) (35); table S4] with highly scattered directions and most MAD values >40° (fig. S8B and table S4). This indicates the absence of any HC/HT components and a lack of total TRM in the glass subsamples. Furthermore, we found that the ARM, IRM, and thermal paleointensities for the glass subsamples are within error of zero for the HC/HT range (Fig. 2, figs. S16 and S18, tables S6 to S7, and section S4). For the nonthermal paleointensities, the mean HC paleointensity value for glass samples is $-0.10 \pm 0.08 \mu\text{T}$ (paleointensity ranges are 2 SDs), with ~90% of experiments yielding nominal values of <0.7 μT . Glass sample HT thermal paleointensities are less well constrained but also near zero (mean value of $3.8 \pm 2.9 \mu\text{T}$). Partial TRM (pTRM) checks during the thermal experiments indicate a lack of thermochemical alteration during laboratory heating up to 730°C (section S4 and fig. S18), although the samples acquired substantial pTRM during in-field heating steps. Like the matrix glass samples, we also found that subsample 6-3, which is from the exterior of the 15465 regolith breccia clast that is expected to have been heated above the kamacite Curie temperature by surrounding matrix melt after breccia assembly, exhibits an unmagnetized HC range (ARM and IRM mean paleointensity of $-0.13 \pm 0.22 \mu\text{T}$ and residual ARM paleointensity of <0.06 μT) (Fig. 2A, tables S6 and S7, and section S4). The lack of stable NRM in 15465 is not only due to poor magnetic recording properties of the sample: Our 15465 paleointensity fidelity analyses indicate that our nonthermal methods can accurately measure paleointensities of <0.4 μT (Fig. 2B, section S4, and table S11). Overall, our measurements of 15465 show that the lunar surface field was almost certainly below 0.4 μT and very likely below even 0.06 μT , at the time it was assembled at 0.44 ± 0.01 Ga ago.

Breccia 15015

Demagnetization of 15015 glass-rich, clast, and composite clast glass subsamples yielded similar results. Subsamples taken from within 2.7 mm of two surfaces previously cut with a bandsaw at JSC in 1971 have NRM intensities and directions that correlate with the position of the subsamples (fig. S15D, table S5, and section S3). Subsamples with surfaces cut by the JSC bandsaw have stable, origin-trending LC/LT components with low unblocking temperatures (150°C) (Fig. 1D) but high peak coercivities (>145 mT) (fig. S13, C and D). The LC/LT components are collectively highly non-unidirectional but have directions dispersed approximately along a great circle and correlated with the distance of the subsamples from the two JSC sawcut surfaces (fig. S15C). The peak AF levels and unblocking temperatures of the LC/LT components also correlate with distance from the JSC sawcuts (fig. S15 and table S5). These LC/LT components have a paleointensity of ~5 to 69 μT , within the range of Earth's present field (table S8 and section S4). These observations indicate that the LC/LT overprints are likely overprints acquired during bandsaw cutting at JSC, which has been shown to partially thermally remagnetize sam-

ples due to the lack of a coolant (8). By comparison, for glass subsamples located >3.4 mm from either JSC sawcut, the LC/LT components unblocked by just ~2 to 16 mT and <150°C (Fig. 1C; fig. S13, A and B; and table S5). The low AF and thermal stability and non-unidirectionality of these components (fig. S12) suggest that they are also recent overprints. Our laboratory VRM acquisition experiments indicate that the magnitudes of the LC/LT components of these interior samples are consistent with their origin as a terrestrial VRM (section S5) with a possible weak contribution from bandsaw heating.

As with the 15465 subsamples, after removal of the LC/LT components, we found that the remaining NRM does not consistently weaken in intensity or maintain a stable orientation during further demagnetization in the HC/HT range (Fig. 1, C and D, and fig. S13), with PCA fits yielding scattered, non-origin-trending fits with MAD values >30°. As with 15465, this again indicates the absence of an HC/HT component. Our HC/HT ARM and IRM paleointensities (Fig. 2C, fig. S17, and tables S7 and S8) are indistinguishable from zero (with glass samples having a mean value of $-0.01 \pm 0.02 \mu\text{T}$ and 68% of samples having nominal values of <0.1 μT) and the residual ARM paleointensity of <0.08 μT . Our thermal paleointensity experiments measured an HT mean value of $0.31 \pm 0.18 \mu\text{T}$ (Fig. 3, fig. S19, and table S8), with pTRM checks (table S10) demonstrating that no substantial thermochemical alteration occurred up to 680°C. Our paleointensity fidelity measurements indicate that 15015 can accurately record paleofields of <0.7 μT (Fig. 2D and section S4). Collectively, these data indicate a lack of total TRM during the breccia formation. We conclude that the matrix glass of breccia 15015 certainly formed in a field of no more than 0.7 μT and very likely less than 0.08 μT at 0.91 ± 0.11 Ga ago.

DISCUSSION

Our results from both breccias show that the lunar surface field was very likely below 0.06 and 0.08 μT at 0.44 ± 0.01 Ga ago and 0.91 ± 0.11 Ga ago, respectively. These upper limits are at or below inferred lunar

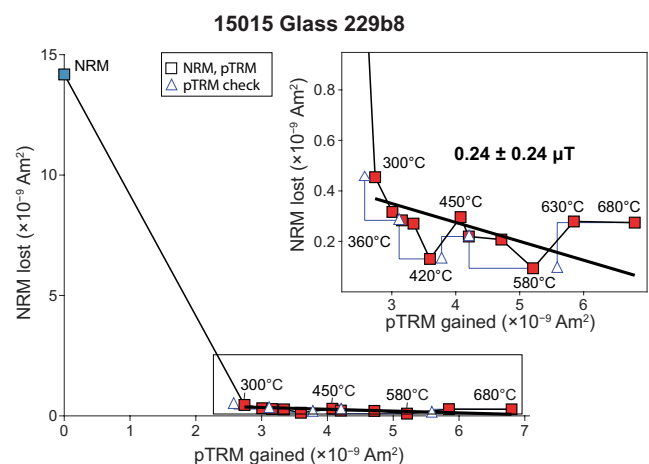


Fig. 3. Thermal paleointensity estimate for 15015 matrix glass. Shown is the NRM lost during progressive thermal demagnetization versus pTRM gained by heating in a laboratory field of 3 μT for subsample 229b8. Inset: Magnified view of 300° to 680°C temperature steps. NRM lost and pTRM gained steps are denoted with squares, with blue and red symbols denoting data in the LT and HT ranges, respectively. pTRM checks for alteration are denoted with triangles. The HT range has a paleointensity value of $0.24 \pm 0.24 \mu\text{T}$.

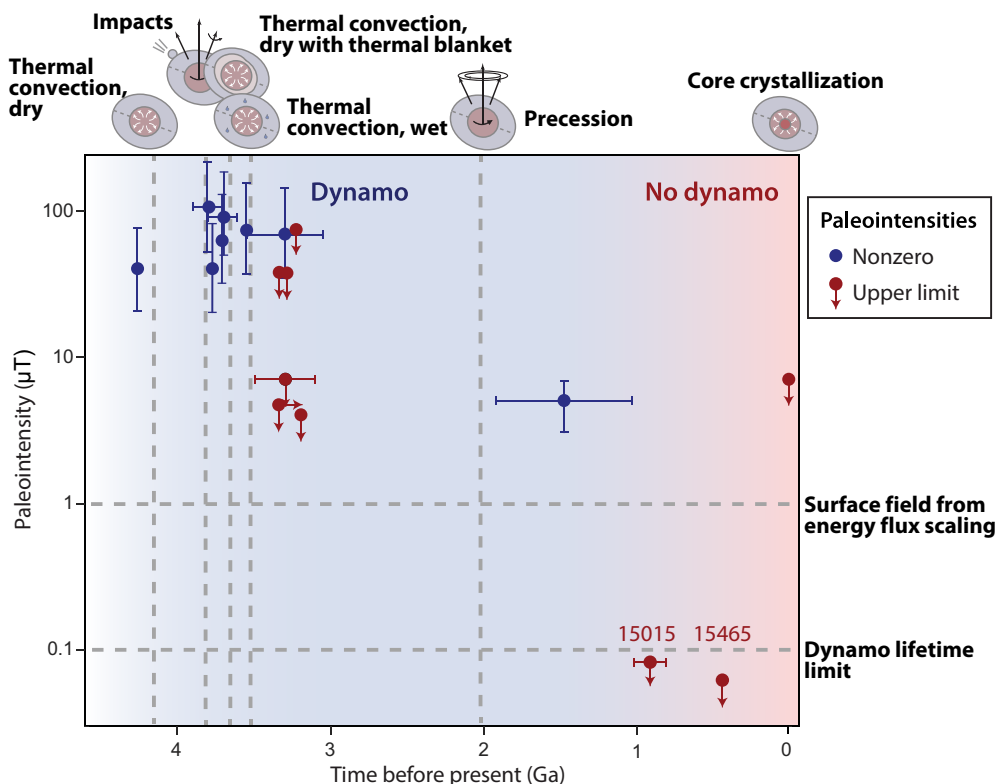


Fig. 4. Paleointensities for breccias 15465 and 15015 and those of other modern measurements of lunar rocks. Points labeled 15015 and 15465 are new paleointensity estimates reported by this study, while the remaining points are previously measured values (6, 9). Red points denote upper limits on the field (i.e., values indistinguishable from zero), while blue points denote nonzero values (i.e., detections of the paleofield). Vertical and horizontal arrows and error bars indicate the paleointensity and age limits and 1-SD uncertainties, respectively. The blue and red shaded regions indicate the epochs when the dynamo is inferred to be active and have ceased, respectively. Vertical and horizontal arrows and error bars indicate the paleointensity and age limits and uncertainties, respectively. The vertical dashed lines are the lifetime for proposed dynamo mechanisms: thermal convection in a dry mantle (11), impact-driven changes in mantle rotation (50), thermal convection in a dry mantle covered by a thermal blanket (12), thermal convection in a wet mantle (13), lunar precession (16), and core crystallization (15). The upper and lower horizontal dashed lines denote the maximum field predicted by energy flux scaling (36) and the predicted field exceeded by all published dynamo models for >90% of the dynamo lifetime, respectively. Data are tabulated in table S22.

surface fields over much of the mare (1) and compatible with the weak fields measured at the Apollo 15 site (2). These upper limits are also below the surface fields typically predicted by dynamo scaling laws (36): In particular, all published lunar thermal and evolution models (12, 14–16, 37, 38) predict surface fields of $>0.1 \mu\text{T}$ for $>\sim 90\%$ of the dynamo's active period. Such a weak intensity is also below the weakest known dynamo surface field in the solar system today, that of Mercury (39). Therefore, we conclude that the lunar dynamo was likely no longer operating at 0.91 ± 0.11 Ga ago.

The youngest evidence for the existence of the lunar dynamo is the $\sim 5 \pm 2 \mu\text{T}$ paleointensity estimate from regolith breccia 15498, whose age of assembly is constrained using $^{40}\text{Ar}/^{39}\text{Ar}$ chronometry (9) to $\sim 1.75 \pm 0.75$ Ga ago and using trapped $^{40}\text{Ar}/^{36}\text{Ar}$ data (40) to $1.32^{+0.59}_{-0.52}$ (section S7.5). We obtain a new refined age of the NRM in 15498 by adopting the weighted mean of these two ages of 1.47 ± 0.45 Ga ago. Combining the 1-SD extremes of the age estimates for 15498 and 15015, we conclude that the dynamo ceased sometime between 1.92 and 0.80 Ga ago. Furthermore, the age and paleointensity constraints on 15465 indicate that the dynamo field remained absent at 0.44 ± 0.01 Ga ago (Fig. 4). Such a protracted history is likely inconsistent with the late magnetic field being generated by precession (16, 41), which is thought to have only been capable of powering a dynamo until

~ 2.0 Ga ago given the expected evolution of the lunar orbit (9). Instead, the persistence of the magnetic field until after 1.92 Ga ago is likely compatible with the late dynamo being driven by core crystallization for relatively low values of core thermal conductivity and expansivity (17). Future paleointensity studies on young Apollo samples should determine whether the dynamo ceased permanently after 1.92 Ga ago or, alternatively, whether it entered a start-stop regime (17).

METHODS

Paleomagnetism

Paleomagnetic analyses were conducted using a 2G Enterprises SRM 755 inside the MIT Paleomagnetism Laboratory. We prepared mutually oriented subsamples of 15465 and 15015 in this shielded room using a wire saw previously shown to not measurably disturb the NRM of lunar samples (8).

Static three-axis AF demagnetization of NRM was conducted up to a maximum AF of 145 mT for most subsamples (in some cases, up to 290 mT). Thermal demagnetization and thermal paleointensity experiments were conducted up to 780°C in a $\text{CO}_2\text{-H}_2$ gas-mixing controlled-atmosphere oven (27) at an oxygen fugacity set to the estimated formation conditions of lunar materials (0.5 to 1 log units

below the iron-wüstite buffer) (28, 29). ARM and IRM paleointensities were conducted using multicomponent methods (42, 43). The thermal paleointensities were conducted following the IZZI (in-field, zero-field, zero-field, in-field) protocol (44) and included pTRM checks for alteration. NRM components were estimated using PCA (45).

ARM and IRM measurements were obtained using the MIT SRM. Hysteresis and FORC measurements were conducted at the MIT Department of Materials Science and Engineering using a vibrating sample magnetometer.

$^{40}\text{Ar}/^{39}\text{Ar}$, $^{38}\text{Ar}/^{37}\text{Ar}$, and $^{40}\text{Ar}/^{36}\text{Ar}$ chronometry

$^{40}\text{Ar}/^{39}\text{Ar}$, $^{38}\text{Ar}/^{37}\text{Ar}$, and $^{40}\text{Ar}/^{36}\text{Ar}$ thermochronometry experiments were conducted at the Berkeley Geochronology Center following our previously described procedures (4, 8, 46). We analyzed both whole rock matrix glass and clast subsamples from both lithologies. We calculated apparent $^{40}\text{Ar}/^{39}\text{Ar}$ ages for each degassing step relative to the Hb3gr fluence monitor [age = 1081 Ma (47)] using the decay constants of (47) and the isotopic abundances of (48). For 15465 glass subsample 6-4-1, 15465 clast subsample 6-2, and 15015 glass subsample 229b1, we corrected the $^{40}\text{Ar}/^{39}\text{Ar}$ ages for the trapped ^{40}Ar using the ordinate-intercept $^{40}\text{Ar}/^{36}\text{Ar}$ ratios determined by error-weighted linear regressions in three-isotope plots. Cosmogenic ^{38}Ar exposure ages for each degassing step were estimated following the procedures described in (46).

SUPPLEMENTARY MATERIALS

Supplementary material for this article is available at <http://advances.sciencemag.org/cgi/content/full/6/1/eaax0883/DC1>

Section S1. Overview of samples

Section S2. Breccia thermal history

Section S3. NRM

Section S4. Paleointensities

Section S5. VRM experiments

Section S6. Magnetization carriers

Section S7. $^{40}\text{Ar}/^{39}\text{Ar}$, $^{38}\text{Ar}/^{37}\text{Ar}$, and $^{40}\text{Ar}/^{36}\text{Ar}$ chronometry

Fig. S1. Photomicrographs of 15465.

Fig. S2. Photomicrographs of 15015.

Fig. S3. Schematic time-temperature transformation curve for a generic cooling melt.

Fig. S4. Estimated melt cooling rate for breccias 15465 and 15015.

Fig. S5. Temperature distribution inside a clast with a one-dimensional contact with a cooling melt.

Fig. S6. Temperature distribution inside a spherical clast surrounded by a linearly cooling melt.

Fig. S7. Location of our 15465 subsamples relative to the parent sample 15465, 44, 115.

Fig. S8. Magnetization directions in 15465 inferred from PCA.

Fig. S9. AF demagnetization of 15465.

Fig. S10. Thermal demagnetization of 15465.

Fig. S11. Location of our 15015 subsamples and cuts relative to the parent samples 229a1, 229a3, and 229b.

Fig. S12. Magnetization directions in 15015 inferred from PCA.

Fig. S13. AF demagnetization of 15015 glass subsamples.

Fig. S14. Thermal demagnetization of 15015 subsamples.

Fig. S15. Magnetic overprints in 15015 subsamples from bandsaw cutting at JSC.

Fig. S16. Paleointensity estimates for breccia 15465 matrix glass and clast samples.

Fig. S17. Paleointensity estimates for breccia 15015 subsamples.

Fig. S18. Thermal paleointensity experiments for breccia 15465 subsamples.

Fig. S19. Thermal paleointensity experiments for breccia 15015 glass subsamples.

Fig. S20. Paleointensity fidelity tests for breccia 15465.

Fig. S21. Paleointensity fidelity tests for breccia 15015.

Fig. S22. VRM acquisition by 15465 glass.

Fig. S23. VRM acquisition by 15015 glass.

Fig. S24. Electron microprobe analysis of magnetization carriers in 15465.

Fig. S25. Hysteresis and IRM acquisition/demagnetization curves for 15465 glass and clast subsamples.

Fig. S26. Dunlop-Day plot showing the domain state of breccias compared to other lunar rocks analyzed in the MIT Paleomagnetism Laboratory.

Fig. S27. FORC analysis of 15465 breccia subsamples.

Fig. S28. Electron microprobe analysis of magnetization carriers in 15015.

Fig. S29. Hysteresis and IRM acquisition/demagnetization curves for 15015 glass subsamples.

Fig. S30. FORC analysis for 15015 glass.

Fig. S31. Ar release spectra for 15465 glass subsample 6-4-1.

Fig. S32. Ar release spectra for 15465 clast subsample 6-2.

Fig. S33. Ar release spectra for 15015 glass subsample 229b1.

Fig. S34. Ar release spectra for 15015 clast subsample 229a1a.

Fig. S35. Ar three-isotope plot for 15465 glass subsample 6-4-1.

Fig. S36. Ar three-isotope plot for 15465 clast subsample 6-2.

Fig. S37. Ar three-isotope for 15015 glass subsample 229b1.

Fig. S38. Geologic and magnetization history of breccia 15465.

Fig. S39. Geologic and magnetization history of breccia 15015.

Table S1. Comparison between the glass compositions of breccias 15465, 15015, and 15498.

Table S2. Estimated cooling rate for 15465 and 15015 lunar rock compositions.

Table S3. Distances between 15465 matrix glass melt interface and our clast subsamples.

Table S4. NRM components during AF or thermal demagnetization for 15465 subsamples.

Table S5. NRM components during AF or thermal demagnetization for 15015 subsamples.

Table S6. Paleointensity estimates for 15465.

Table S7. Paleointensity upper limits for 15465 and 15015 based on the AREM method.

Table S8. Paleointensity estimates for 15015.

Table S9. Statistics for thermal paleointensity experiments for breccias 15465 and 15015.

Table S10. pTRM check parameters for double-heating experiments.

Table S11. Paleointensity fidelity tests for breccias 15465 and 15015.

Table S12. Upper paleointensity limits on breccias using different paleointensity methods.

Table S13. WDS of 15465 metal grains.

Table S14. Rock magnetic parameters for 15465 and 15015 subsamples.

Table S15. WDS of 15015 metal grains.

Table S16. $^{40}\text{Ar}/^{39}\text{Ar}$ degassing data for 15465 glass 6-4-1.

Table S17. $^{40}\text{Ar}/^{39}\text{Ar}$ degassing data for 15465 clast 6-2.

Table S18. $^{40}\text{Ar}/^{39}\text{Ar}$ degassing data for 15015 glass 229b1.

Table S19. $^{40}\text{Ar}/^{39}\text{Ar}$ degassing data for 15015 clast 229a1a.

Table S20. $^{40}\text{Ar}/^{39}\text{Ar}$, $^{40}\text{Ar}/^{36}\text{Ar}$, and $^{38}\text{Ar}/^{36}\text{Ar}$ analyses of breccia 15465.

Table S21. $^{40}\text{Ar}/^{39}\text{Ar}$, $^{40}\text{Ar}/^{36}\text{Ar}$, and $^{38}\text{Ar}/^{36}\text{Ar}$ analyses of breccia 15015.

Table S22. Modern paleointensity analyses of Apollo samples.

Database S1. Demagnetization data on 15465 and 15015.

References (51–103)

REFERENCES AND NOTES

1. D. S. Mitchell, J. S. Halekas, R. P. Lin, S. Frey, L. L. Hood, M. H. Acuña, A. Binder, Global mapping of lunar crustal magnetic fields by Lunar Prospector. *Icarus* **194**, 401–409 (2008).
2. M. Fuller, S. M. Cisowski, Lunar paleomagnetism, in *Geomagnetism*, J. A. Jacobs, Ed. (Academic Press, 1987), vol. 2, pp. 307–455.
3. I. Garrick-Bethell, B. P. Weiss, D. L. Shuster, J. Buz, Early lunar magnetism. *Science* **323**, 356–359 (2009).
4. E. K. Shea, B. P. Weiss, W. S. Cassata, D. L. Shuster, S. M. Tikoo, J. Gattacceca, T. L. Grove, M. D. Fuller, A long-lived lunar core dynamo. *Science* **335**, 453–456 (2012).
5. C.ournède, J. Gattacceca, P. Rochette, Magnetic study of large Apollo samples: Possible evidence for an ancient centered dipolar field on the Moon. *Earth Planet. Sci. Lett.* **331–332**, 31–42 (2012).
6. B. P. Weiss, S. M. Tikoo, The lunar dynamo. *Science* **346**, 1246753 (2014).
7. I. Garrick-Bethell, B. P. Weiss, D. L. Shuster, S. M. Tikoo, M. M. Tremblay, Further evidence for early lunar magnetism from troctolite 76535. *J. Geophys. Res.* **121**, 76–93 (2017).
8. S. M. Tikoo, B. P. Weiss, W. S. Cassata, D. L. Shuster, J. Gattacceca, E. A. Lima, C. Suavet, F. Nimmo, M. D. Fuller, Decline of the lunar core dynamo. *Earth Planet. Sci. Lett.* **404**, 89–97 (2014).
9. S. M. Tikoo, B. P. Weiss, D. L. Shuster, C. Suavet, H. Wang, T. L. Grove, A two-billion-year history for the lunar dynamo. *Sci. Adv.* **3**, e1700207 (2017).
10. J. Buz, B. P. Weiss, S. M. Tikoo, D. L. Shuster, J. Gattacceca, T. L. Grove, Magnetism of a very young lunar glass. *J. Geophys. Res.* **120**, 1720–1735 (2015).
11. W. Konrad, T. Spohn, Thermal history of the Moon: Implications for an early core dynamo and post-accretional magmatism. *Adv. Space Res.* **19**, 1511–1521 (1997).
12. D. R. Stegman, A. M. Jellinek, S. A. Zatman, J. R. Baumgardner, M. A. Richards, An early lunar core dynamo driven by thermochemical mantle convection. *Nature* **421**, 143–146 (2003).
13. A. J. Evans, M. T. Zuber, B. P. Weiss, S. M. Tikoo, A wet, heterogeneous lunar interior: Lower mantle and core dynamo evolution. *J. Geophys. Res.* **119**, 1061–1077 (2014).
14. F. Takahashi, H. Tsunakawa, Thermal core-mantle coupling in an early lunar dynamo: Implications for a global magnetic field and magnetosphere of the early Moon. *Geophys. Res. Lett.* **36**, L24202 (2009).
15. M. Laneuville, M. A. Wiczkorek, D. Breuer, J. Aubert, G. Morard, T. Rückriemen, A long-lived lunar dynamo powered by core crystallization. *Earth Planet. Sci. Lett.* **401**, 251–260 (2014).

16. C. A. Dwyer, D. J. Stevenson, F. Nimmo, A long-lived lunar dynamo driven by continuous mechanical stirring. *Nature* **479**, 212–214 (2011).
17. A. Scheinberg, K. M. Soderlund, G. Schubert, Magnetic field generation in the lunar core: The role of inner core growth. *Icarus* **254**, 62–71 (2015).
18. H. Wang, S. Mighani, B. P. Weiss, D. L. Shuster, K. V. Hodges, Lifetime of the lunar dynamo constrained by young Apollo returned breccias 15015 and 15465. *Proc. Lunar Planet. Sci. Conf.* **48**, 1439 (2017).
19. C. Meyer, *The Lunar Sample Compendium* (2016); <https://curator.jsc.nasa.gov/lunar/lsc/index.cfm>.
20. S. Simon, J. Papike, D. Gosselin, J. Laul, Petrology, chemistry and origin of Apollo 15 regolith breccias. *Geochim. Cosmochim. Acta* **50**, 2675–2691 (1986).
21. K. Cameron, J. Delano, Petrology of Apollo 15 consortium breccia 15465. *Proc. Lunar Sci. Conf. 4th* **1**, 461–466 (1973).
22. D. S. McKay, D. D. Bogard, R. v. Morris, R. L. Korotev, S. J. Wentworth, P. Johnson, Apollo 15 regolith breccias: Window to a KREEP regolith, in *19th Proceedings of Lunar and Planetary Science Conference* (1989), pp. 19–41.
23. S. Mehta, J. I. Goldstein, Analytical electron microscopy study of submicroscopic metal particles in glassy constituents of lunar breccias 15015 and 60095, in *10th Proceedings of Lunar and Planetary Science Conference* (1979), pp. 1507–1521.
24. L. L. Hood, N. A. Artemieva, Antipodal effects of lunar basin-forming impacts: Initial 3D simulations and comparisons with observations. *Icarus* **193**, 485–502 (2008).
25. S. M. Tikoo, B. P. Weiss, J. Buz, E. A. Lima, E. K. Shea, G. Melo, T. L. Grove, Magnetic fidelity of lunar samples and implications for an ancient core dynamo. *Earth Planet. Sci. Lett.* **337–338**, 93–103 (2012).
26. E. Thellier, O. Thellier, Sur l'intensité du champ magnétique terrestre dans le passé historique et géologique. *Ann. Geophys.* **15**, 285–376 (1959).
27. C. Suavet, B. P. Weiss, T. L. Grove, Controlled-atmosphere thermal demagnetization and paleointensity analyses of extraterrestrial rocks. *Geochem. Geophys. Geosyst.* **15**, 2733–2743 (2014).
28. M. Sato, N. L. Hickling, J. E. McLane, Oxygen fugacity values of Apollo 12, 14, and 15 lunar samples and reduced state of lunar magmas. *Proc. Lunar Planet. Sci. Conf. 4th* **1**, 1061–1079 (1973).
29. H. Mao, A. El Goresy, P. Bell, Evidence of extensive chemical reduction in lunar regolith samples from the Apollo 17 site. *Proc. Lunar Planet. Sci. Conf. 5th* **1**, 673–683 (1974).
30. S. M. Ciesowski, D. W. Collinson, S. K. Runcorn, A. Stephenson, M. Fuller, A review of lunar paleointensity data and implications for origin of lunar magnetism. *Proc. Lunar Planet. Sci. Conf. 13th* **88**, A691–A704 (1983).
31. D. W. Collinson, On the existence of magnetic fields on the Moon between 3.6 Ga ago and the present. *Phys. Earth Planet. Inter.* **34**, 102–116 (1984).
32. L. Nagy, W. Williams, L. Tauxe, A. R. Muxworthy, I. Ferreira, Thermomagnetic recording fidelity of nanometer-sized iron and implications for planetary magnetism. *Proc. Natl. Acad. Sci. U.S.A.* **116**, 1984–1991 (2019).
33. I. Garrick-Bethell, B. P. Weiss, Kamacite blocking temperatures and applications to lunar magnetism. *Earth Planet. Sci. Lett.* **294**, 1–7 (2010).
34. G. W. Pearce, W. A. Gose, D. W. Strangway, Magnetic studies on Apollo 15 and 16 lunar samples. *Proc. Lunar Sci. Conf. 4*, 3045–3076 (1973).
35. K. Lawrence, C. Johnson, L. Tauxe, J. Gee, Lunar paleointensity measurements: Implications for lunar magnetic evolution. *Phys. Earth Planet. Inter.* **168**, 71–87 (2008).
36. U. R. Christensen, Dynamo scaling laws and applications to the planets. *Space Sci. Rev.* **152**, 565–590 (2010).
37. M. Laneville, M. A. Wieczorek, D. Breuer, N. Tosi, Asymmetric thermal evolution of the Moon. *J. Geophys. Res.* **118**, 1435–1452 (2013).
38. M. Le Bars, M. A. Wieczorek, Ö. Karatekin, D. Cébron, M. Laneville, An impact-driven dynamo for the early Moon. *Nature* **479**, 215–218 (2011).
39. B. J. Anderson, M. H. Acuña, H. Korth, J. A. Slavin, H. Uno, C. L. Johnson, M. E. Purucker, S. C. Solomon, J. M. Raines, T. H. Zurbuchen, G. Gloeckler, R. L. McNutt Jr., The magnetic field of Mercury. *Space Sci. Rev.* **152**, 307–339 (2010).
40. A. L. Fagan, K. H. Joy, D. D. Bogard, D. A. Kring, Ages of globally distributed lunar paleoregoliths and soils from 3.9 Ga to the present. *Earth Moon Planets* **112**, 59–71 (2014).
41. J. Meyer, J. Wisdom, Precession of the lunar core. *Icarus* **211**, 921–924 (2011).
42. A. Stephenson, D. W. Collinson, Lunar magnetic field palaeointensities determined by an anhysteretic remanent magnetization method. *Earth Planet. Sci. Lett.* **23**, 220–228 (1974).
43. J. Gattacceca, P. Rochette, Toward a robust normalized magnetic paleointensity method applied to meteorites. *Earth Planet. Sci. Lett.* **227**, 377–393 (2004).
44. E. Ben-Yosef, H. Ron, L. Tauxe, A. Agnon, A. Genevey, T. E. Levy, U. Avner, M. Najjar, Application of copper slag in geomagnetic archaeointensity research. *J. Geophys. Res.* **113**, B08101 (2008).
45. J. L. Kirschvink, The least-squares line and plane and the analysis of palaeomagnetic data. *Geophys. J. Int.* **62**, 699–718 (1980).
46. D. L. Shuster, W. S. Cassata, Paleotemperatures at the lunar surfaces from open system behavior of cosmogenic ^{39}Ar and radiogenic ^{40}Ar . *Geochim. Cosmochim. Acta* **155**, 154–171 (2015).
47. P. R. Renne, G. Balco, K. R. Ludwig, R. Mundil, K. Min, Response to the comment by W. H. Schwarz et al. on “Joint determination of ^{40}K decay constants and $^{40}\text{Ar}^*/^{40}\text{K}$ for the Fish Canyon sanidine standard, and improved accuracy for $^{40}\text{Ar}/^{39}\text{Ar}$ geochronology” by P. R. Renne et al. (2010). *Geochim. Cosmochim. Acta* **75**, 5097–5100 (2011).
48. P. R. Renne, C. C. Swisher, A. L. Deino, D. B. Karner, T. L. Owens, D. J. De Paolo, Intercalibration of standards, absolute ages and uncertainties in $^{40}\text{Ar}/^{39}\text{Ar}$ dating. *Chem. Geol.* **145**, 117–152 (1998).
49. D. W. Collinson, A. Stephenson, S. K. Runcorn, Magnetic studies of Apollo 15 and 16 rocks. *Proc. Lunar Sci. Conf. 4*, 2963–2976 (1973).
50. C. Suavet, B. P. Weiss, W. S. Cassata, D. L. Shuster, J. Gattacceca, L. Chan, I. Garrick-Bethell, J. W. Head, T. L. Grove, M. D. Fuller, Persistence and origin of the lunar core dynamo. *Proc. Natl. Acad. Sci. U.S.A.* **110**, 8453–8458 (2013).
51. G. A. Swann, N. C. Bailey, R. M. Baston, V. L. Freeman, M. H. Hait, J. W. Head, H. E. Holt, K. A. Howard, J. B. Irwin, K. B. Larson, W. R. Muehlberger, V. S. Reed, J. J. Rennison, G. G. Schaber, D. R. Scott, L. T. Silver, R. L. Sutton, G. E. Ulrich, H. G. Wilshire, E. W. Wolfe, in *Apollo 15 Preliminary Science Report* (NASA publication SP-289, 1972), pp. 5-1–5-112.
52. G. Ryder, in *Catalog of Apollo 15 Rocks, Part 2* (NASA Curatorial Branch Publication 72, 1985).
53. The Apollo 15 Preliminary Examination Team, The Apollo 15 lunar samples: A preliminary description. *Science* **175**, 363–375 (1972).
54. T. Plieninger, O. A. Schaeffer, Laser probe ^{39}Ar – ^{40}Ar ages of individual mineral grains in lunar basalt 15607 and lunar breccia 15465. *Proc. Lunar Sci. Conf. 7th* **2**, 2055–2066 (1976).
55. R. Schaaf, F. Hörz, T. D. Thompson, J. Bauer, Shock metamorphism of granulated lunar basalt. *Proc. Lunar Sci. Conf. 10th*, 2547–2571 (1979).
56. G. Ryder, in *Catalog of Apollo 15 Rocks* (NASA Curatorial Branch Publication 72, 1985), p. 1296.
57. The European Consortium, in *Lunar Sample Studies* (1977), pp. 1–33.
58. J. C. Russ, R. T. Dehoff, *Practical Stereology* (Springer, ed. 2, 2000).
59. D. R. Uhlmann, L. C. Kleine, Crystallization kinetics, viscous flow, and thermal histories of lunar breccias 15286 and 15498. *Proc. Lunar Sci. Conf. 7th*, 2529–2541 (1976).
60. D. S. McKay, D. A. Morrison, Lunar breccias. *J. Geophys. Res.* **76**, 5658–5669 (1971).
61. J. M. Christie, D. T. Griggs, Electron petrography of Apollo 14 and 15 breccias and shock-produced analogs. *Proc. Lunar Sci. Conf. 4*, 365–382 (1973).
62. S. W. Kieffer, From regolith to rock by shock. *Moon* **13**, 301–320 (1975).
63. D. Stöffler, H.-D. Knöll, U. Maerz, Terrestrial and lunar impact breccias and the classification of lunar highland rocks. *Proc. Lunar Planet. Sci. Conf. 10th* **1**, 639–675 (1979).
64. J. G. Spray, Lithification mechanisms for planetary regoliths: The glue that binds. *Annu. Rev. Earth Planet. Sci.* **44**, 139–174 (2016).
65. D. R. Uhlmann, L. Klein, R. W. Hopper, Sintering, crystallization, and breccia formation. *Moon* **13**, 277–284 (1975).
66. R. K. Cardwell, D. S. Chinn, G. F. Moore, D. L. Turcotte, Frictional heating on a fault zone with finite thickness. *Geophys. J. Int.* **52**, 525–530 (1978).
67. H. S. Carslaw, J. C. Jaeger, *The Conduction of Heat in Solids* (Oxford Univ. Press, ed. 2, 1959).
68. H. Wang, B. P. Weiss, X. N. Bai, B. G. Downey, J. Wang, J. Wang, C. Suavet, R. R. Fu, M. E. Zucolotto, Lifetime of the solar nebula constrained by meteorite paleomagnetism. *Science* **355**, 623–627 (2017).
69. B. P. Weiss, J. Gattacceca, S. Stanley, P. Rochette, U. R. Christensen, Paleomagnetic records of meteorites and early planetesimal differentiation. *Space Sci. Rev.* **152**, 341–390 (2010).
70. A. Stephenson, Three-axis static alternating field demagnetization of rocks and the identification of natural remanent magnetization, gyroremanent magnetization, and anisotropy. *J. Geophys. Res.* **98**, 373–381 (1993).
71. J. R. Taylor, *An Introduction to Error Analysis: The Study of Uncertainties in Physical Measurements* (University of Science Books, 1997).
72. L. Tauxe, H. Staudigel, Strength of the geomagnetic field in the Cretaceous Normal Superchron: New data from submarine basaltic glass of the Troodos Ophiolite. *Geochim. Geophys. Geosyst.* **5**, Q02H06 (2004).
73. G. Kletetschka, M. A. Wieczorek, Fundamental relations of mineral specific magnetic carriers for paleointensity determination. *Phys. Earth Planet. Inter.* **272**, 44–49 (2017).
74. G. Acton, Q.-Z. Yin, K. L. Verosub, L. Jovane, A. Roth, B. Jacobsen, D. S. Ebel, Micromagnetic coercivity distributions and interactions in chondrules with implications for paleointensities of the early solar system. *J. Geophys. Res.* **112**, B03S90 (2007).
75. Y. Yu, Paleointensity determination using anhysteretic remanence and saturation isothermal remanence. *Geochim. Geophys. Geosyst.* **11**, Q02212 (2010).
76. Y. Yu, L. Tauxe, J. S. Gee, A linear field dependence of thermoremanence in low magnetic fields. *Phys. Earth Planet. Inter.* **162**, 244–248 (2007).
77. S.-C. L. L. Lappe, J. M. Feinberg, A. R. Muxworthy, R. J. Harrison, Comparison and calibration of nonheating paleointensity methods: A case study using dusty olivine. *Geochim. Geophys. Geosyst.* **14**, 2143–2158 (2013).
78. S. L. Halgedahl, S. R. Day, M. Fuller, The effect of cooling rate on the intensity of weak-field TRM in single-domain magnetite. *J. Geophys. Res.* **95**, 3690–3698 (1980).

79. L. Tauxe, *Essentials of Paleomagnetism: Fifth Web Edition* (2018).
80. G. A. Paterson, L. Tauxe, A. J. Biggin, R. Shaar, L. C. Jonestrask, On improving the selection of Thellier-type paleointensity data. *Geochim. Geophys. Geosyst.* **15**, 1180–1192 (2014).
81. J. F. J. Bryson, B. P. Weiss, R. J. Harrison, J. Herrero-Albillos, F. Kronast, Paleomagnetic evidence for dynamo activity driven by inward crystallisation of a metallic asteroid. *Earth Planet. Sci. Lett.* **472**, 152–163 (2017).
82. D. J. Dunlop, Theory and application of the Day plot (M_R/M_S versus H_{CR}/H_C)—1. Theoretical curves and tests using titanomagnetite data. *J. Geophys. Res.* **107**, EPM 4-1–EPM 4-22 (2002).
83. D. J. Dunlop, Theory and application of the Day plot (M_R/M_S versus H_{CR}/H_C)—2. Application to data for rocks, sediments, and soils. *J. Geophys. Res.* **107**, EPM 5-1–EPM 5-15 (2002).
84. R. J. Harrison, J. M. Feinberg, FORCinel: An improved algorithm for calculating first-order reversal curve distributions using locally weighted regression smoothing. *Geochim. Geophys. Geosyst.* **9**, Q01056 (2008).
85. L. J. Swartzendruber, V. P. Itkin, C. B. Alcock, The Fe-Ni (iron-nickel) system. *J. Phase Equilib.* **12**, 288–312 (1991).
86. J. I. Goldstein, H. Yakowitz, Metallic inclusions and metal particles in the Apollo 12 lunar soil. *Proc. Lunar Sci. Conf.* **2**, 177–191 (1971).
87. A. El Goresy, P. Ramdohr, L. A. Taylor, The geochemistry of the opaque minerals in Apollo 14 crystalline rocks. *Earth Planet. Sci. Lett.* **13**, 121–129 (1971).
88. A. S. Doan, J. I. Goldstein, The ternary phase diagram, Fe-Ni-P. *Metall. Trans.* **1**, 1759–1767 (1970).
89. R. J. Gambino, T. R. McGuire, Y. Nakamura, Magnetic properties of the iron-group metal phosphides. *J. Appl. Phys.* **38**, 1253–1255 (1967).
90. J. Gattacceca, P. Rochette, F. Lagroix, P.-E. Mathé, B. Zanda, Low temperature magnetic transition of chromite in ordinary chondrites. *Geophys. Res. Lett.* **38**, L10203 (2011).
91. J. L. Carter, VLS (Vapor-Liquid-Solid): Newly discovered growth mechanism on the lunar surface? *Science* **181**, 841–842 (1973).
92. I. McDougall, T. M. Harrison, *Geochronology and Thermochronology by the $^{40}\text{Ar}/^{39}\text{Ar}$ Method* (Oxford Univ. Press, ed. 2, 1999).
93. O. Eugster, G. F. Herzog, K. Marti, M. W. Caffee, in *Meteorites and the Early Solar System II*, D. S. Lauretta, H. Y. McSween, Eds. (University of Arizona Press, 2006), pp. 829–851.
94. O. Eugster, D. Terribilini, E. Polnau, J. Kramers, The antiquity indicator argon-40/argon-36 for lunar surface samples calibrated by uranium-235-xenon-136 dating. *Meteorit. Planet. Sci.* **36**, 1097–1115 (2001).
95. K. H. Joy, D. A. Kring, D. D. Bogard, D. S. McKay, M. Zolensky, Re-examination of the formation ages of the Apollo 16 regolith breccias. *Geochim. Cosmochim. Acta* **75**, 7208–7225 (2011).
96. D. Stöffler, G. Ryder, B. A. Ivanov, N. A. Artemieva, Cratering history and lunar chronology. *Rev. Mineral. Geochem.* **60**, 519–596 (2006).
97. L. Husain, in *The Apollo 15 Lunar Samples* (Lunar and Planetary Institute, 1972), pp. 374–375.
98. R. W. Carlson, G. W. Lugmair, Sm-Nd constraints on early lunar differentiation and the evolution of KREEP. *Earth Planet. Sci. Lett.* **45**, 123–132 (1979).
99. P. Vermeesch, IsoplotR: A free and open toolbox for geochronology. *Geosci. Front.* **9**, 1479–1493 (2018).
100. H. H. Schmitt, N. E. Petro, R. A. Wells, M. S. Robinson, B. P. Weiss, C. M. Mercer, Revisiting the field geology of Taurus-Littrow. *Icarus* **298**, 2–33 (2017).
101. R. D. Warner, G. F. Taylor, G. H. Conrad, H. R. Northrop, S. Barker, K. Keil, Apollo 17 high-Ti mare basalts: New bulk compositional data, magma types, and petrogenesis. *Proc. Lunar Planet. Sci. Conf.* **10th** **1**, 225–247 (1979).
102. J. B. Paces, S. Nakai, C. R. Neal, L. A. Taylor, A. N. Halliday, D.-C. Lee, A strontium and neodymium isotopic study of Apollo 17 high-Ti mare basalts: Resolution of ages, evolution of magmas, and origins of source heterogeneities. *Geochim. Cosmochim. Acta* **55**, 2025–2043 (1991).
103. D. Phinney, S. B. Kahl, J. H. Reynolds, $^{40}\text{Ar}/^{39}\text{Ar}$ dating of Apollo 16 and 17 rocks. *Proc. Lunar Sci. Conf.* **6th** **2**, 1593–1608 (1975).

Acknowledgments: We thank B. Carbone and K. Willis for administrative assistance.

Funding: We thank the NASA Solar System Workings and Planetary Major Equipment Programs (grant no. NNX15AL62G) and the NASA Solar System Exploration Research Virtual Institute node at Brown-MIT (grant no. NNA14AB01A) for support. **Author contributions:** B.P.W., H.W., and S.M. designed the research. H.W. and S.M. led the paleomagnetic analyses of 15015 and 15465, respectively, with contributions from C.S.B. and C.I.O.N. D.L.S. conducted the Ar experiments, and D.L.S. and B.P.W. interpreted the data. S.M. and B.P.W. led the writing of the paper. All authors participated in the scientific interpretation of the data and writing the manuscript. **Competing interests:** The authors declare that they have no competing interests. **Data and materials availability:** All data needed to evaluate the conclusions in the paper are present in the paper and/or the Supplementary Materials. Additional data related to this paper may be requested from the authors and will be posted in the Magnetics Information Consortium (MagIC) database (www2.earthref.org/MagIC/).

Submitted 20 February 2019

Accepted 22 October 2019

Published 1 January 2020

10.1126/sciadv.aax0883

Citation: S. Mighani, H. Wang, D. L. Shuster, C. S. Borlina, C. I. O. Nichols, B. P. Weiss, The end of the lunar dynamo. *Sci. Adv.* **6**, eaax0883 (2020).

Supplementary Materials for

The end of the lunar dynamo

Saied Mighani*, Huapei Wang*, David L. Shuster, Cauê S. Borlina, Claire I. O. Nichols, Benjamin P. Weiss*

*Corresponding author. Email: bpweiss@mit.edu (B.P.W.); huapei@mit.edu (H.W.); smighani@mit.edu (S.M.)

Published 1 January 2020, *Sci. Adv.* 6, eaax0883 (2020)

DOI: 10.1126/sciadv.aax0883

The PDF file includes:

Section S1. Overview of samples
Section S2. Breccia thermal history
Section S3. NRM
Section S4. Paleointensities
Section S5. VRM experiments
Section S6. Magnetization carriers
Section S7. $^{40}\text{Ar}/^{39}\text{Ar}$, $^{38}\text{Ar}/^{37}\text{Ar}$, and $^{40}\text{Ar}/^{36}\text{Ar}$ chronometry
Fig. S1. Photomicrographs of 15465.
Fig. S2. Photomicrographs of 15015.
Fig. S3. Schematic time-temperature transformation curve for a generic cooling melt.
Fig. S4. Estimated melt cooling rate for breccias 15465 and 15015.
Fig. S5. Temperature distribution inside a clast with a one-dimensional contact with a cooling melt.
Fig. S6. Temperature distribution inside a spherical clast surrounded by a linearly cooling melt.
Fig. S7. Location of our 15465 subsamples relative to the parent sample 15465, 44, 115.
Fig. S8. Magnetization directions in 15465 inferred from PCA.
Fig. S9. AF demagnetization of 15465.
Fig. S10. Thermal demagnetization of 15465.
Fig. S11. Location of our 15015 subsamples and cuts relative to the parent samples 229a1, 229a3, and 229b.
Fig. S12. Magnetization directions in 15015 inferred from PCA.
Fig. S13. AF demagnetization of 15015 glass subsamples.
Fig. S14. Thermal demagnetization of 15015 subsamples.
Fig. S15. Magnetic overprints in 15015 subsamples from bandsaw cutting at JSC.
Fig. S16. Paleointensity estimates for breccia 15465 matrix glass and clast samples.
Fig. S17. Paleointensity estimates for breccia 15015 subsamples.
Fig. S18. Thermal paleointensity experiments for breccia 15465 subsamples.
Fig. S19. Thermal paleointensity experiments for breccia 15015 glass subsamples.
Fig. S20. Paleointensity fidelity tests for breccia 15465.

Fig. S21. Paleointensity fidelity tests for breccia 15015.

Fig. S22. VRM acquisition by 15465 glass.

Fig. S23. VRM acquisition by 15015 glass.

Fig. S24. Electron microprobe analysis of magnetization carriers in 15465.

Fig. S25. Hysteresis and IRM acquisition/demagnetization curves for 15465 glass and clast subsamples.

Fig. S26. Dunlop-Day plot showing the domain state of breccias compared to other lunar rocks analyzed in the MIT Paleomagnetism Laboratory.

Fig. S27. FORC analysis of 15465 breccia subsamples.

Fig. S28. Electron microprobe analysis of magnetization carriers in 15015.

Fig. S29. Hysteresis and IRM acquisition/demagnetization curves for 15015 glass subsamples.

Fig. S30. FORC analysis for 15015 glass.

Fig. S31. Ar release spectra for 15465 glass subsample 6-4-1.

Fig. S32. Ar release spectra for 15465 clast subsample 6-2.

Fig. S33. Ar release spectra for 15015 glass subsample 229b1.

Fig. S34. Ar release spectra for 15015 clast subsample 229a1a.

Fig. S35. Ar three-isotope plot for 15465 glass subsample 6-4-1.

Fig. S36. Ar three-isotope plot for 15465 clast subsample 6-2.

Fig. S37. Ar three-isotope for 15015 glass subsample 229b1.

Fig. S38. Geologic and magnetization history of breccia 15465.

Fig. S39. Geologic and magnetization history of breccia 15015.

Table S1. Comparison between the glass compositions of breccias 15465, 15015, and 15498.

Table S2. Estimated cooling rate for 15465 and 15015 lunar rock compositions.

Table S3. Distances between 15465 matrix glass melt interface and our clast subsamples.

Table S4. NRM components during AF or thermal demagnetization for 15465 subsamples.

Table S5. NRM components during AF or thermal demagnetization for 15015 subsamples.

Table S6. Paleointensity estimates for 15465.

Table S7. Paleointensity upper limits for 15465 and 15015 based on the AREMc method.

Table S8. Paleointensity estimates for 15015.

Table S9. Statistics for thermal paleointensity experiments for breccias 15465 and 15015.

Table S10. pTRM check parameters for double-heating experiments.

Table S11. Paleointensity fidelity tests for breccias 15465 and 15015.

Table S12. Upper paleointensity limits on breccias using different paleointensity methods.

Table S13. WDS of 15465 metal grains.

Table S14. Rock magnetic parameters for 15465 and 15015 subsamples.

Table S15. WDS of 15015 metal grains.

Table S16. $^{40}\text{Ar}/^{39}\text{Ar}$ degassing data for 15465 glass 6-4-1.

Table S17. $^{40}\text{Ar}/^{39}\text{Ar}$ degassing data for 15465 clast 6-2.

Table S18. $^{40}\text{Ar}/^{39}\text{Ar}$ degassing data for 15015 glass 229b1.

Table S19. $^{40}\text{Ar}/^{39}\text{Ar}$ degassing data for 15015 clast 229a1a.

Table S20. $^{40}\text{Ar}/^{39}\text{Ar}$, $^{40}\text{Ar}/^{36}\text{Ar}$, and $^{38}\text{Ar}/^{36}\text{Ar}$ analyses of breccia 15465.

Table S21. $^{40}\text{Ar}/^{39}\text{Ar}$, $^{40}\text{Ar}/^{36}\text{Ar}$, and $^{38}\text{Ar}/^{36}\text{Ar}$ analyses of breccia 15015.

Table S22. Modern paleointensity analyses of Apollo samples.

References (51–103)

Other Supplementary Material for this manuscript includes the following:

(available at advances.sciencemag.org/cgi/content/full/6/1/eaax0883/DC1)

Database S1 (.zip format). Demagnetization data on 15465 and 15015.

Supplementary Text

Section S1. Overview of samples

1.1. Breccia 15465. Sample 15465 is a glass-welded polymict breccia (fig. S1) collected by the Apollo 15 mission from the rim of Spur crater at the base of the Apennine mountains and returned to Earth in 1971 (21, 51). 15465 contains regolith breccia clasts welded together by thick melt glass representing >60 vol.% of the sample (21, 52). The clasts contain a diversity of sub-clasts including potassium-rare earth element-phosphorus (KREEP)-rich basalts (20, 21), Apollo 15-like mare basalts, anorthosites and norites [see the study of clast 7 in ref. (21), which is sampled from the same clast as the large ~20 mm diameter regolith breccia clast in our study (fig. S1)]. The clast materials are thought to be derived from the local Apennine Front regolith and mixed with Aristillus-Autolycus ray materials (21) and/or with buried nearby KREEP-basalt flows (22). The similarity in composition of the matrix glass (21) with that of the Apennine Front soil composition (53) suggests that the matrix glass is shock-melted Apennine Front soil (54). Given the large volume fraction of melt glass, the shock that produced 15465 likely reached pressures of several tens of GPa (55) and produced post-shock temperatures in the matrix exceeding ~1300 °C given its approximately basaltic composition (tables S1 and S2).

1.2. Breccia 15015. Sample 15015 is a glass-welded polymict breccia (fig. S2) collected from the mare surface adjacent to the Apollo 15 Lunar Module and returned to the Earth in 1971 (56, 57). Its clasts consist of fragments of rock, minerals, and glass (fig. S2) welded together by ~90 vol.% matrix melt glass (31, 56). Like 15465, it is thought to contain a component of Aristillus-Autolycus ray materials (56) and/or buried nearby KREEP-basalt flows (22). The clasts have lithologies that are mostly (84%) a diversity of basalts (mare-, plagioclase-, and KREEP-basalts), with the remainder being metamorphosed basalt and highlands rocks. Part of the surface of the breccia is covered by a thin (0.5 to <5 mm thick) melt glass with the same composition as the bulk sample and that continuously grades into the interior matrix glass. These glasses are thought to have both formed simultaneously during breccia assembly (57). The similarity in composition between the matrix glass and nearby soils indicates that, like 15465, 15015 was formed by shock-melting and welding of the local regolith. As with 15465, the large melt fraction indicates that 15015 formed as a result of shock pressures of several tens of GPa (55) with temperatures in the matrix exceeding ~1300 °C.

Section S2. Breccia thermal history

2.1. Introduction. The matrix glass in our breccias was molten (>1300 °C) at the time of breccia formation and therefore was well above the 780 °C and 440 °C Curie points of kamacite and schreibersite, respectively (see section 6). As such, these phases in the matrix glass should have acquired a total TRM in any ambient fields as the matrix subsequently cooled. On the other hand, the clasts clearly did not exceed the liquidus temperature, meaning that kamacite grains within the clasts may not have been completely remagnetized by the breccia formation process. Here, we seek to determine the cooling rate of the matrix glass to establish the minimum duration of any recorded magnetic field (section 2.2). We then use this cooling rate to constrain the thermal history of clasts in each breccia as functions of their size and geometry to establish whether the interiors of the largest clasts might retain an ancient natural remanent magnetization (NRM) from prior to breccia assembly (section 2.3).

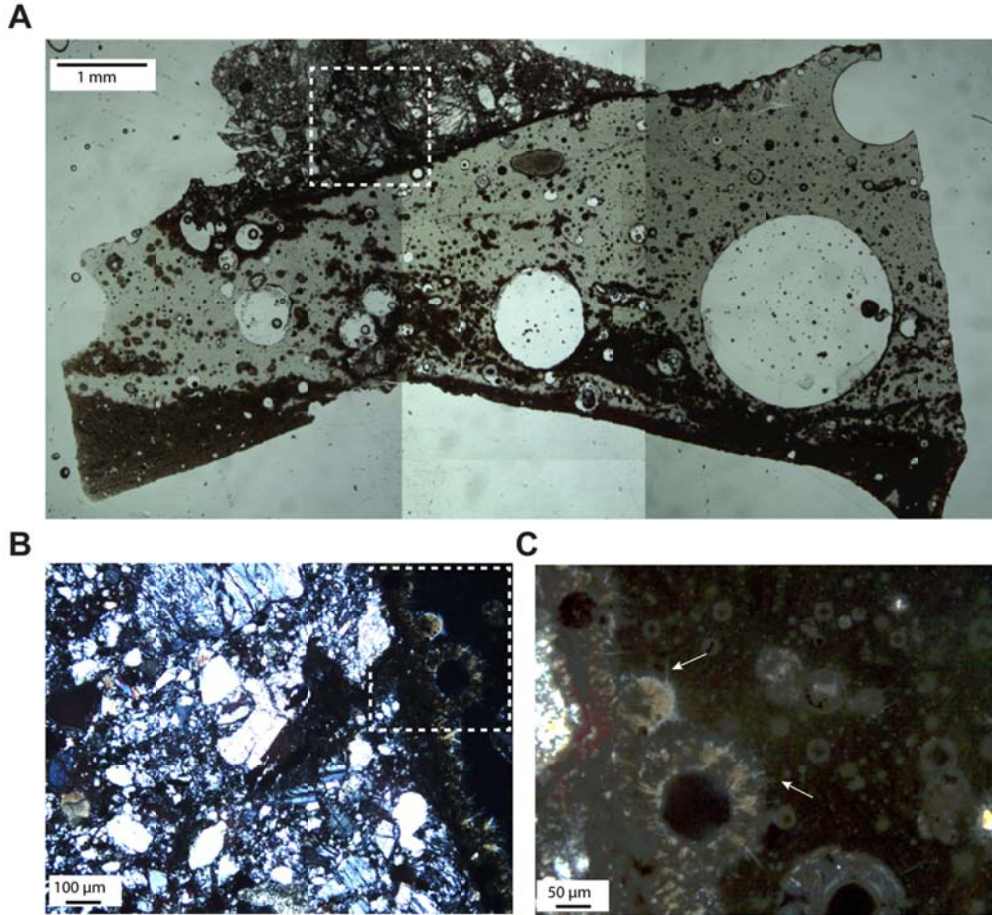


Fig. S1. Photomicrographs of 15465. Shown are images of a $\sim 30\ \mu\text{m}$ thin section from 15465 obtained from parent split 114, which we chipped from parent mass 44 at NASA Johnson Space Center (JSC). (A) Transmitted plane-polarized light image showing a clast fragment (top part of the section) bonded to the matrix glass (bottom part). The clast 15465 subsamples analyzed with paleomagnetism and Ar chronometry in this study are from the same clast shown here. Schlieren in the matrix glass indicates it is shock-melted (10). The dark regions in the glass at the clast edge and at the bottom of the section contain numerous small crystallites that nucleated on the edges of the clast and other relic crystals during breccia cooling. From this image, we estimate a crystallized volume fraction of $\sim 0.1\text{--}0.3$ (see section 2). A close-up of the crystallized region on the clast boundary (boxed region) is shown in (B). (B) Transmitted cross-polarized light image of boxed region in (A). The image shows that the clast in (A) is a regolith breccia composed of several welded fragments including plagioclase (gray) and olivine (brown) welded by interstitial glass. A magnified view of the crystallization on the clast-glass boundary in the white box in (B) is shown in (C). (C) Transmitted cross-polarized light image of boxed region in (B) showing needle-shaped crystals of devitrified glass (white arrows).

2.2. Matrix melt cooling rate. We begin by estimating the cooling timescale of each breccia from the kamacite Curie point (~ 780 °C) to the Moon's surface temperature (0 °C). In transmitted plane- polarized light, the glass matrix in 15465 is not uniformly transparent but rather contains localized darker regions that underwent partial crystallization during cooling below the liquidus temperature (fig. S1). From our thin section observations, we measured a crystal surface area fraction of ~ 0.1 - 0.3 for 15465 matrix glass (fig. S1) and ~ 0.5 for 15015 matrix glass (fig. S2B). Because the mean volume fraction equals the mean surface area fraction (58), we estimate a crystal volume fraction of ~ 0.1 - 0.3 and ~ 0.5 for 15465 and 15015 matrix glass.

Several mechanisms have been proposed for the assembly of lunar breccias from their constituent clast fragments following an impact. Among the proposed mechanisms, stress-free glass sintering at the lunar surface was proposed to be a viable mechanism for the breccia formation

Table S1. Comparison between the glass compositions of breccias 15465, 15015, and 15498.

Oxide	15465 ^a	15015 ^b	15498 ^c
SiO ₂	47.4	48.3	48.2
Al ₂ O ₃	17.0	13.7	19.8
TiO ₂	1.4	1.8	2.0
FeO	11.4	13.6	8.4
MgO	10.5	9.9	7.5
CaO	12.1	10.8	13.0
Na ₂ O	0.39	0.5	0.9
K ₂ O	0.28	0.2	-
Total	100.5	98.8	99.8

Notes: The first column lists the oxide names. The second to fourth columns list the oxide mass % for lunar breccias 15465, 15015, and 15498, respectively.

^aData from ref. (21)

^bData from ref. (19)

^cData from ref. (59)

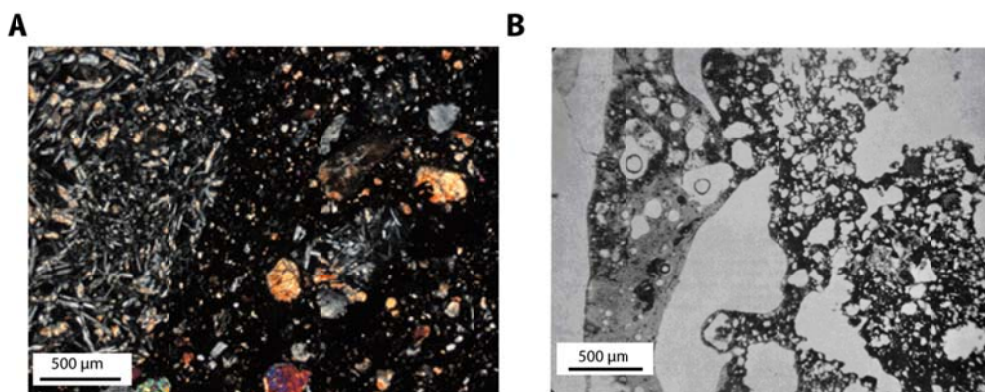


Fig. S2. Photomicrographs of 15015. Shown are images of a ~ 30 μm thin section from 15015. (A) JSC photo 15015,136_JSC01892-X1 from split 136 in transmitted cross-polarized light. Image shows a large clast at left (likely a textured KREEP basalt fragment) adjacent to matrix glass (right part). The smaller (<300 μm diameter) floating clasts in the melt are comprised of plagioclase (gray), olivine (brown), and other lithologies. The melt in this breccia makes up more than 90% volume of the breccia (31, 56). Based on this image, we estimate a crystallized volume fraction of ~ 0.5 (see section 2). (B) Vesicular glass coat (unspecified split number) as seen in transmitted plane-polarized light. Adapted from ref. (56).

rather than shock lithification (60). The main argument for favoring sintering was the high porosities usually observed for the breccias' glassy matrix, which challenged the assumption of breccia lithification due to shock pressurization alone without melting. However, experimentally shock-lithified lunar soils showed similar microstructures to lunar breccias (61). Therefore, the passage of a shock wave can readily fuse the fine fragments into breccia while maintaining high porosity (62). Further impact experiments on granulated basalt showed that at pressures as low as ~6 GPa, a glass-rich breccia could form after pore collapse (63, 64), with melt abundance correlated with the shock pressure (63). The prevalence of microbreccias and agglutinates in lunar breccias is further evidence for shock-lithification (62). The high abundance of melt glass in our breccias is more consistent with formation by shock-lithification (55).

After the breccias were assembled, they cooled slowly to the lunar surface temperature. We can estimate the time for melt cooling using the crystallization fraction of the glass (darker regions in figs. S1 and S2). Ref. (65) suggested the following relation for estimating the crystallized fraction (V_C/V) based on experimentally-derived crystal growth rates

$$\frac{V_C}{V} = \frac{\pi}{3} I_v u^3 t^4 \quad (\text{S1})$$

where the crystallization time is

$$t = \left(\frac{3 V_C/V}{\pi I_v u^3} \right)^{\frac{1}{4}} \quad (\text{S2})$$

and where I_v is the rate of nucleation per volume in $\text{s}^{-1} \text{m}^{-3}$ and u is the growth rate in units of m s^{-1} . I_v can also be derived from the following relation

$$I_v = \frac{10^{31}}{\mu} \exp \left(-\frac{1.229}{\Delta T_r^2 T_r^3} \right) \quad (\text{S3})$$

where $T_r \equiv T/T_E$, $\Delta T_r = (T - T_E)/T_E$ and T and T_E are temperature and liquidus temperature, respectively and μ is viscosity. These relations enable us to construct time-temperature transformation (TTT) curves, which quantify the dependence of the crystal fraction on the duration that the glass is held isothermally at a given temperature (fig. S3). The nose of a TTT curve (see fig. S3) results from the competition between the crystal growth rate and melt viscosity, both of which are temperature-dependent.

Continuous cooling (CT) curves can be generated by assuming either linear ($T = T_0 - Bt$) or logarithmic [$T = T_0 - C \ln(t)$] cooling rates where B , C , and T_0 are the linear rate, logarithmic rate, and initial temperature, respectively. The intersection of the CT and TTT curves constrains the minimum time required for the breccia formation for a certain melt crystal fraction. The corresponding temperature for minimum cooling rate, the minimum contact temperature, is derived from the point of tangency between the CT and TTT curves. To constrain the cooling rate for our breccias, we used physical properties previously measured for glass in the Apollo 15 regolith breccia 15498 (crystal growth rate, viscosity, and liquidus temperature) (59), which has a

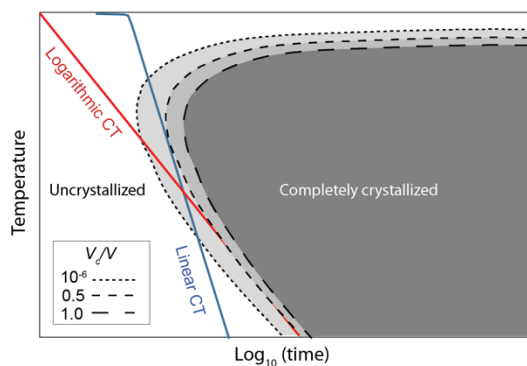


Fig. S3. Schematic time-temperature transformation curve for a generic cooling melt. The TTT curves (black dashed lines) depict time-temperature conditions to produce various crystal fractions (with curves to the right depicting increasing crystal fractions). Legend shows the crystal fractions. Also, shown are cooling paths assuming linear (blue) and logarithmic (red) continuous cooling (CT) curves. The intersection of CT and TTT curves is used to estimate the minimum cooling rate of melt. Adapted from ref. (65).

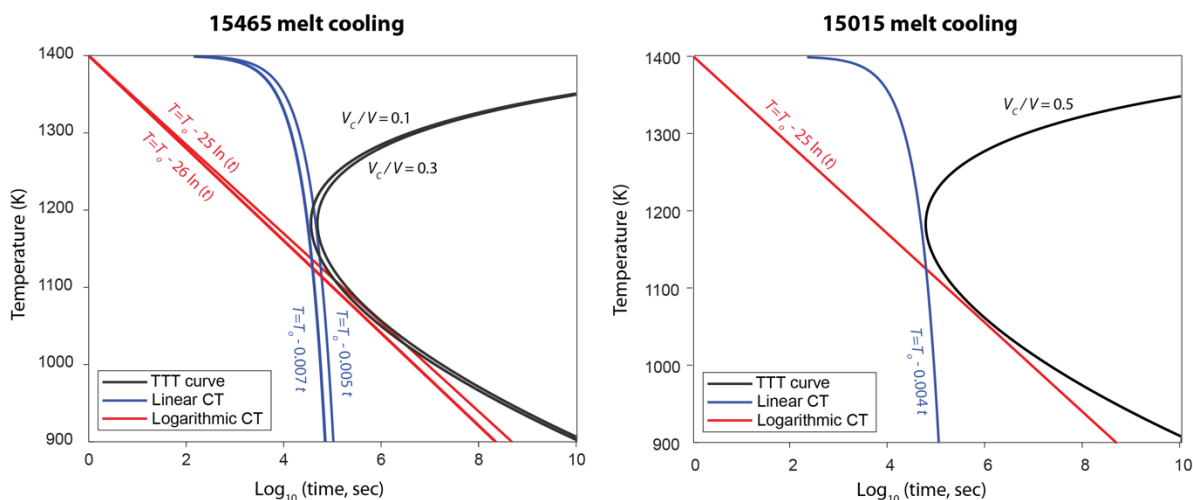


Fig. S4. Estimated melt cooling rate for breccias 15465 and 15015. Black curves are TTT calculations depicting time-temperature conditions for producing crystal fractions of $V_C/V = 0.1$ - 0.3 for 15465 (fig. S1) and 0.5 for 15015 (fig. S2). Blue and red lines depict linear and logarithmic cooling curves, respectively. These calculations assume a glass composition like that of regolith breccia 15498 (59). The estimated linear cooling times from 800°C to 0°C for 15465 and 15015 are 31-44 hours and 54 hours, respectively.

similar composition to 15465 and 15015 glasses (table S1). Based on our petrographic observations (figs. S1 and S2), the crystal fractions (V_C/V) in equation (S1) for 15465 and 15015 are ~ 0.1 - 0.3 and ~ 0.5 , respectively.

Figure S4 shows the TTT and CT curves for breccias 15465 and 15015 for these parameters. Based on the estimated B values, it took a minimum of 31-44 h for 15465 and 54 h for 15015 to linearly cool from the kamacite Curie point to lunar surface temperatures (table S2). The predicted logarithmic cooling times for both breccias are much longer (e.g., ~ 50 - 100 days for cooling from 800 to 400°C given the estimated C values).

Table S2. Estimated cooling rate for 15465 and 15015 lunar rock compositions.

Sample	Liquidus temperature (K)	Crystal fraction	B (K s ⁻¹)	Cooling time (h)
15465	1543	0.1-0.3	0.005-0.007	31-44
15015	1543	0.5	0.004	54

Note: The first column lists the sample name, the second column lists the liquidus temperature in K, the third column lists the volume fraction of crystallized glass over the total glass volume. The fourth column lists the linear cooling rate, B . The fifth column lists the linear cooling time from 780 °C (i.e., the kamacite Curie temperature) to the lunar surface temperature (0 °C).

2.3. Heat conduction in clast-bearing melt. After breccia formation, the glassy melt welded and heated the clasts. We now assess whether the clast fragments' temperatures would have exceeded the kamacite Curie temperature such that part or all of their volumes would have completely remagnetized during breccia formation. Depending on the thermal diffusivity of the clast and the melt cooling rate during breccia formation (see section 2.2), different regions inside a single clast may have experienced different peak temperatures. Given their basaltic compositions (19), we assume a thermal diffusivity $k = 4 \times 10^{-7} \text{ m}^2 \text{ s}^{-1}$ (59).

We consider two extreme scenarios for heating of a clast after it is placed in contact with the glassy melt. Initially, the clast and melt are at the ambient lunar surface (0 °C) and liquidus temperature (1270 °C), respectively. In scenario 1, we consider a one-dimensional (1D) geometry in which the melt and clast are in contact on one side of the clast, while the other side of the clast is exposed to the lunar vacuum (fig. S5). In scenario 2, we consider a two-dimensional geometry in which the melt surrounds a spherical clast on all sides (fig. S6). For each scenario, we estimate the peak temperature as a function of position within the clast resulting from conductive heating by the cooling melt. Because the melt cooling rate is constrained by the cooling rate calculations in section 2.2, our calculations do not require knowledge of the total melt volume.

2.3.1. Scenario 1. Considering the geometry in the inset for fig. S5A, we consider the following 1D unsteady heat-transport equation (66)

$$\frac{\partial T}{\partial t} = k \frac{\partial^2 T}{\partial x^2} \quad (\text{S4})$$

where x , t , T are position, time, temperature, respectively. In particular, we examine a ~20 mm diameter clast like that in our 15465 sample. We assume that its right boundary is in contact with the lunar vacuum and held constant at 0 °C while its left boundary is in contact with the melt cooling at either a linear or logarithmic rate (section 2.2). We solved for the spatiotemporal evolution of the clast's temperature using finite difference discretization of equation (S4). The results (fig. S5) indicate that, depending on the melt cooling rate, clast material at depths of ≤ 5 mm (logarithmic rate) to ≤ 7 mm (linear rate) from the exterior of the clast adjacent to the melt wall would have been completely remagnetized by heating above the kamacite Curie temperature.

2.3.2. Scenario 2. In the second scenario, the isothermal surfaces take the form of concentric spheres and the temperature is only radially-dependent. Therefore, the unsteady differential equation for heat transport in spherical coordinates reduces to (67)

$$\frac{\partial T'}{\partial t} = k \frac{\partial^2 T'}{\partial r^2} \quad (\text{S5})$$

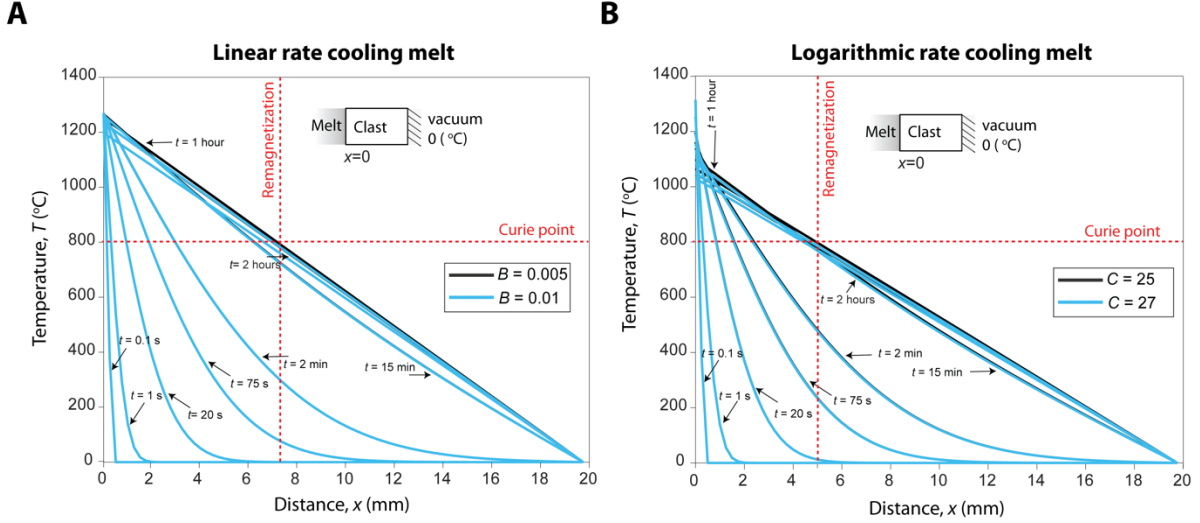


Fig. S5. Temperature distribution inside a clast with a one-dimensional contact with a cooling melt. Blue curves depict temperature T as a function of time t in the clast following cooling from initial temperature T_0 . **(A)** Assuming a linear glass cooling rate: $T = T_0 - Bt$. **(B)** Assuming a logarithmic glass cooling rate: $T = T_0 - C \ln(t)$. Insets in (A) and (B) show the cooling geometry. The left and right boundaries of the clast are in contact with diffusively cooling melt and the lunar surface vacuum, respectively. The horizontal red dashed line indicates the kamacite Curie temperature. Between ~ 5 (B) to ~ 7 (A) mm of the 20-mm diameter clast considered here would remagnetize during the breccia formation (shown by the vertical red dashed lines).

where r is radius and $T' = T \cdot r$.

As an example, let us apply this to a clast with a radius of $a = 5$ mm. The clast boundary (clast-melt wall) temperature varies as $T = A - Bt$, with an initial value at $A = 1270$ °C and linear decay rate $B = 0.005$ to 0.01 °C s^{-1} (see section 2.2). Ref. (67) presented an analytical formula for this special case with a linearly-cooling boundary

$$T = A + \frac{2aA}{\pi r} \sum_{n=1}^{\infty} \frac{(-1)^n}{n} \sin \frac{n\pi r}{a} e^{-\frac{kn^2\pi^2 t}{a^2}} + B \left[t - \frac{a^2 - r^2}{6k} \right] - \frac{2Ba^3}{k\pi^3 r} \sum_{n=1}^{\infty} \frac{(-1)^n}{n^3} \sin \frac{n\pi r}{a} e^{-\frac{kn^2\pi^2 t}{a^2}} \quad (\text{S6})$$

Figure S6A shows the spatiotemporal evolution of the temperature inside this clast using the analytical expression in equation (S6). The entire clast reaches the kamacite Curie temperature and remains above this temperature for more than 2 hours. This means that any clasts with radii of less than 5 mm would be completely remagnetized by the heat conduction from the melt.

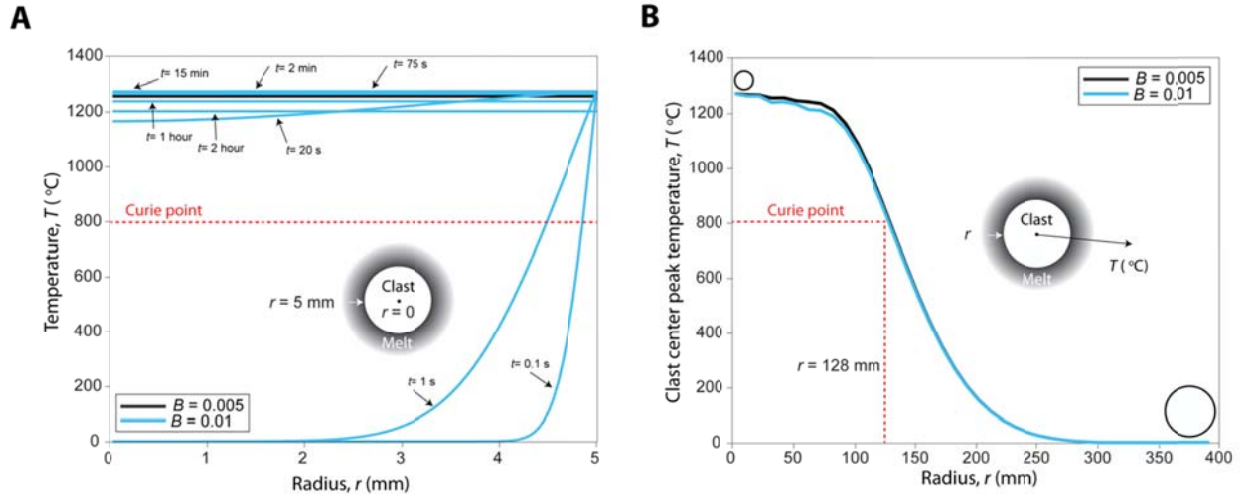


Fig. S6. Temperature distribution inside a spherical clast surrounded by a linearly cooling melt. (A) Blue curves depict temperature T as a function of time t in the clast following cooling from initial temperature T_0 assuming a linear glass cooling rate ($T = T_0 - Bt$). Inset shows the cooling geometry: the spherical clast is surrounded by an infinite melt medium. The horizontal red dashed line denotes the kamacite Curie point. The entire clast with a radius of 5 mm would remagnetize by heating above its Curie temperature. (B) Peak temperature at the clast's center as a function of the radius of the clast. A clast with a maximum radius of 128 mm (vertical red dashed line) would entirely remagnetize during the breccia formation.

Using the same analytical expression, we can also estimate the maximum radius of a spherical clast that would be totally remagnetized by heating entirely (even to its center) above the Curie temperature (fig. S6B). Our calculations show that this critical radius is ~ 130 mm. This means that any clasts with radii smaller than this value would be entirely remagnetized.

2.3.3. Synthesis. The results in figs. S5 and S6 would slightly vary for the range cooling rates that we obtained in section 2.2 for our two breccias. However, the overall clast remagnetized region dimensions remain the same. Nevertheless, the calculations presented in scenarios 1 and 2 have some uncertainties. The first is the value of thermal diffusivity in our calculations. The presence of pores could decrease the clasts' thermal diffusivity, which would modify the results. For example, reducing the thermal diffusivity by a factor of 8 (i.e., to $0.5 \times 10^{-7} \text{ m}^2 \text{ s}^{-1}$) would reduce the remagnetized region by $\sim 50\%$. Another source of uncertainty derives from the simplified geometries which only approximate those of our samples.

Our clast subsamples in breccia 15465 were sampled from a large ~ 20 mm diameter regolith breccia clast. Table S3 shows the distance between the melt wall to the most distal point within the clast (related to scenario 1) and also to the center of the clast (related to scenario 2) for 15465 clast subsamples. Considering the uncertainties, the calculations for scenario 1 would imply that parts of the interior of this 20-mm diameter clast (see fig. S7) may not have been completely remagnetized at the time of breccia formation. On the other hand, the results for scenario 2 would imply that the clast would have been completely remagnetized. Our visual observations of the original 15465,0 sample (based on JSC photos S71-44188 and S-71-44190) suggest that the clast studied here (fig. S1) is part of a larger clast that was not surrounded by melt and could well

Table S3. Distances between 15465 matrix glass melt interface and our clast subsamples.

Distance (mm)	15465 Clast 6-2	15465 Clast 6-3	15465 Clast 8-2
From center	1.6	1.5	1.8
From farthest point	3.9	2.5	2.8

Note: The second row indicates the distance between clast's center and melt glass. The third row indicates the distance between the farthest point on the clast from the melt. Refer to fig. S7 for a visual description of the subsamples.

have been in contact with the Moon's surface. Therefore, scenario 1 is likely more representative of this geometry. If more than one face were exposed to the surface (fig. S7), the calculations would overestimate the clast's remagnetized region. The absence of melt residues on our studied large clast (fig. S7) is further evidence for the relevance of scenario 1. Therefore, it is likely that some of our deeper clast subsamples may not have been remagnetized during breccia formation and still contain a record of the lunar paleofield from an earlier epoch (in particular, subsamples 6-2 and 8-2, which are distal from the melt wall).

On the other hand, the clasts in breccia 15015 are all <0.1 to 7 mm in diameter and were surrounded by melt (e.g., subsamples 229a1a and 229a1g), which indicates scenario 2 is appropriate for this sample. This indicates that the clasts in this breccia would essentially have been entirely remagnetized during breccia formation. Consistent with this conclusion, the depletion of He, N₂, and C and the enrichment of ¹³C and ¹⁵N observed in clast fragments of 15015,15, is similar to that of nearby soil, indicating that the clast fragments in this breccia may have been heated to at least ~800 °C (57).

Section S3. NRM

3.1. Introduction. All of our paleomagnetic and most rock magnetic analyses were conducted using a 2G Enterprises Superconducting Rock Magnetometer (SRM) 755 inside the MIT Paleomagnetism Laboratory's magnetically shielded room (< 200 nT). The 3-standard deviation noise level of this magnetometer is 9.9×10^{-13} Am² [fig. S5 of ref. (68)], which is less than 2% of the weakest measured moment reported in this paper. We prepared mutually-oriented subsamples of 15465 and 15015 in this shielded room using a wire saw previously shown to not measurably disturb the NRM of lunar samples (8).

We analyzed both glass and clast lithologies of each breccia. Static three-axis alternating field (AF) demagnetization of NRM was conducted up to a maximum AF of 145 mT for most subsamples (and in some cases, to 290 mT). To mitigate the acquisition of gyroremanent magnetization (GRM) (9, 25, 69), we measured the moment after AF application along each orthogonal axis and then averaged the components for a given AF level following the Zijderveld-Dunlop method (70). To reduce contributions from spurious anhysteretic remanent magnetization (ARM) resulting from imperfections in the AF waveform (9, 25, 69), we also conducted repeat applications of the AF at higher steps and included these extra steps in the averaging process. Thermal demagnetization and thermal paleointensity experiments were conducted up to 780 °C in a controlled-atmosphere oven (27) at an oxygen fugacity set to the estimated formation conditions of lunar materials [0.5-1 log units below the iron-wüstite (IW) buffer] (28, 29). We maintained this oxygen fugacity during the heating and cooling process using continuously-adjusted mixtures of CO₂ and H₂.

We estimated NRM components using principle component analysis (PCA) (71). Tests for origin-trending components were conducted by comparing the maximum angular deviation (MAD) to the deviation angle (DANG) (72). We now describe the nature and origin of the NRM in individual subsamples of 15465 and 15015.

3.2. Breccia 15465

3.2.1. Overview. Our 15465 subsamples were taken from the 3.767 g parent split 115, which we chipped from parent mass 44 at NASA Johnson Space Center (JSC) and then shipped to MIT in a magnetically shielded can in April 2015. The entire parent 15465, including our piece 115, had never been previously cut or exposed to a saw at JSC. At MIT, we prepared 11 subsamples from split 115 oriented with respect to the parent 44 mass using the same orientation system (N-S-E-W) as that of the parent breccia at JSC.

Our subsamples consisted of 8 matrix-glass-rich samples and 3 subsamples from a single ~20 mm diameter regolith breccia clast (fig. S7). Although some of the “glass” subsamples contain tiny clast fragments (≤ 300 μm diameter) enclosed within the melt (e.g., subsample 3-2 in fig. S7), our thermal analyses in section 2 showed that these melt-surrounded clast fragments (smaller than the critical 128 mm radius in fig. S6) would remagnetize during the glass formation event. The large clast itself is a regolith breccia composed of glass-welded fragments (fig. S1). We applied AF demagnetization and non-thermal paleointensity experiments to 8

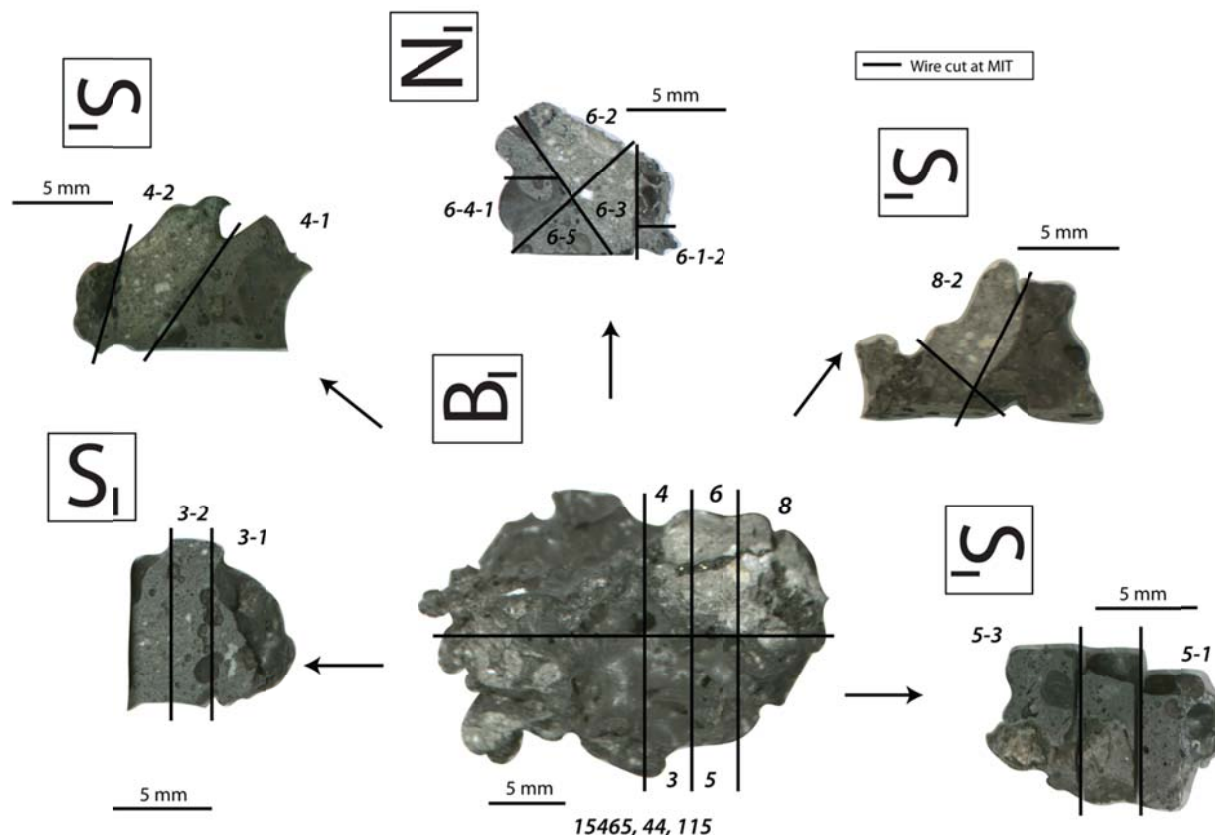


Fig. S7. Location of our 15465 subsamples relative to the parent sample 15465, 44, 115.

Dark homogenous material is matrix glass and light grey is clast material. Scale bar in each image is 5 mm. Subsample names are labeled. Subsamples 6-2, 6-3, and 8-2 are all sampled from a single 20-mm diameter regolith breccia clast (light grey) (see also fig. S1). The orientation cube shows the JSC orientation system, which is adopted in this study.

Table S4. NRM components during AF or thermal demagnetization for 15465 subsamples.

Subsample	Lithology	Mass (mg)	Component	Range	Dec, Inc (°)	MAD (°)	DANG (°)	N	Orientation (°)
3-2	Glass	86	LC	NRM-3 mT	40.9, 9.0	16.4		6	270, 90
			HC	3-145 mT	36.2, -24.9	42.1	52.0	145	
4-1	Glass	249	LC	NRM-10 mT	314.6, -41.0	15.1		20	270, 90
			HC	10-290 mT	245.7, 11.0	39.2	135.2	142	
4-2	Glass	105	LC	NRM-9 mT	105.6, -19.1	14.5		18	270, 90
			HC	9-290 mT	235.8, -24.9	38.5	32.2	144	
5-1	Glass	88	LT	NRM-390 °C	46.1, 14.9	12.7		10	270, 90
			HT	390-730 °C	168.7, 23.4	44.4	76.9	8	
5-3	Glass	109	LT	NRM-330 °C	30.0, 46.7	7.1		7	270, 90
			HT	330-730 °C	318.1, 72.6	31.7	67.0	11	
6-1-2	Glass	7	LC	NRM-10 mT	117.1, 55.4	20.3		20	270, 90
			HC	10-145 mT	294.2, -7.5	37.1	22.3	131	
6-2	Clast	59	LC	NRM-65 mT	184.1, -0.7	10.0		90	270, 90
			HC	65-145 mT	104.1, -28.5	38.4	11.1	61	
6-3	Clast	56	LC	NRM-16 mT	181.1, 17.9	11.0		32	90, 90
			HC	16-145 mT	353.7, -11.7	23.8	154.6	119	
6-4-1	Glass	27	LC	NRM-9.5 mT	181.1, -51.8	14.1		19	90, 90
			HC	9.5-145 mT	240.8, 41.6	38.0	10.91	132	
6-5	Glass	33	LC	NRM-10 mT	178.1, -66.7	24.0		20	90, 90
			HC	10-145 mT	108.7, -18.9	39.1	11.3	29	
8-2	Clast	28	LT	NRM-200 °C	172.6, 26.3	10.1		4	270, 90
			HTC	200-730 °C	198.2, 30.3	16.4	14.6	14	

Notes: The first and second columns list the subsample name and its lithology. The third column lists the mass. The fourth column lists the natural remanent magnetization (NRM) components and the fifth column lists their alternating field (AF) level or unblocking temperature ranges. The sixth, seventh, and eighth columns list declination and inclination in sample coordinates (e.g., fig. S7), maximum angular deviation (MAD) and deviation angle (DANG) for fits using principal component analysis (PCA). The eighth column lists the number of data points used during the PCA fit. The last column lists the right-hand strike and dip of the subsamples' top faces during the magnetic measurements (see fig. S7).

subsamples (6 and 2 from the glass and clast lithologies, respectively) while the remaining 3 subsamples (2 and 1 from the glass and clast lithologies, respectively) were subjected to thermal demagnetization and thermal paleointensity experiments. Table S4 summarizes the demagnetization components for all subsamples and fig. S8 depicts their directions inferred from PCA.

3.2.2. Glass subsamples. We found that all glass subsamples have a low coercivity (LC), low temperature (LT) component that demagnetized by ~3-10 mT and 330-390 °C, respectively. These components are collectively non-unidirectionally oriented across the parent sample. The LC/LT components' low peak unblocking AF levels and temperatures and scattered directions (fig. S8A) indicate that they are secondary in origin. The magnitude of these components is comparable to that expected to have been acquired VRM in the geomagnetic field (section 5). Therefore, it is likely that these overprints are VRMs acquired as the sample was rotating randomly during its storage and maintenance at JSC (9). Two other possibilities are that LC/LT components are due to either modest physical contamination of the samples and/or to exposure to stray fields during handling by the astronauts or at JSC [e.g., ref. (34)].

After removal of the LC/LT components, the NRMs did not further decay in magnitude or maintain a consistent direction during subsequent AF and thermal demagnetization in the HC (~10 to 145 or ~10 to 290 mT) and (390-780 °C) HT ranges (figs. 1A and B, S9A and B, S10A). The largely scattered directions inferred from PCA fits to this range (fig. S8B), the associated large

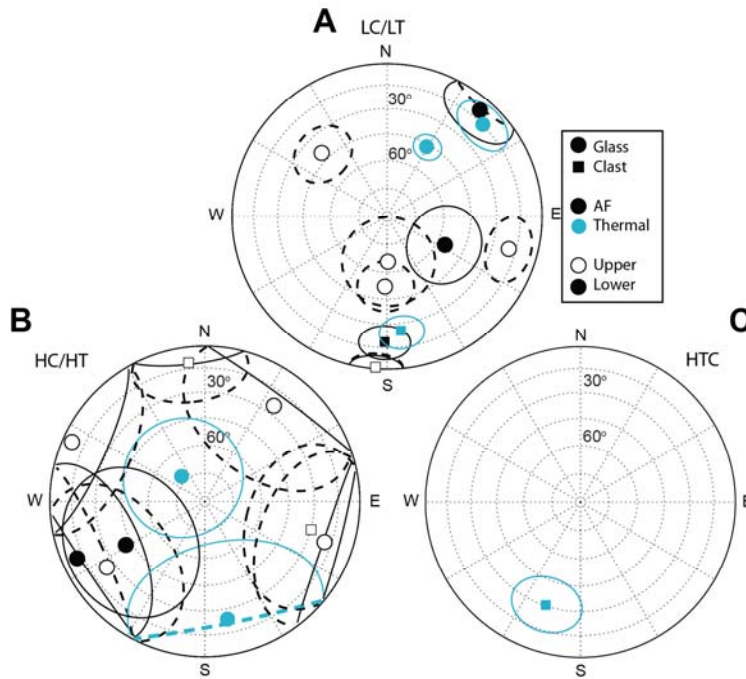


Fig. S8. Magnetization directions in 15465 inferred from PCA. Shown are equal area stereographs, with open symbols and dashed lines representing the upper hemisphere and closed symbols and solid lines represent the lower hemisphere. Ellipses show the 95% formal confidence intervals on mean directions using PCA. (A) Low coercivity (LC)/low temperature (LT) components. (B) High coercivity (HC)/high temperature (HT) ranges. (C) High temperature clast (HCT) component. Black and blue symbols denote the components obtained from AF and thermal demagnetization, respectively. Squares and circles denote clast and glass subsamples, respectively.

(>20-30°) MAD angles, the non-origin trending nature (i.e., $DANG > MAD$ for most subsamples) (table S4) (72), and paleointensities mostly within error of zero field (section 4) indicate that there is no stable NRM in the HC/HT range. The lack of NRM is not due to destruction of ferromagnetic carriers in our heating experiments as demonstrated by the fact that measurements of partial thermoremanent magnetization (pTRM) acquisition in our paleointensity experiments showed that there was no significant thermochemical alteration up to 730 °C (section 4).

3.2.3. Clast subsamples. We also identified LC and LT components in the clast subsamples. Unlike for the matrix glass subsamples, we found that the LC components in two clast subsamples that were AF-demagnetized (6-2 and 6-3) were broadly unidirectional (fig. S8) and unblocked at higher AF levels of ~16-65 mT (fig. S9). Like the matrix glass, the HC ranges for these subsamples did not contain origin-trending HC components, with PCA fits again exhibiting large MAD values (>20°) and fit directions separated by >100° (fig. S8B and fig. S9C and D).

Thermal demagnetization of a third clast subsample (8-2) isolated an LT component that unblocked by 200 °C (fig. S10B). Unlike all other subsamples of 15465, this subsample also was found to contain an origin-trending component that unblocked between 200-780 °C offset by ~20° from the directions of the LC/LT components in the three subsamples (figs. S8 and S10B). We name this the high temperature clast (HTC) component. We also note that the nonzero

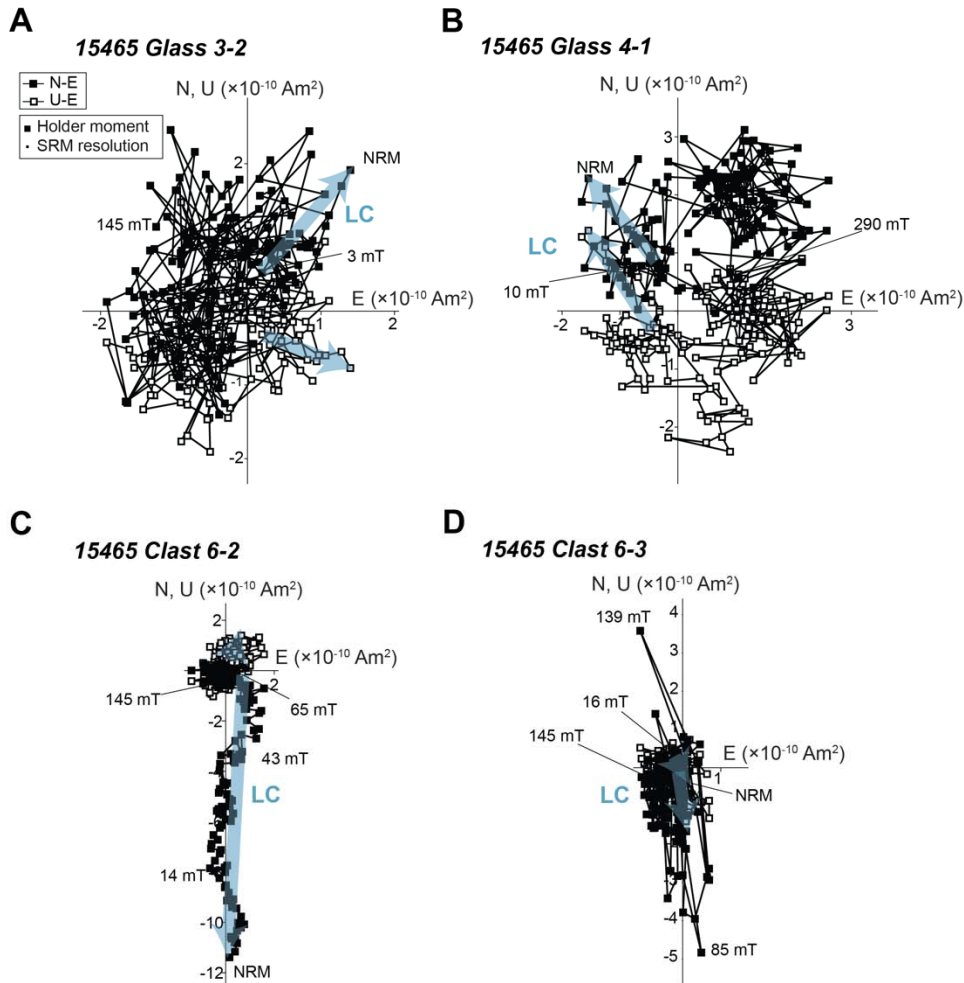


Fig. S9. AF demagnetization of 15465. (A) Glass subsample 15465-3-2. (B) Glass subsample 15465-4-1. (C) Clast subsample 15465-6-2. (D) Clast subsample 15465-6-3. Closed and open symbols represent the projections of the natural remanent magnetization (NRM) vectors onto the horizontal (N-E) and vertical (U-E) planes, respectively. Legend in (A) shows the sample holder magnetic moment along with the MIT superconducting rock magnetometer (SRM) resolution (section 3). Low coercivity (LC) components are denoted by blue arrows. NRM and AF levels for selected steps are labeled. The LC components for 15465 glass subsamples (A and B) unblock by ~3 to 10 mT, while the LC components for clasts (C and D) unblock by AF levels of ~16-65 mT.

paleointensity for the high-coercivity range for 6-2 (table S6 and section 4) hints that it might too contain a weak component.

The LC/LT components are likely VRMs or other secondary overprints like those observed in the matrix glass subsamples (section 3.2.2). Furthermore, as with the glass subsamples, the HC range in 6-3 record zero-field conditions during assembly of 15465. By comparison, the high thermal stability of the HTC component suggests it may be an ancient remanence from the dynamo, which was active at the time of formation of clasts in 15465 (>3.4 to 3.9 Ga; see section 7). In particular, as discussed in section 2.3, when the clast was enveloped by the matrix melt, some clast material distal from the melt may have escaped heating above its Curie temperature. Therefore,

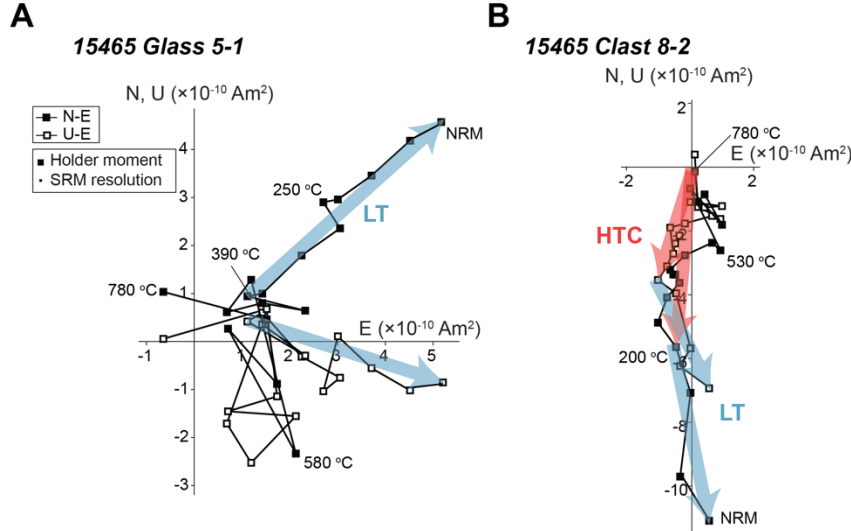


Fig. S10. Thermal demagnetization of 15465. (A) Glass subsample 5-1. (B) Clast subsample 8-2. Closed and open symbols represent the projection of natural remanent magnetization (NRM) vectors onto the horizontal (N-E) and vertical (U-E) planes, respectively. Legend in (A) shows the sample holder magnetic moment along with the MIT superconducting rock magnetometer (SRM) resolution (section 3). Low temperature (LT) and high temperature clast (HTC) components are denoted by blue and red arrows, respectively. NRM and selected temperature steps are labeled. The LT component for the 15465 matrix glass subsample (A) unblocks by 390 °C and has no discernible origin-trending HT component. The clast subsample (B) shows an HTC component that is stable and origin-trending up to 780 °C.

portions of the clast may not have been remagnetized during assembly of 15645. Note that uncertainties associated with the thermal modeling in section 2.3 (stemming from the simplified geometry and uncertainties in the clast cooling rate and boundary condition) can account for the lack of HTC remanence in subsample 6-2, which contains clast material both near and far from the melt wall.

3.3. Breccia 15015

3.3.1. Overview. Our 15015 subsamples were taken from 6.044 g parent split 229 which we chipped from parent mass 12 at NASA Johnson Space Center and then shipped in a magnetically shielded can to MIT in March 2015. Our subsamples are in the same orientation system (N-S-E-W) as the parent breccia and use the JSC orientation system. Unlike 15465, our 15015 parent sample (229) had two faces that were previously cut with a bandsaw at JSC (fig. S11). We prepared 25 subsamples from both near and away from these bandsawn surfaces. We applied AF demagnetizations on 22 subsamples (20 and 2 with matrix glass and composite clast-glass lithologies, respectively). We also conducted controlled-atmosphere thermal demagnetization experiments on the remaining 3 subsamples, all of which are from the matrix glass lithology.

Table S5 summarizes the demagnetization components for all subsamples and fig. S12 depicts their directions. Among the samples with edges cut with the JSC bandsaw, a total of 10 and 1 were from the glass and the clast lithologies, respectively. Unlike the large clast in breccia 15465, which was not surrounded by melt on all sides, the clast fragments in split

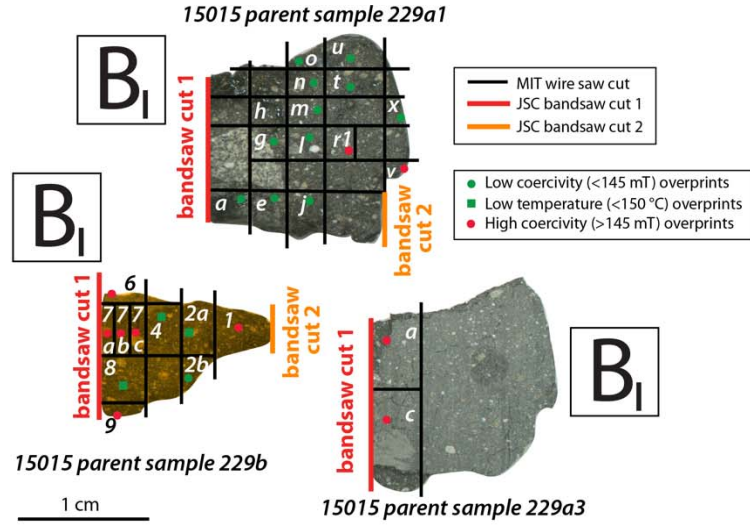


Fig. S11. Location of our 15015 subsamples and cuts relative to the parent samples 229a1, 229a3, and 229b. Dark material is matrix glass and light grey is clast material. Green symbols indicate subsamples whose overprints were successfully completely removed via alternating field (AF) (circles) or thermal (squares) demagnetization. Red symbols indicate subsamples whose overprints persisted at high AF levels (145 mT) and could not be completely demagnetized. Black lines denote wiresaw cuts at MIT, while red and orange lines denote two JSC bandsaw (BS) cut surfaces. The orientation cube shows the JSC orientation system which is adopted in this study.

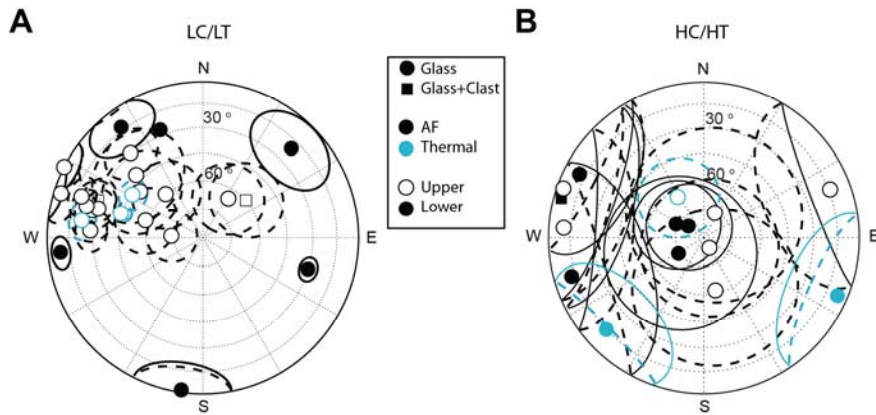


Fig. S12. Magnetization directions in 15015 inferred from PCA. Shown are equal area stereographs, with open symbols and dashed lines representing the upper hemisphere and closed symbols and solid lines represent the lower hemisphere. Ellipses denote the 95% formal confidence intervals on mean directions using PCA. (A) Low coercivity (LC)/low temperature (LT) components. (B) High coercivity (HC)/high temperature (HT) ranges. Black and blue symbols denote the components obtained from AF and thermal demagnetization, respectively. Squares and circles denote composite clast-glass and glass subsamples, respectively.

229 were enveloped by melt and are <1 mm in diameter except for a single ~7 mm diameter sub-angular clast fragment (fig. S11). Our clast and composite clast-glass samples both contained material from the latter ~7 mm clast. Our thermal calculations (fig. S6) indicate that all of these melt-enveloped clasts should have been completely remagnetized during breccia formation.

3.3.2. Glass subsamples. Our AF and thermal demagnetization showed that 15015 matrix glass subsamples contained LC/LT magnetization components with a wide range of peak unblocking

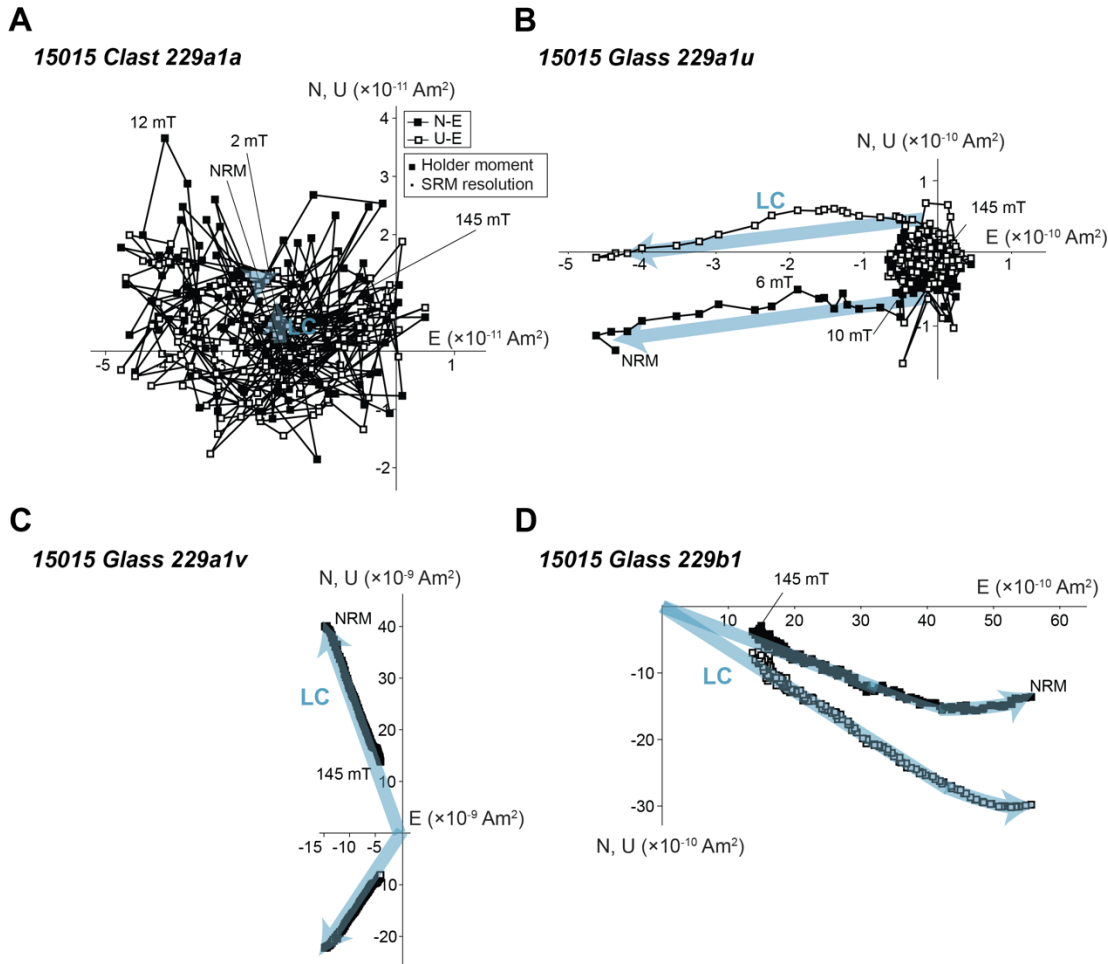


Fig. S13. AF demagnetization of 15015 glass subsamples. (A) 15015 clast subsample 229a1a. (B) 15015 glass subsample 22a1u. (C) 15015 glass subsample 229a1v. (D) 15015 glass subsample 229b1. Closed and open symbols represent the projection of natural remanent magnetization (NRM) vectors onto the horizontal (N-E) and vertical (U-E) planes, respectively. Lower legend in (A) shows the sample holder magnetic moment along with the MIT superconducting rock magnetometer (SRM) resolution (section 3). Low coercivity (LC) components are denoted by blue arrows. NRM and AF levels for selected steps are labeled. The LC components for 15015 glass subsamples in (A) and (B) unblock by 2 to 10 mT. The subsamples in (C) and (D) are nearest (within ≤ 2.7 mm) to the edges that were cut with a bandsaw at Johnson Space Center (JSC). They show a significant overprint by the generated heat during the bandsaw cutting. The overprint LC components in (C) and (D) are origin-trending and yet not unblocked by 145 mT AF level (see section 3).

AF levels, peak unblocking temperatures, and intensities (table S5). Note that although we use the same “LC” and “LT” acronyms to denote the low-stability components for both 15015 and 15465, this is not intended to imply that the origin for these components in the two breccias is the same. The LC/LT components in subsamples located more than ~ 3.4 mm farther away from the JSC bandsawn face unblocked by ~ 2 -16 mT (figs. S13A and B). The LC/LT components for the samples closer to the bandsawn face (~ 2.7 mm < distance < ~ 3.4 mm) demagnetized by 16-45 mT, with the 10 subsamples closest to the edge (distance < ~ 2.7 mm) not even fully unblocked by 145 mT (figs. S13C and D). Thermal demagnetization of all subsamples including those closest to the bandsawn edge (fig. S14) removed a LT component by just 150 °C.

Glass and clast-glass lithologies demagnetized in a very similar manner. LC components from samples within ~ 2.7 mm of the sawcut surfaces were origin-trending while those from deeper samples were weaker and not origin-trending (fig. S13). Another notable observation is that both the intensities and directions of the LC/LT components in a given subsample correlate with the subsample’s relative position in the parent sample; collectively, the directions continuously rotate by $\sim 180^\circ$ over a traverse from the extreme bandsawn edge on the E side to that on the W, while sample intensities weaken progressing into the interior from both the E or W bandsawn edges (fig. S15). These observations indicate that the LC/LT components are not total TRMs of lunar origin. Given that it has been established that cutting with large saws at JSC, which is usually conducted without lubricant, can heat samples >150 °C at a depth of ~ 3 mm beneath the sawn surface (8),

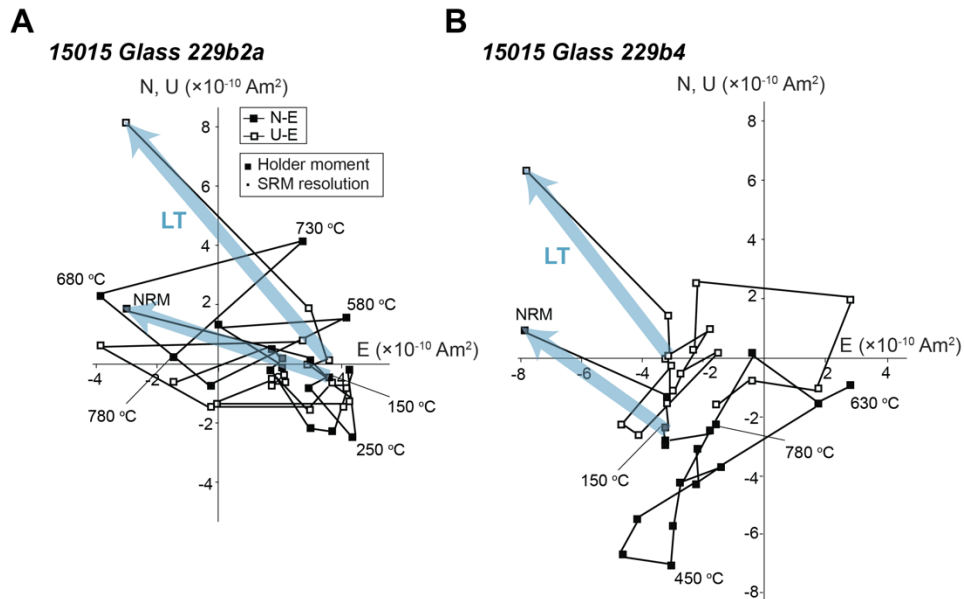


Fig. S14. Thermal demagnetization of 15015 subsamples. (A) Subsample 15015-229b2a. **(B)** Subsample 15015-229b4. Closed and open symbols represent the projection of natural remanent magnetization (NRM) vectors onto the horizontal (N-E) and vertical (U-E) planes, respectively. Lower legend in (A) shows the sample holder magnetic moment along with the MIT superconducting rock magnetometer (SRM) resolution (section 3). Low temperature (LT) component is denoted by a blue arrow. The NRM and selected temperature steps are labeled. The LT components for 15015 glass subsamples (A and B) unblock by 150 °C and there is no discernible origin-trending high temperature (HT) component.

Table S5. NRM components during AF or thermal demagnetization for 15015 subsamples.

Subsample	Lithology	Mass (mg)	Saw cut distance (mm)	Component	Range	Dec, Inc (°)	MAD (°)	DANG (°)	N	Orientation (°)
229a1a*	Clast	29	0	LC	NRM-2 mT	187.5, 1.2	17.9		4	90, 0
				HC	2-145 mT	289.3, -5.1	43.2	2.8	147	
229a1e	Glass	29	3.4	LC	NRM-22 mT	33.4, -65.4	18.7		44	90, 0
				HC	22-145 mT	24.7, -75.9	47.0	112.1	107	
229a1g	Clast-Glass	28	3.4	LC	NRM-18 mT	49.3, -59.3	19.4		36	90, 0
				HC	18-145 mT	285.4, 6.6	42.9	11.9	115	
229a1j	Glass	51	4.2	LC	NRM-13.5 mT	286.6, -58.6	16.8		27	90, 0
				HC	13.5-145 mT	150.1, -83.6	36.6	29.2	123	
229a1l	Glass	36	5.8	LC	NRM-45 mT	319.8, -60.0	17.8		70	90, 0
				HC	45-145 mT	253.5, 12.8	46.8	9.1	81	
229a1m	Glass	26	5.8	LC	NRM-16 mT	272.8, -73.7	13.3		32	90, 0
				HC	16-145 mT	237.0, 74.4	40.9	71.1	119	
229a1n	Glass	15	5.8	LC	NRM-23.5 mT	306.5, -48.8	21.3		47	90, 0
				HC	23.5-145 mT	306.9, 80.2	22.6	98.9	104	
229a1o	Glass	-	5.8	LC	NRM-2.5 mT	287.4, -5.3	11.7		5	90, 0
				HC	2.5-145 mT	297.1, 11.4	33.4	14.7	146	
229a1r1	Glass	24	2.6	LC	NRM-145 mT	45.0, 20.4	19.9		150	90, 0
229a1t	Glass	18	6.8	LC	NRM-30 mT	283.8, -28.1	14.0		55	90, 0
				HC	30-145 mT	273.9, -10.8	41.6	126.1	96	
229a1u	Glass	11	8.6	LC	NRM-10 mT	263.8, 9.1	6.5		20	90, 0
				HC	10-145 mT	167.2, -61.3	43.0	79.2	131	
229a1v	Glass	-	0	LC	NRM-145 mT	338.4, 26.7	1.6		150	90, 0
229a1x	Glass	9	5.1	LC	NRM-43 mT	323.4, 13.1	15.1		68	0, 90
				HC	43-145 mT	69.2, -13.8	41.0	144.7	83	
229a3a	Glass	83	0	LC	NRM-145 mT	273.6, -28.6	9.6		150	90, 0
229a3c*	Clast-Glass	90	0	LC	NRM-145 mT	289.6, -29.4	10.3		150	90, 0
229b1	Glass	42	0	LC	NRM-145 mT	106.8, 29.9	5.5		150	90, 0
229b2a	Glass	60	5.3	LT	NRM-150 °C	287.1, -46.7	3.7		3	0, 90
				HT	150-780 °C	113.5, 6.5	33.0	11.3	16	
229b2b	Glass	15	5.3	LC	NRM-39 mT	313.4, -41.1	24.1		64	90, 0
				HC	39-145 mT	296.4, 74.1	23.1	23.0	87	90, 0
229b4	Glass	45	2.6	LT	NRM-150 °C	301.5, -46.2	7.6		3	180, 90
				HT	150-780 °C	226.4, 14.9	30.7	13.1	16	
229b6	Glass	27	0	LC	NRM-145 mT	285.7, -31.3	8.9		150	90, 90
229b7a	Glass	13	0	LC	NRM-145 mT	285.1, -23.9	7.6		150	180, 90
229b7b	Glass	16	0.8	LC	NRM-145 mT	297.0, -0.3	10.1		150	180, 90
229b7c	Glass	15	2.1	LC	NRM-145 mT	319.5, -29.5	13.2		150	180, 90
229b8	Glass	61	0	LT	NRM-150 °C	278.1, -22.7	8.5		3	270, 180
				HT	150-780 °C	327.8, -64.7	21.1	33.9	16	
229b9	Glass	7	0	LC	NRM-145 mT	288.8, -19.1	8.7		150	90, 0

Notes: The first and second columns list the subsample name and its lithology. The third column lists the distance of the subsample edge from the closest JSC saw cut face. The fourth column lists the natural remanent magnetization (NRM) components and the fifth column lists their alternating field (AF) level or unblocking temperature ranges. The sixth, seventh, and eighth columns list declination and inclination in sample coordinates (e.g., figs. S11 and S15), maximum angular deviation (MAD) and deviation angle (DANG) for fits using principal component analysis (PCA) fit. The ninth column lists the number of data points used during the PCA fit. The last column lists the right-hand strike and dip of the subsamples' top faces during the magnetic measurements (see figs. S11 and S15).

*These subsamples contain material from the same parent clast.

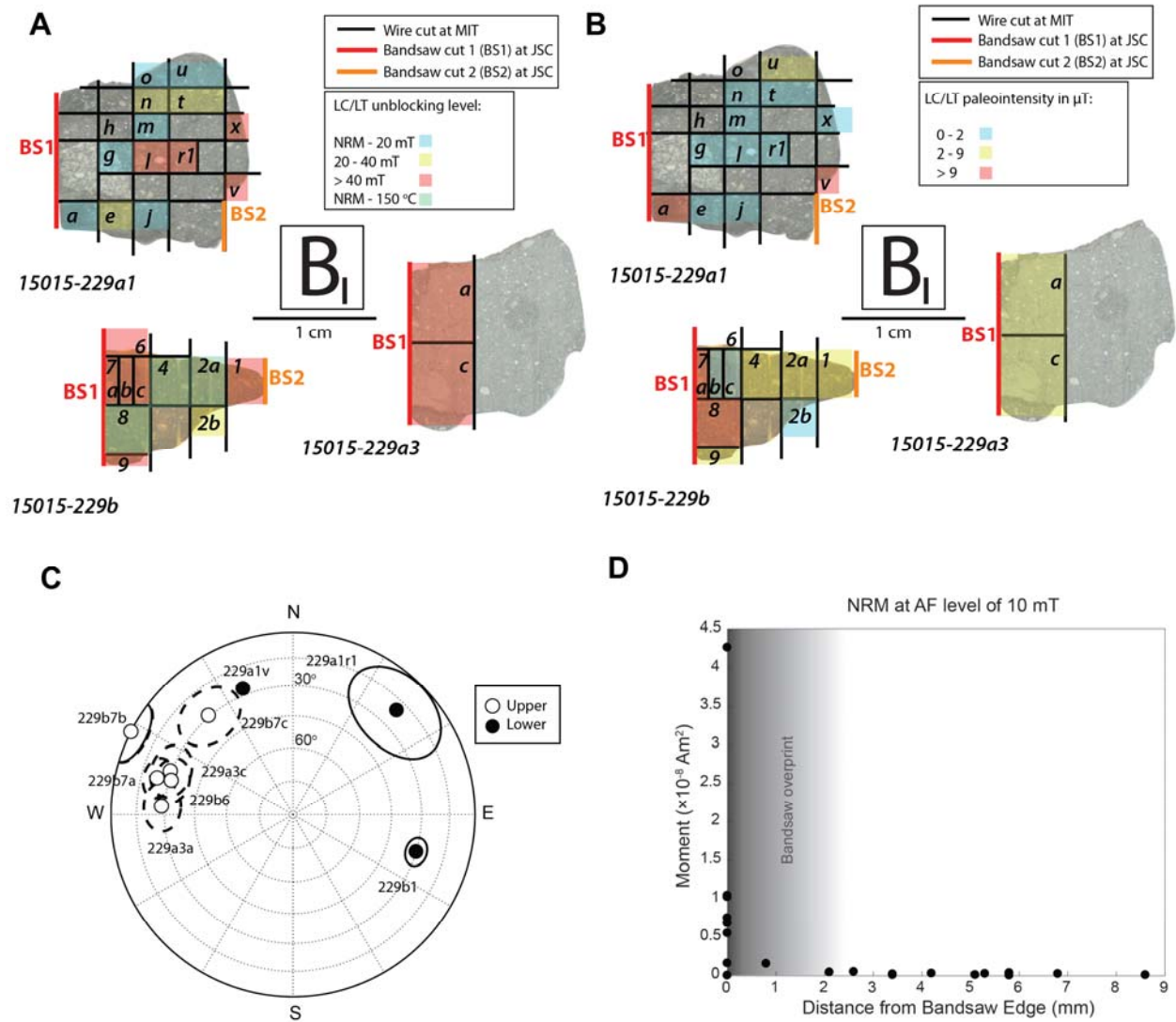


Fig. S15. Magnetic overprints in 15015 subsamples from bandsaw cutting at JSC. (A) Colored boxes superposed on photograph of parent samples denote peak unblocking alternating field (AF) or temperature steps for the low coercivity (LC) and low temperature (LT) components, respectively. (B) Colored boxes superposed on photograph of parent samples indicate LC/LT paleointensities based on anhysteretic remanent magnetization (ARM) and double-heating paleointensity experiments. Black lines in (A) and (B) denote wiresaw cuts at MIT, while red and orange lines denote two Johnson Space Center (JSC) bandsaw cut surfaces. Orientation cubes in (A) and (B) show the JSC orientation system, which is adopted in this study. (C) Equal area stereograph for the mean direction of bandsaw overprints in 15015 subsamples with distances ≤ 2.7 mm from the bandsawn edge. (D) NRM moment after AF demagnetization to 10 mT for all AF-demagnetized subsamples.

the most likely explanation for the LC/LT components is a pTRM acquired during heating from bandsawing at JSC. This bandsaw overprint is the likely source for the LC/LT components, especially for those subsamples located within 3 mm of the bandsaw edge.

For deeper subsamples, the LC/LT components' low peak unblocking temperatures and AF levels and scattered directions (fig. S12A) all indicate these components are also overprints. Given that the magnitudes of these components are comparable to those expected for terrestrial VRM (section 5), they were likely acquired during storage and maintenance at JSC (9). Another possibility is that they are due to modest physical contamination of the breccia or exposure to stray fields during handling by the astronauts or at JSC [e.g., ref. (34)].

As observed for 15465, after removal of the LC/LT components, the 15015 samples experienced no further decay in moment intensity and did not maintain stable directions during subsequent AF and thermal demagnetization (Figs. 1C and D, S13A and B, and S14A and B). PCA fits to the magnetization in these HC (~2-45 to 145 mT) and HT (150 °C to 780 °C) ranges produced scattered directions (fig. S12B) and large MAD values that were non-origin trending (i.e., DANG > MAD) for most subsamples (table S5) (72). Paleointensities in the HC/HT range had values indistinguishable from zero (section 4). pTRM checks showed that the samples did not experience significant thermochemical alteration up to laboratory heating temperatures of 680 °C (section 4). Therefore, the absence of stable NRM in the HT range indicates the lack of any total TRM. As with 15465, we conclude that no detectable paleofield was present during primary cooling of 15015 following formation of the matrix glass at the time the breccia was assembled.

A previous paleomagnetic analysis conducted on two subsamples from split 15015,18 and reported an ARM paleointensity of ~13 μ T (31). However, based on JSC photos, split 18, which was smaller than our split 12, was adjacent to and contained one face from the JSC bandsaw edge. Therefore, this high reported paleointensity is likely a bandsaw overprint. Another previous study (30) on breccia 15015 measured the NRM and IRM for a single chip of 15015 but did not draw any broad conclusions about 15015 paleointensity.

Section S4. Paleointensities

4.1. Non-thermal

4.1.1. Introduction. Our non-thermal paleointensity experiments normalize the NRM using either ARM or IRM (isothermal remanent magnetization). The ARM multicomponent paleointensity estimate is given by (42)

$$B_{\text{ARM}} = \frac{\Delta\text{NRM}}{\Delta\text{ARM}} \times \frac{B_{\text{DC}}}{f'} \quad (\text{S7})$$

where B_{ARM} is in units of μ T, ΔNRM is the NRM lost during progressive AF demagnetization, ΔARM is the progressive ARM gained in a bias field $B_{\text{DC}} = 50 \mu\text{T}$, and f' is the TRM/ARM ratio. Following many previous studies of lunar rocks, we adopt $f' = 1.34$ (6, 9, 42). The IRM multicomponent paleointensity estimate following the REM' method is given by (43)

$$B_{\text{IRM}} = \frac{\Delta\text{NRM}}{\Delta\text{IRM}} \times a \quad (\text{S8})$$

where B_{IRM} is in units of μT , ΔIRM is the IRM lost during progressive AF demagnetization (starting from an initial saturation IRM of 1.1 T) and a is a calibration constant with units of μT .

Like most previous studies of lunar rocks, we have adopted a nominal value of $a = 3000$ (6), which has been inferred from TRM/IRM global calibrations of data acquired on iron, magnetite, and pyrrhotite ferromagnetic minerals. However, it has been recently argued that mineral-specific values for a should be used, with $a = 10,000$ calculated for kamacite and martensite (73). Using the relations in ref. (73) and the saturation magnetization for schreibersite of $155.4 \text{ Am}^2 \text{ kg}^{-1}$, we calculate $a = 6,700$ for schreibersite. If we were to use these alternative values of $a = 6,700$ and $10,000$, this would increase our IRM paleointensities (tables S6-S8) by a factor of 2 and 3, respectively (although note that this would result in poorer agreement between our IRM and ARM LC paleointensities compared to our nominal $a = 3000$).

A variant on the ARM and IRM paleointensity techniques (74) uses a single value of NRM, IRM and ARM after the remanence has been cleaned of all overprints

$$B_{\text{ARM},c} = \frac{\text{NRM}_{\text{LC}}}{\text{ARM}_{\text{LC}}} \times \frac{B_{\text{DC}}}{f'} \quad (\text{S9})$$

$$B_{\text{IRM},c} = \frac{\text{NRM}_{\text{LC}}}{\text{IRM}_{\text{LC}}} \times a \quad (\text{S10})$$

where $B_{\text{ARM},c}$ and $B_{\text{IRM},c}$ again have units of μT , and NRM_{LC} , ARM_{LC} , and IRM_{LC} are the residual NRM, ARM, and IRM after AF demagnetization has removed LC overprints and isolated the primary HC magnetization range. This approach is known as the REMc method when used for IRM paleointensities. In this paper, we adopt the name AREMc when using it for ARM paleointensities. Although these methods only enable a paleointensity estimate of the highest-coercivity, primary magnetization range in a sample, they have the major advantage over the other two multicomponent approaches in minimizing the amount of AF-demagnetization which otherwise can contribute significant spurious ARM and GRM and thereby produce paleointensity estimates that are too high (25, 75).

There are two main contributions to the uncertainties of ARM and IRM paleointensity estimates. First, as highlighted above, the value of f' and a for a given sample systematically depend on its ferromagnetic mineralogy, grain size and shape distribution, such that actual paleointensities have been observed to vary around the value predicted by our adopted values for these coefficients with a 2-standard deviation systematic uncertainty of a factor of ~ 5 (6). This factor encompasses the uncertainties discussed by ref. (73) associated with the choice of a value for kamacite-bearing materials. Rare samples with metal grains with unusually strong shape anisotropy [ref. (76)] and/or those that carry a substantial fraction of pseudo-single domain grains that can enter vortex states during AF or IRM applications have been found to have f' and a that differ by an order of magnitude from our adopted values [refs. (75, 77)]. However, these properties differ from those of the dominantly equant, single domain to superparamagnetic grain sizes of most samples analyzed in this study (see section 6). A second source of non-systematic uncertainty is that associated with slope-fits inferred from the regression of ΔNRM versus ΔARM and ΔIRM . The latter is important because it enables tests of the hypothesis that the

paleointensity is distinguishable from zero. Note that we do not use cooling-rate corrections (78) because the laboratory heating time of 1-h for the ARM and IRM calibration experiment is close to the several-day cooling timescales of 15015 and 15465 (table S2), which would translate to only a ~10% correction (79).

Tables S6 and S7 and fig. S16 present the ARM and IRM paleointensities for 15465, while fig. S17 and tables S7 and S8 present those for 15015. All ARM and IRM paleointensities were indistinguishable within their 2-standard deviation systematic uncertainties. In the following sections, we describe the paleointensities for 15465 and 15015 subsamples in more detail and their implications. In the discussion below, we only quote uncertainties associated with the 95% confidence interval on the slope fits to assess whether a paleofield was distinguishably present. However, we note that the paleointensities are also subject to the factor of ~5 systematic uncertainty discussed above.

4.1.2. Breccia 15465.

4.1.2.1. Glass subsamples. We found that the LC paleointensities in the glass subsamples varied between ~4 to 70 μT (see table S6). The fact that the upper end of this range is similar to that of the Earth's field is consistent with our proposal that the LC component could be a terrestrial VRM. The wide range of paleointensities and non-unidirectionality for the LC components are consistent with the parent sample having tumbled multiple times during sample handling over the last four decades and its various constituent lithologies having different VRM acquisition and decay rates.

The ARM and IRM paleointensities for the HC range in all 5 glass subsamples are indistinguishable from zero and have 95% confidence intervals ranging from ~0.1 to 1 μT (table S6 and fig. S16). The weighted mean paleointensity for all glass samples is $-0.10 \pm 0.08 \mu\text{T}$ [range is 2 standard deviations (σ)]. The paleointensities obtained by the ARM method for both the LC and HC ranges are within error of those of the IRM method given the systematic uncertainties associated with knowledge of a and f' (table S6).

Because the paleointensities for the HC range in glass subsamples are essentially zero, the AREMc method provides an additional upper paleointensity limit estimate. The LC overprint in 15465 glass subsample 3-2 was removed by 8 mT (the spurious ARM noise level in table S7).

Table S6. Paleointensity estimates for 15465.

Subsample	Lithology	ARM (μT)		IRM (μT)		Thermal (μT)	
		LC	HC	LC	HC	LT	HT
3-2	Glass	30 ± 10	0.66 ± 1.04	32 ± 6	0.52 ± 0.24	-	-
4-1	Glass	21 ± 8	0.77 ± 0.99	11 ± 2	0.37 ± 0.34	-	-
4-2	Glass	21 ± 10	-0.24 ± 0.24	12 ± 0.9	-0.18 ± 0.19	-	-
5-1	Glass	-	-	-	-	11 ± 3	3.2 ± 3.1
5-3	Glass	-	-	-	-	27 ± 18	7.9 ± 8.2
6-1-2	Glass	37 ± 5	-0.58 ± 0.29	17 ± 2.0	-0.31 ± 0.15	-	-
6-2*	Clast	4.2 ± 0.2	0.22 ± 0.12	5.4 ± 0.2	0.39 ± 0.20	-	-
6-3	Clast	4.4 ± 0.2	-0.06 ± 0.15	5.4 ± 0.2	-0.13 ± 0.22	-	-
6-4-1	Glass	70 ± 12	0.52 ± 0.73	42 ± 1	0.06 ± 0.28	-	-
8-2*	Clast	-	-	-	-	11.8 (N/A)	6.5 ± 2.5
Weighted HC ARM and IRM paleointensity mean for glass samples (± 2 s.d.): $-0.10 \pm 0.08 \mu\text{T}$							
Weighted HT thermal paleointensity mean for glass samples (± 2 s.d.): $3.8 \pm 2.9 \mu\text{T}$							

Note: The first and second columns indicate the subsample names and their lithology. The third to eighth columns list the paleointensities in μT units for the low coercivity (LC), high coercivity (HC), low temperature (LT), and high temperature (HT) components listed in table S4. Uncertainties are 95% confidence intervals from Student's two-tailed *t*-test on slope fits to natural remanent magnetization (NRM) lost versus anhysteretic remanent magnetization (ARM) and isothermal remanent magnetization (IRM) gained. The uncertainties listed for non-thermal experiments in the fourth to seventh columns do not take into account the additional uncertainties associated with the poorly known ratio of ARM and IRM to thermoremanent magnetization (TRM) [which introduces an uncertainty factor of ~ 5 (6)].

*Subsamples that may contain a record of the lunar field prior to breccia assembly

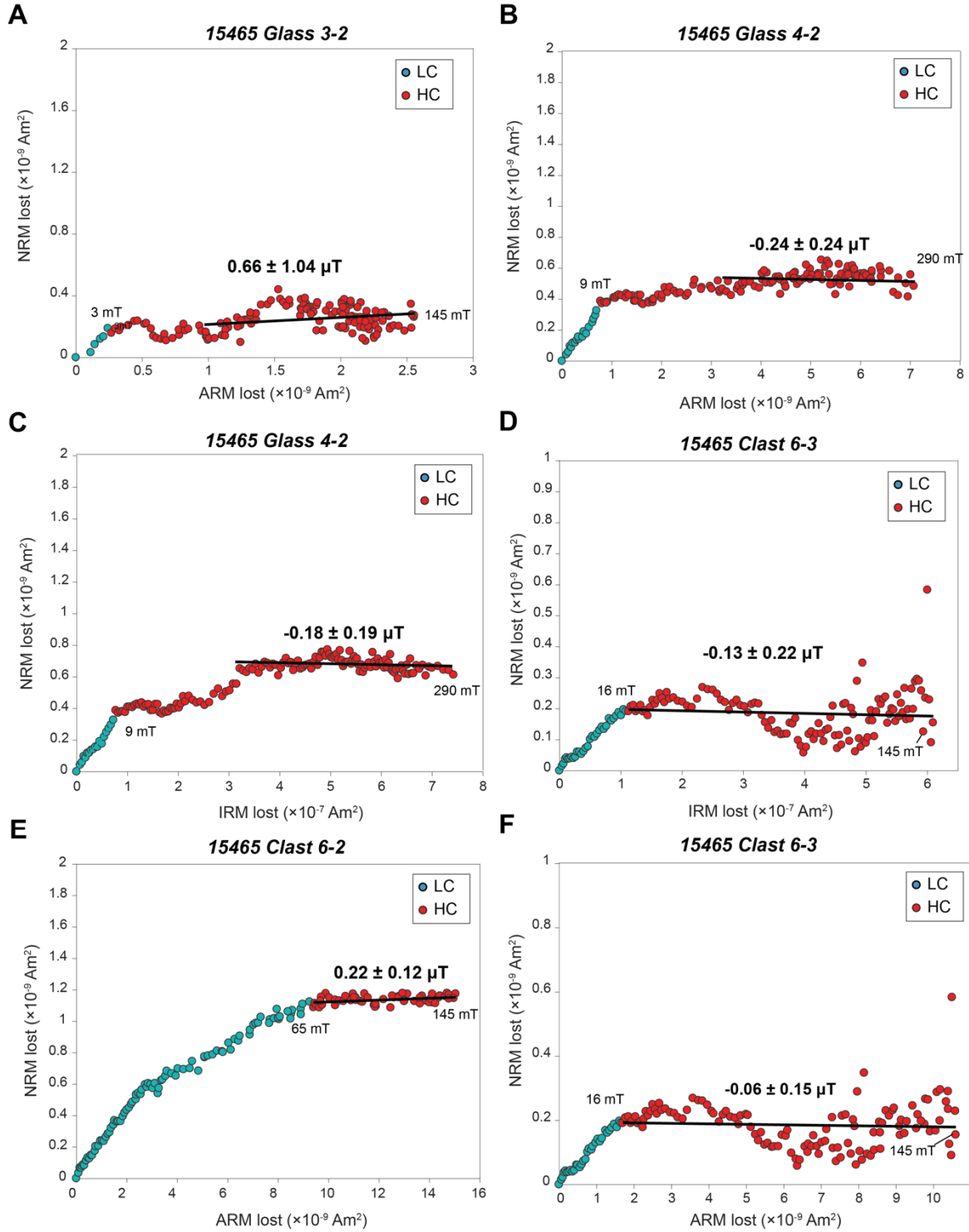


Fig. S16. Paleointensity estimates for breccia 15465 matrix glass and clast samples. (A-F) Anhysteretic remanent magnetization (ARM) and IRM paleointensities over the low coercivity (LC) (blue) and high coercivity (HC) (red) ranges, respectively for subsamples 3-2 (A), 4-2 (B, C), 6-3 (D, F) and 6-2 (E). The slopes in the HC range for the glass subsamples (A to C) is essentially zero. The HC range has a weak positive slope for clast subsample 6-2 (E), while it is essentially zero for clast subsample 6-3 (D, F).

Table S7. Paleointensity upper limits for 15465 and 15015 based on the AREMc method.

Subsample	AF noise level (mT)	Residual NRM/ARM	Paleointensity (μT)
15465 glass 3-2	8	0.11	<0.17
15465 clast 6-3	18	0.001	<0.06
15015 glass 229a1l	13	0.12	<0.08

Note: The first column lists the subsamples names and their lithology. The second and third columns list the alternating field (AF) noise level (see section 4) and the ratio of the residual natural remanent magnetization (NRM) to the residual anhysteretic remanent magnetization (ARM) at that AF level, respectively. The fourth column lists the paleointensity based on the residual ratio of NRM/ARM ratio using equation (S9) [section 4 and ref. (74)].

Given the NRM/ARM ratio at this AF level, an upper paleointensity limit of <0.17 μT is obtained for this glass subsample.

4.1.2.2. Clast subsamples. The LC components in the two clast subsamples had paleointensities of $\sim 4 \mu\text{T}$, within the range of LC components for glass subsamples. ARM paleointensity measurements for the HC range in clast subsamples 6-2 and 6-3 yield paleointensities of $0.22 \pm 0.12 \mu\text{T}$ and $-0.06 \pm 0.15 \mu\text{T}$, respectively (fig. S16E and F). The positive paleointensity for subsample 6-2 may indicate a weak remanence remaining from an earlier period when the dynamo was active (section 3.2.3), although this subsample did not exhibit a stable and origin-trending HC range (fig. S9C). Clast subsample 6-3 has a near-zero paleointensity, consistent with demagnetization of the exterior of the 20-mm diameter parent clast during breccia formation. The AREMc method for this subsample (table S7, Fig. 2) indicates an upper paleointensity limit of <0.06 μT (calculated at an AF level of 17.5 mT).

4.1.3. Breccia 15015. The LC paleointensities for the 15015 glass subsamples vary between 0.5 to 68 μT and depend strikingly on the location of the subsamples within the parent samples (fig. S15). Subsamples within 3.4 mm of the bandsawn surfaces have LC paleointensities between ~ 5 to 69 μT (fig. S17E and F), while at distance ≥ 3.4 mm have values of only ~ 0.5 to $\sim 3 \mu\text{T}$ (table S8). These results are consistent with our conclusion that the LC components in samples near the bandsawn surfaces are likely pTRMs due to heating from the bandsawing process (section 3). It is also possible that VRM acquisition in the Earth's field contributes to the LC components of some subsamples (section 5).

Glass subsamples ≥ 3.4 mm from bandsaw have HC paleointensities within error of zero (fig. S17A and B; table S8). The weighted mean paleointensity for all glass samples is $0.01 \pm 0.02 \mu\text{T}$. The glass and composite clast-glass lithologies have indistinguishable paleointensities and demagnetized in a similar manner. The upper paleointensity limit using the AREMc method for 15015 glass subsample 229a1l is <0.08 μT (calculated at an AF level of 13 mT) (Fig. 2 and table S7).

4.2. Thermal

4.2.1. Introduction. In addition to the non-thermal paleointensity experiments, we conducted controlled-atmosphere double-heating paleointensity experiments (26). The advantage of thermal paleointensities is that they do not rely on poorly-determined calibration constants (e.g., section 4.1.1) because they use direct TRM acquisition in a known laboratory field to normalize the NRM. The paleointensity is given by:

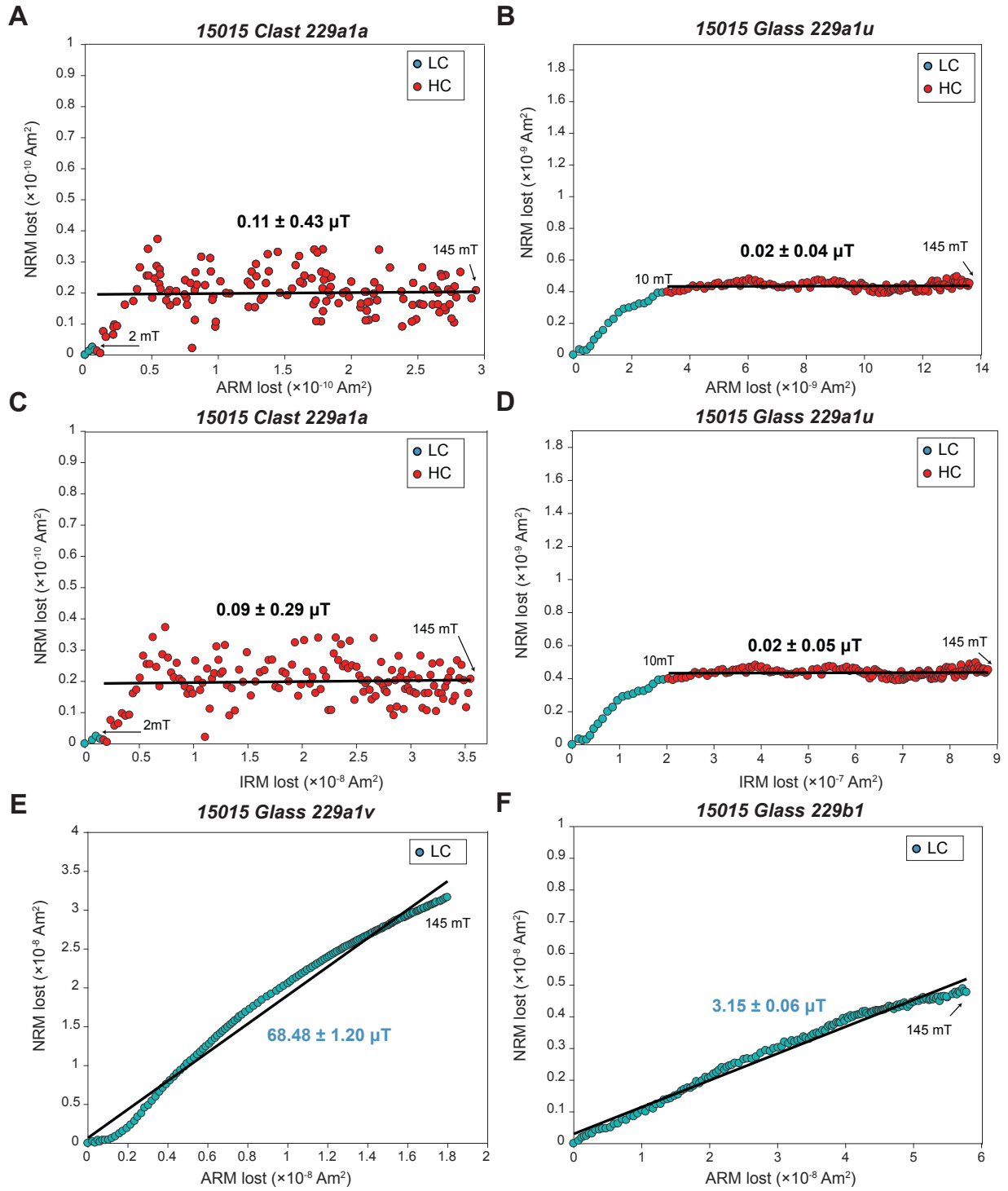


Fig. S17. Paleointensity estimates for breccia 15015 subsamples. (A-F) Anhyseretic remanent magnetization (ARM) and IRM paleointensities over the low coercivity (LC) (blue) and high coercivity (HC) (red) ranges, respectively for subsamples 229a1a (A, C), 229a1u (B, D) 229a1v (E), and 229b1 (F). The slope in the HC range for the glass subsamples (A to D) is essentially zero. The subsamples in (E) and (F) contain strong LC overprint with a variable apparent paleointensities between ~ 3 to $68 \mu\text{T}$ due to JSC bandsaw cutting (see section 3).

Table S8. Paleointensity estimates for 15015.

Subsample	Lithology	JSC Sawcut Distance (mm)	ARM (μT)		IRM (μT)		Thermal (μT)	
			LC	HC	LC	HC	LT	HT
229a1a	Clast	0	9.6 \pm 14	0.11 \pm 0.43	4.0 \pm 6.3	0.09 \pm 0.29	-	-
229a1e	Glass	3.4	0.55 \pm 0.07	-0.02 \pm 0.06	0.70 \pm 0.09	-0.01 \pm 0.07	-	-
229a1g	Clast-Glass	3.4	0.74 \pm 0.06	0.02 \pm 0.04	0.87 \pm 0.06	0.02 \pm 0.05	-	-
229a1j	Glass	4.2	0.67 \pm 0.05	0.01 \pm 0.05	0.81 \pm 0.06	0.02 \pm 0.06	-	-
229a1l	Glass	5.8	0.54 \pm 0.06	0.04 \pm 0.10	-	-	-	-
229a1m	Glass	5.8	1.47 \pm 0.20	-0.02 \pm 0.05	1.5 \pm 0.2	-0.02 \pm 0.06	-	-
229a1n	Glass	5.8	0.71 \pm 0.05	0.21 \pm 0.22	0.71 \pm 0.05	0.24 \pm 0.25	-	-
229a1r1	Glass	2.6	0.36 \pm 0.02	-	-	-	-	-
229a1t	Glass	6.8	1.2 \pm 0.10	0.13 \pm 0.16	1.2 \pm 0.1	0.16 \pm 0.18	-	-
229a1u	Glass	8.6	5.1 \pm 0.40	0.02 \pm 0.04	6.6 \pm 0.6	0.02 \pm 0.05	-	-
229a1v	Glass	0	68 \pm 1	-	-	-	-	-
229a1x	Glass	5.1	1.1 \pm 0.1	0.05 \pm 0.08	1.0 \pm 0.1	0.06 \pm 0.08	-	-
229a3a	Glass	0	3.4 \pm 0.2	-	-	-	-	-
229a3c	Clast-Glass	0	2.6 \pm 0.1	-	-	-	-	-
229b1	Glass	0	3.2 \pm 0.1	-	3.4 \pm 0.1	-	-	-
229b2a	Glass	5.3	-	-	-	-	-	0.35 \pm 0.46
229b2b	Glass	5.3	0.84 \pm 0.06	0.19 \pm 0.20	-	-	-	-
229b4	Glass	2.6	-	-	-	-	-	0.42 \pm 0.34
229b7a	Glass	0	13 \pm 0.6	-	14 \pm 0.6	-	-	-
229b7b	Glass	0.8	1.4 \pm 0.04	-	-	-	-	-
229b7c	Glass	2.1	0.69 \pm 0.03	-	0.72 \pm 0.04	-	-	-
229b8	Glass	0	-	-	-	-	-	0.24 \pm 0.24
229b9	Glass	0	4.4 \pm 0.2	-	4.6 \pm 0.2	-	-	-

Weighted HC ARM and IRM paleointensity mean for glass samples (± 2 s.d.): -0.01 \pm 0.02

Weighted HT thermal paleointensity mean for glass samples (± 2 s.d.): 0.31 \pm 0.18 μT

Note: The first and second columns indicate the subsample names and their lithology. The third column lists the distance of the subsample edge from the closest JSC saw cut face. The fourth to ninth columns list the paleointensities in μT for the low coercivity (LC), high coercivity (HC), low temperature (LT), and high temperature (HT) components listed in table S5. Uncertainties are 95% confidence intervals on slope fits to natural remanent magnetization (NRM) lost versus anhysteretic remanent magnetization (ARM) and isothermal remanent magnetization (IRM) gained from Student's two-tailed t -test. The uncertainties listed for non-thermal experiments in the fourth to seventh columns do not take into account the additional uncertainties associated with the poorly known ratio of ARM and IRM to thermoremanent magnetization (TRM) [which introduces an uncertainty factor of ~ 5 (6)].

$$B_{\text{TRM}} = \frac{\Delta\text{NRM}}{p\text{TRM}} \times B_{\text{lab}} \quad (\text{S11})$$

where ΔNRM is the NRM lost during zero-field heating, $p\text{TRM}$ is the $p\text{TRM}$ -grained during in-field heating, and B_{lab} is the laboratory field. Again, we do not use cooling-rate corrections (78) because the laboratory heating time of 1-h for our paleointensity experiment is close to the several-day cooling timescales of 15015 and 15465 (table S2).

We followed the in-field, zero-field, zero-field, in-field (IZZFI) scheme (44), setting B_{lab} to 10 μT and 3 μT for the experiments on 15465 and 15015, respectively. We used temperature steps in increments of 50 $^{\circ}\text{C}$ between 100 to 300 $^{\circ}\text{C}$, of 30 $^{\circ}\text{C}$ between 300 to 480 $^{\circ}\text{C}$, and of 50 $^{\circ}\text{C}$ from 480 to 780 $^{\circ}\text{C}$. We also checked for thermochemical alteration by repeating the in-field steps every few consecutive steps (i.e., $p\text{TRM}$ checks). For breccia 15465, $p\text{TRM}$ checks were conducted after heating to 250 $^{\circ}\text{C}$ (back to 150 $^{\circ}\text{C}$), to 330 $^{\circ}\text{C}$ (back to 250 $^{\circ}\text{C}$), to 390 $^{\circ}\text{C}$ (back to 330 $^{\circ}\text{C}$), to 450 $^{\circ}\text{C}$ (back to 390 $^{\circ}\text{C}$), to 530 $^{\circ}\text{C}$ (back to 450 $^{\circ}\text{C}$), to 630 $^{\circ}\text{C}$ (back to 530 $^{\circ}\text{C}$), and to 730 $^{\circ}\text{C}$ (back to 630 $^{\circ}\text{C}$). For breccia 15015, $p\text{TRM}$ checks were conducted after heating to 360 $^{\circ}\text{C}$ (back to 300 $^{\circ}\text{C}$), to 420 $^{\circ}\text{C}$ (back to 360 $^{\circ}\text{C}$), to 480 $^{\circ}\text{C}$ (back to 420 $^{\circ}\text{C}$), to 580 $^{\circ}\text{C}$ (back to 480 $^{\circ}\text{C}$), and to 680 $^{\circ}\text{C}$ (back to 580 $^{\circ}\text{C}$). We conducted these experiments up to the Curie temperature of kamacite (780 $^{\circ}\text{C}$).

Uncertainties on the paleointensity values are those associated with slope-fits inferred from the regression of ΔNRM versus $p\text{TRM}$. Tables S6 and S8 summarize our measured paleointensity values for breccias 15465 and 15015, respectively. Tables S9 and S10 provide statistical measures of the thermal experiments and the $p\text{TRM}$ check statistics, respectively (80).

The paleointensity statistical parameters are defined in the footnote in table S9. The parameter *FRAC* indicates the relative fraction of NRM demagnetization over a desired temperature range compared with the entire temperature range of NRM demagnetization. It evaluates the fraction of the initial NRM used during fits for a certain temperature range. The parameter β quantifies the scatter of the paleointensity around the best-fit line in plots of NRM lost versus $p\text{TRM}$ gained. The parameter *GAP-MAX* indicates the maximum fraction of NRM demagnetization between two consecutive temperature steps over the experiment. The parameter q evaluates the paleointensity fit quality (80). The parameter *DRATS* evaluates the amount of thermochemical alteration by normalizing the sum of the differences between the $p\text{TRM}$ checks and $p\text{TRMs}$ previously gained at the same temperature by the $p\text{TRM}$ gained at the maximum temperature step. *DRATS* values below 20-25% indicate the thermochemical stability of the magnetic carriers for the desired temperature range (72). The normalized *pTRM check parameter* is the percentage difference between a given $p\text{TRM}$ and the $p\text{TRM}$ previously gained at the same temperature normalized by the latter $p\text{TRM}$. Although the $p\text{TRM}$ check parameter is useful for diagnosing whether a single step should be included in a paleointensity fit, it can yield

Table S9. Statistics for thermal paleointensity experiments for breccias 15465 and 15015.
A. Breccia 15465.

Subsample	Range	Temperature	<i>N</i>	<i>FRAC</i>	β	<i>GAP-MAX</i>	<i>TGAP-MAX</i>	<i>DRATS</i> (%)	q	<i>P</i> (μT)
Glass 5-1	LT	NRM-390 °C	7	0.79	0.11	0.23	NA	5.2	3.9	11.43 \pm 3.33
	HT	390-730 °C	9	NA	0.41	NA	0.29	38.0 ¹	NA	3.20 \pm 3.14
Glass 5-3	LT	NRM-330 °C	5	0.84	0.21	0.31	NA	5.8	1.5	27.03 \pm 18.40
	HT	450-730 °C	7	NA	0.40	NA	0.27	17.3	NA	7.93 \pm 8.15
Clast 8-2	LT	NRM-200 °C	2	0.40	NA	0.57	NA	2.1	NA	11.82
	HT	200-730 °C	14	0.46	0.18	0.35	0.26	4.8	4.5	6.51 \pm 2.53

B. Breccia 15015.

Subsample	Range	Temperature range	<i>N</i>	<i>FRAC</i>	β	<i>GAP-MAX</i>	<i>TGAP-MAX</i>	<i>DRATS</i> (%)	q	<i>P</i> (μT)
Glass 229b2a	HT	300-730 °C	12	NA	0.60	NA	0.19	23.3	NA	0.35 \pm 0.46
Glass 229b4	HT	300-730 °C	12	NA	0.36	NA	0.22	17.2	NA	0.42 \pm 0.34
Glass 229b8	HT	300-730 °C	12	NA	0.44	NA	0.23	11.0	NA	0.24 \pm 0.24

Notes: The first column lists the subsample name. The second and third columns list the temperature ranges. The fourth column lists the number of data points used for the fits. The fifth to tenth columns list thermal paleointensity quality statistics: *FRAC*, β , *GAP-MAX*, *TGAP-MAX*, *DRATS*, and q . As described in section 4.2.1, the parameters *FRAC*, q , and *GAP-MAX* are not reported for the glass HT range since these parameters are not meaningful for zero-field paleointensities.

All parameters except *TGAP-MAX* are described in ref. (80)

$$FRAC = \frac{\sum_{i=start}^{end-1} |NRM_{i+1} - NRM_i|}{|NRM_{n_{max}}| + \sum_{i=1}^{n_{max}-1} |NRM_{i+1} - NRM_i|}$$

$\beta = \sigma_b/|b|$ where σ_b and $|b|$ are the standard error and the absolute value for the fit slope, respectively

$$DRATS = \frac{|\sum_{i=1}^N \delta pTRM_{ij}|}{pTRM_{end}} \times 100$$

$q = fg/\beta$ where f and g are the NRM fraction used for fitting and the gap factor, respectively.

TGAP-MAX is explained in section 4.2.1.

P is the paleointensity in units of μT and associated 95% formal confidence interval from Student's t-test.

¹If the 530 back to 450 °C $p\text{TRM}$ check step [which has an anomalously high $p\text{TRM}$ check parameter (see table S10)] is omitted, the *DRATS* for this subsample for the HT range after would drop to 20.1.

Table S10. pTRM check parameters for double-heating experiments.

Prior pTRM temperature (°C)	pTRM check temperature (°C)	15465 (%)			15015 (%)		
		5-1	5-3	8-2	b2a	b4	b8
250	150	27.4	39.0	74.8			
330	250	5.0	2.5	21.6			
390	330	12.9	27.3	38.6			
450	390	11.3	16.7	5.4			
530	450	56.7	8.0	26.6			
630	530	3.1	1.9	21.5			
730	630	20.4	12.7	13.0			
360	300				9.3	9.2	6.0
420	360				0.8	2.9	1.4
480	420				14.5	0.7	5.1
580	480				6.4	18.2	0.1
680	580				9.9	1.9	7.2

Note: The first column lists the partial thermoremanent magnetization (pTRM) temperature steps preceding the pTRM check steps. The second column lists the pTRM check temperature steps. The numbers in the third to eighth columns are the percentage differences between pTRM and pTRM checks: $(|pTRM_{check} - pTRM|/pTRM) \times 100$

meaninglessly high values at low temperature steps where little alteration is occurring due to the small amount of pTRM gained at those temperatures. As such, we favor *DRATS* as a more accurate indication of the thermochemical stability since it is not penalized by the small low-temperature pTRM values.

As discussed in section 3, the NRM for the HT range does not decline in intensity but rather experiences non-systematic changes in direction and intensity due to the lack of primary NRM. As a result, *FRAC*, *q*, and *GAP-MAX*, which incorporate NRM vector addition and subtraction, do not provide meaningful measures of a zero-field paleointensity estimate. We, therefore, define an alternative gap parameter for HT range

$$TGAP - MAX = \frac{\max\{|pTRM_{i+1} - pTRM_i|\}_{i=1:N-1}}{\sum_{i=1}^N |pTRM_{i+1} - pTRM_i|} \quad (S12)$$

where *N* is the number of steps in the temperature range of interest for the paleointensity calculation. *TGAP-MAX* evaluates whether the in-field steps have been uniformly spaced to provide a representation of the pTRM gained over the temperature range of interest.

4.2.2. Breccia 15465. We conducted thermal paleointensity experiments on three mutually oriented subsamples of 15465 (2 glass subsamples and 1 subsample of the large clast). Based on the pTRM checks on the three subsamples (table S10 and triangles in fig. S18), there is no evidence for significant thermochemical alteration up to 730 °C, with *DRATS* < 25% over this range (except for the HT range in subsample 5-1). The LT components for glass subsamples 5-1 and 5-3 yielded paleointensities of 11.4 ± 3.3 and 27.0 ± 18.4 μT, respectively. The *FRAC* parameter for glass subsamples 5-1 and 5-3 was ~80%, indicating most of the NRM has been removed by the end of LT range. The *β* value of ~0.1-0.2 and *q* value larger than ~1 (80) suggest the presence of magnetization in the LT range, consistent with the discussion in section 3. The similarity of the LT paleointensity to that of the Earth's field is more evidence the LT component being a VRM acquired in Earth's magnetic field.

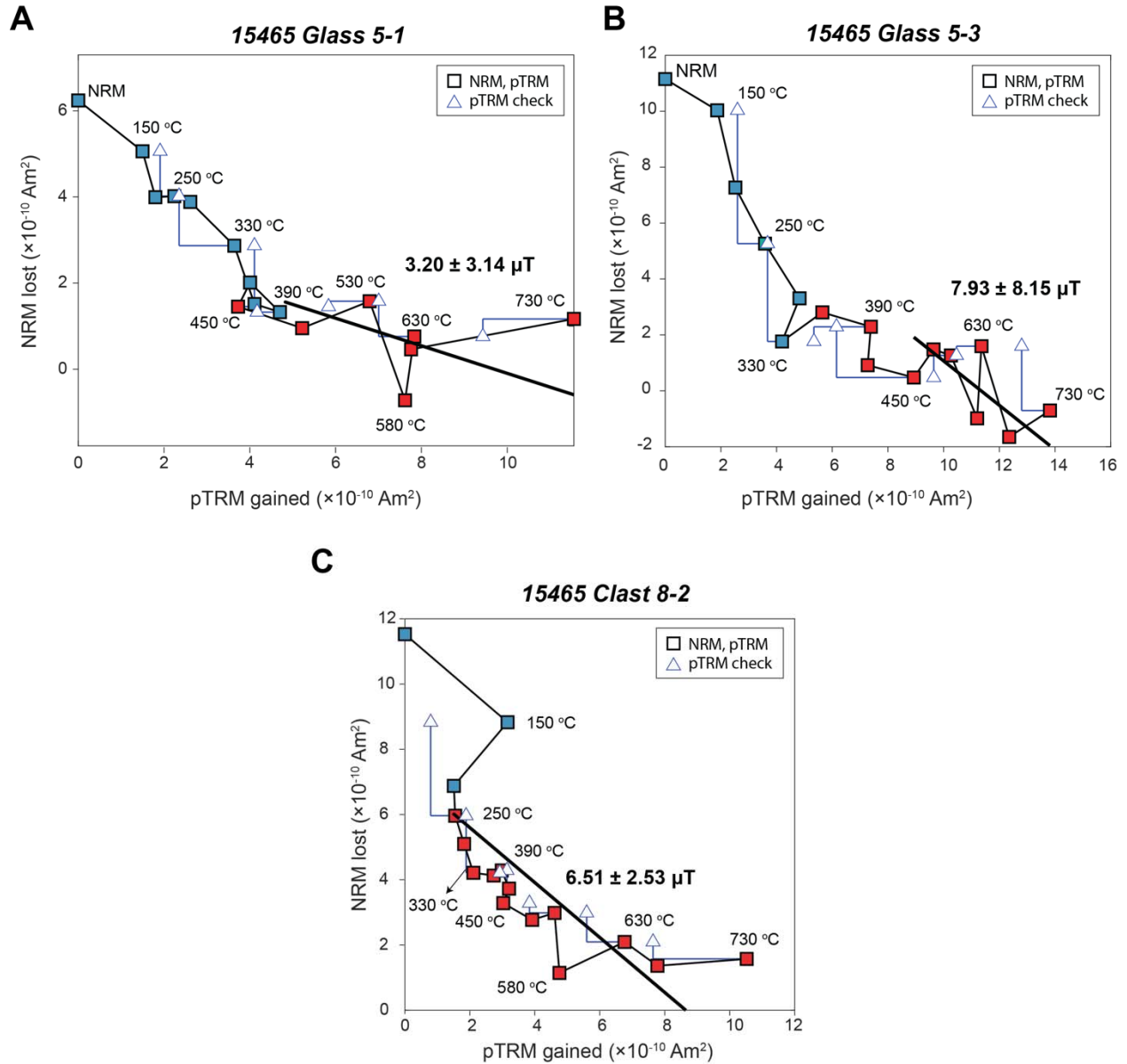


Fig. S18. Thermal paleointensity experiments for breccia 15465 subsamples. Shown is the natural remanent magnetization (NRM) lost as a function of the partial thermal remanent magnetization (pTRM) gained during thermal steps up to 730 °C. NRM lost and pTRM gained steps are denoted with squares, with blue and red symbols denoting data in the low temperature (LT) and high temperature (HT) ranges, respectively. pTRM checks for alteration are denoted with triangles. (A) Glass subsample 5-1. (B) Glass subsample 5-3. (C) Clast subsample 8-2. The LT ranges in the glass subsamples (A and B) unblock between 330-390 °C. The HT range for the glass subsamples (A and B) results in an essentially zero paleointensity. The HT range in the clast subsample (C) has a positive slope associated with an origin-trending component (see fig. S10).

The *GAP-MAX* value of ~ 0.3 suggests that temperature steps are appropriately spaced and acceptably represent the entire temperature range.

The HT ranges for the glass subsamples yield paleointensities of $3.20 \pm 3.14 \mu\text{T}$ and $7.93 \pm 8.15 \mu\text{T}$ and therefore indicate paleointensities indistinguishable from zero. The large β value of ~ 0.4 [compare with values for lunar samples formed in a dynamo field (9) and with the threshold value of 0.15 in ref. (80)] confirms the absence of paleofield recorded in the HT range. The *TGAP-MAX* value of ~ 0.25 suggests that the temperature steps are sufficiently uniformly-spaced.

By comparison, the origin-trending HTC component in clast subsample 8-2 (fig. S10B) has a weak but non-zero paleointensity of $6.51 \pm 2.53 \mu\text{T}$. The q parameter for clast subsample 8-2 is 4.5, which exceeds the typical acceptability threshold of $>\sim 1$ (80) and is within the range of paleointensities obtained for the epoch of the lunar dynamo such as those from breccia 15498 [~ 2 to 6; (9)]. The β value in this clast subsample is ~ 0.2 , which is smaller than the HT range for other 15465 glass subsamples and is close to the typical acceptability threshold range of 0.15 (80). Therefore, clast subsample 8-2 contains a non-zero paleointensity.

4.2.3. Breccia 15015. We conducted thermal paleointensity experiments on three glass subsamples of breccia 15015 (Figs. 3 and S19). Note that the pTRM steps in double-heating experiments for breccia 15015 start from 300 °C, while the zero-field steps have LT and HT ranges of NRM-150 °C, and 150-780 °C, respectively (section 3). Hence, we do not report the LT paleointensities and only report HT paleointensities starting from 300 °C. The HT range yielded paleointensity values of 0.35 ± 0.46 , 0.42 ± 0.34 , and $0.24 \pm 0.24 \mu\text{T}$ for these subsamples. These HT paleointensities are indistinguishable from zero. The *DRATS* parameters are below 25%, confirming no significant thermochemical alteration up to 680 °C (table S10 and triangles in fig. S19). The *TGAP-MAX* parameter of ~ 0.25 suggests the temperature steps are sufficiently uniformly-spaced. The large β value of ~ 0.4 - 0.6 confirms the absence of paleofield recorded in the HT range.

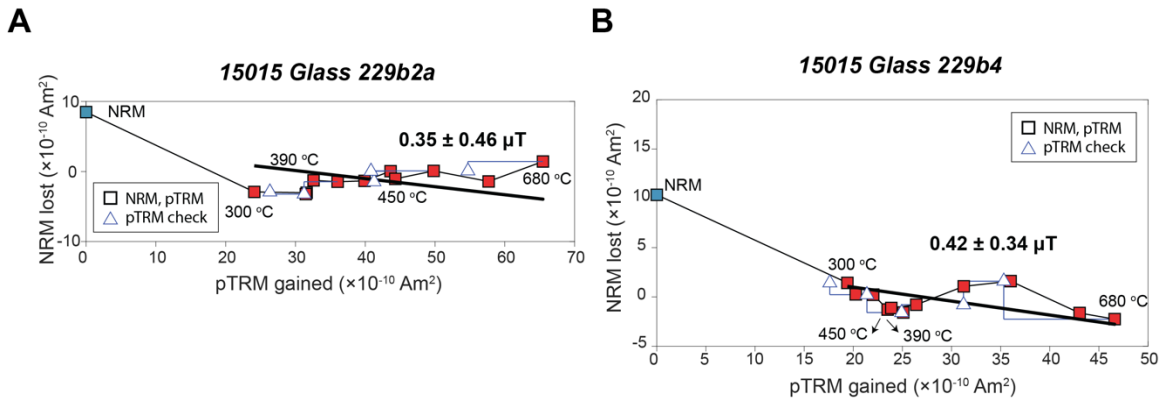


Fig. S19. Thermal paleointensity experiments for breccia 15015 glass subsamples. Shown is the natural remanent magnetization (NRM) lost as a function of the partial thermal remanent magnetization (pTRM) gained during thermal steps up to 680 °C. NRM lost and pTRM gained steps are denoted with squares, with blue and red symbols denoting data in the low temperature (LT) and high temperature (HT) ranges, respectively. pTRM checks for alteration are denoted with triangles. The LT range unblocks by 150 °C. The HT range for the glass subsamples has an essentially zero paleointensity. (A) Subsample 229b2a. (B) Subsample 229b4.

4.3. Paleointensity fidelity tests

4.3.1. Introduction. A complementary approach to estimating an upper limit on the paleofield is to conduct repeat paleointensity experiments on artificial laboratory NRMs acquired in a range of TRM-equivalent ambient fields, with the goal of determining the minimum paleofield strength that can be recovered using our paleointensity method. In particular, following ref. (25), we applied ARMs to glass subsamples 15465-3-2 and 15015-229a11, as well as clast subsample 15465-6-3, with a peak AF of 260 mT and using DC bias fields ranging from 0.5-50 μT . This bias field range corresponds to TRM-equivalent-fields of 0.4-37 μT given our adopted TRM/ARM value of 1.34. By comparing the retrieved paleointensity from the known paleointensity, we can assess the sample's magnetic recording fidelity. For these experiments, the induced ARMs were compared against the induced DC bias field of 50 μT .

The fidelity of the recorded field was assessed using the following quality parameters

$$D = \frac{|L - I|}{L} \quad (\text{S13a})$$

$$E = \frac{W}{L} \quad (\text{S13b})$$

where D and E are the absolute difference and error of estimation and L , I , and W are the applied field strength, retrieved field, and the 95% confidence interval on the retrieved paleointensity. According to ref. (25), the acceptance condition is met once both D and E are below 100%. In a recent study, ref. (81) argued that the D' provides a more robust estimate than D

$$D' = \frac{I - L}{L} \quad (\text{S14})$$

where the acceptance condition is met when $-50 < D' < 100\%$. We report here all three values above. Equations (S13) and (S14) show that E represents the 95% confidence interval of the slope, while D and D' quantify the inaccuracy of the paleointensity magnitude.

4.3.2. Breccia 15465. For glass subsample 3-2 (fig. S20 and table S11A), we found that we can accurately recover paleointensities as weak as 1.5 μT . Its value of E stays marginally stable down to ~ 0.5 μT , while the D and D' criteria failed at around 1.5 μT . This implies that spurious ARM acquisition associated with the application of the laboratory ARM that is serving as a proxy for the NRM is a major noise source at low DC fields. Hence, it is likely that the sample could have recorded even weaker fields than suggested by these experiments, such that this fidelity method likely provides an overestimate of the minimum paleointensity retrievable using our non-thermal paleointensity method. Nevertheless, this ~ 1.5 μT weakest recoverable field is still much lower than most lunar basalts which have been found to have minimum recoverable fields of ~ 7 to 10 μT when using nonthermal paleointensity methods (25). This value is also below the paleointensity of all previous lunar samples shown to record an active dynamo (Fig. 4). For clast subsample 6-3, we found that we can recover paleointensities as low as 0.4 μT (fig. S20 and table S11A). Compared with the glass subsample, it can be observed even more clearly for this subsample how D and D' fail before E exceeded its acceptability threshold.

Table S11. Paleointensity fidelity tests for breccias 15465 and 15015.**A. Breccia 15465**

15465 Glass 3-2							
ARM DC field (μT)	TRM-equivalent (μT)	Retrieved (μT)	D (%)	E (%)	D' (%)	Accepted ^a	Accepted ^b
50	37.3	37.3	0	0	0	✓	✓
20	14.9	12.2	18	4	-18	✓	✓
10	7.4	7.1	4	7	-4	✓	✓
5	3.7	3.4	8	15	-8	✓	✓
2	1.5	2.9	93	37	93	✓	✓
1	0.7	1.6	129	45	129	x	x
0.5	0.4	0.9	125	106	125	x	x

15465 Clast 6-3							
ARM DC field (μT)	TRM-equivalent (μT)	Retrieved (μT)	D (%)	E (%)	D' (%)	Accepted ^a	Accepted ^b
50	37.3	37.3	0	0	0	✓	✓
20	14.9	15.0	1	1	1	✓	✓
10	7.4	7.5	1	1	1	✓	✓
5	3.7	3.3	11	2	-11	✓	✓
2	1.5	1.2	20	4	-20	✓	✓
1	0.7	0.5	29	8	-29	✓	✓
0.5	0.4	0.1	75	11	-75	✓	x

B. Breccia 15015

15015 Glass 229a11							
ARM DC field (μT)	TRM-equivalent (μT)	Retrieved (μT)	D (%)	E (%)	D' (%)	Accepted ^a	Accepted ^b
50	37.3	37.3	0	0	0	✓	✓
10	7.4	7.3	1	0	-1	✓	✓
5	3.7	3.8	3	1	3	✓	✓
2	1.5	1.4	7	4	-7	✓	✓
1	0.7	0.8	14	6	14	✓	✓
0.5	0.4	0.8	100	16	100	x	x

Notes: The first column lists the DC bias field used during the anhysteretic remanent magnetization (ARM) acquisition to represent thermoremanent magnetization (TRM) (not that all experiments use a 260 mT AF). The second column lists the TRM-equivalent field assuming ARM/TRM ~ 1.34 (49). The third column lists the retrieved paleointensity. The fourth and fifth columns list the difference (D) and error of estimation (E) for the retrieved paleointensity, I , from the applied ARM field strengths, L , as defined by ref. (25): $D = |L-I|/L \times 100$ and $E = W/L \times 100$ (where W is the 95% confidence interval for the estimate of I). The sixth column is the difference metric as redefined by ref. (81): $D' = (I-L)/L \times 100$. See figs. S20 and S21 for plots associated with these experiments.

^aThe acceptance criterion in the seventh column is positive when both D and E are less than 100% [see ref. (25)].

^bThe acceptance criterion in the eighth column is positive when both $-50\% < D' < 100\%$ and $E < 50\%$ [see ref. (81)].

4.3.3. Breccia 15015. We found that we can recover paleointensities from glass subsample 229a11 as weak as 0.8 μT (fig. S21 and table S11B), for which criteria for D , D' , and E all simultaneously pass. Again, these fidelity tests are limited by spurious noise associated with the weak-DC field ARM, such that it is likely that this sample can record even weaker fields than 0.7 μT .

4.4. Synthesis of paleointensity limits on HC/HT range. We have obtained near-zero paleointensities for the HC/HT range for the glass and demagnetized clast subsamples for breccia 15465 and for glass and clast-glass subsamples for breccia 15015. In table S12, we summarize all the paleointensities using the ARM, IRM, AREMc, and thermal experiments.

For breccia 15465 glass subsamples, the nominal ARM paleointensities are $<0.77 \mu\text{T}$ and the IRM paleointensities are $<0.52 \mu\text{T}$. The demagnetized clast subsample yielded slightly negative ARM and IRM paleointensities; such unphysical negative paleointensities are likely due to measurement noise. The thermal experiments placed less restrictive upper limits of $<3.2 \mu\text{T}$ and

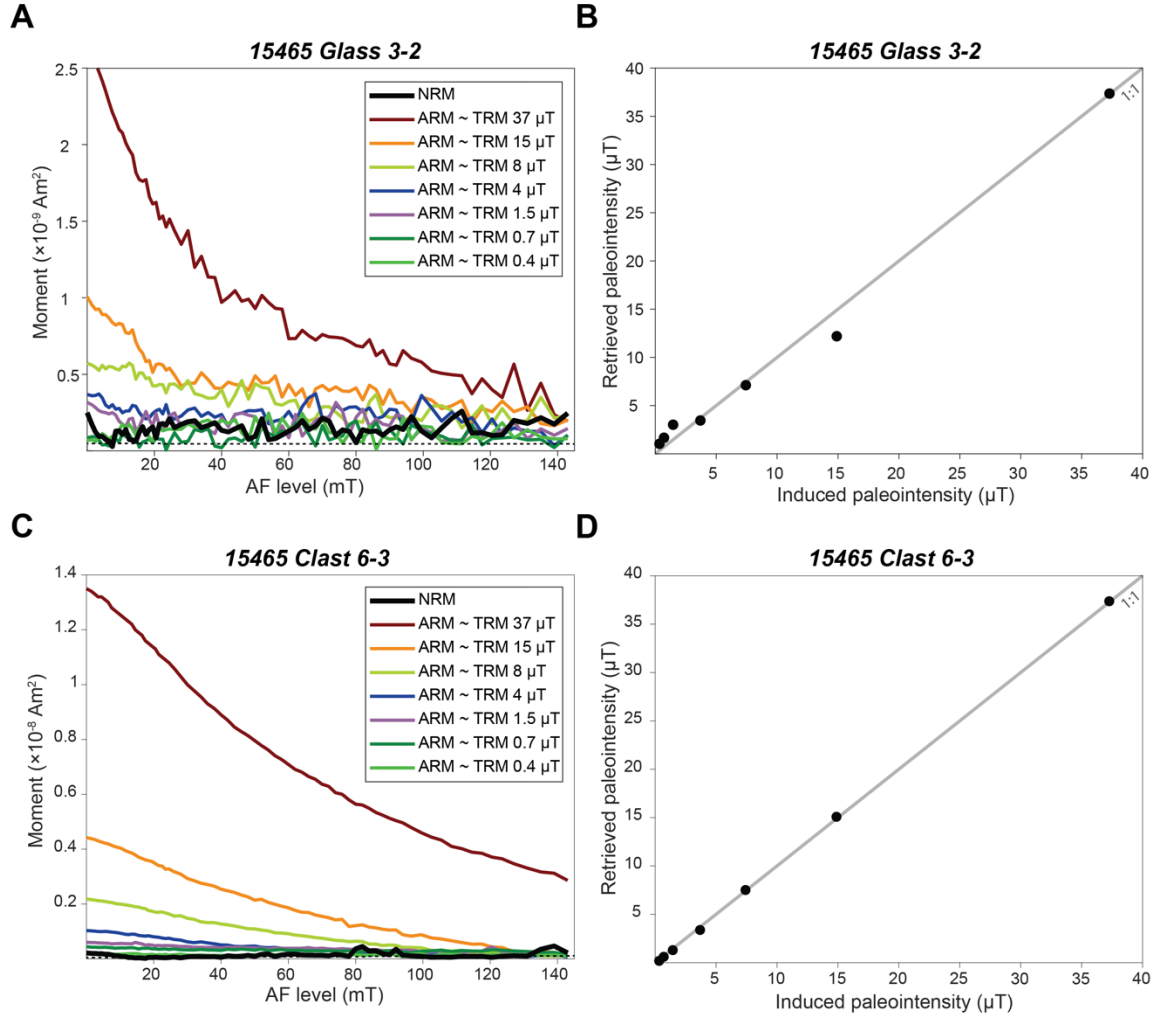


Fig. S20. Paleointensity fidelity tests for breccia 15465. (A, C) Alternating field (AF) demagnetization of natural remanent magnetization (NRM) compared to that of anhysteretic remanent magnetization (ARM) acquired in various DC bias fields for glass subsample 3-2 (A) and clast subsample 6-3 (C). Legends list thermoremanent magnetization (TRM)-equivalent fields for ARMs acquired in a range of DC bias fields in an AF of 260 mT and assuming ARM/TRM = 1.34 (49) (see supplementary text section 4). Horizontal dashed lines indicate noise level due to acquisition of spurious ARM due to imperfections in the AF waveform. (B, D) Recovered paleointensity versus induced paleointensity for different DC fields for glass subsample 3-2 (B) and clast subsample 6-3 (D). Gray lines show the 1:1 line. See table S11A for paleointensity fidelity metrics associated with these experiments.

<7.9 μT on the glass subsamples. The latter experiments confirm the absence of NRM in the HT range, but zigzagging scatter in the Arai plots (figs. S18A and B) results in a large 95% confidence interval. The AREMc method yielded upper paleointensity limits of <0.17 μT and <0.06 μT for glass and demagnetized clast subsamples, respectively. The fidelity tests indicated that our method can recover fields as weak as 1.5 μT and 0.4 μT for glass and clast subsamples, respectively;

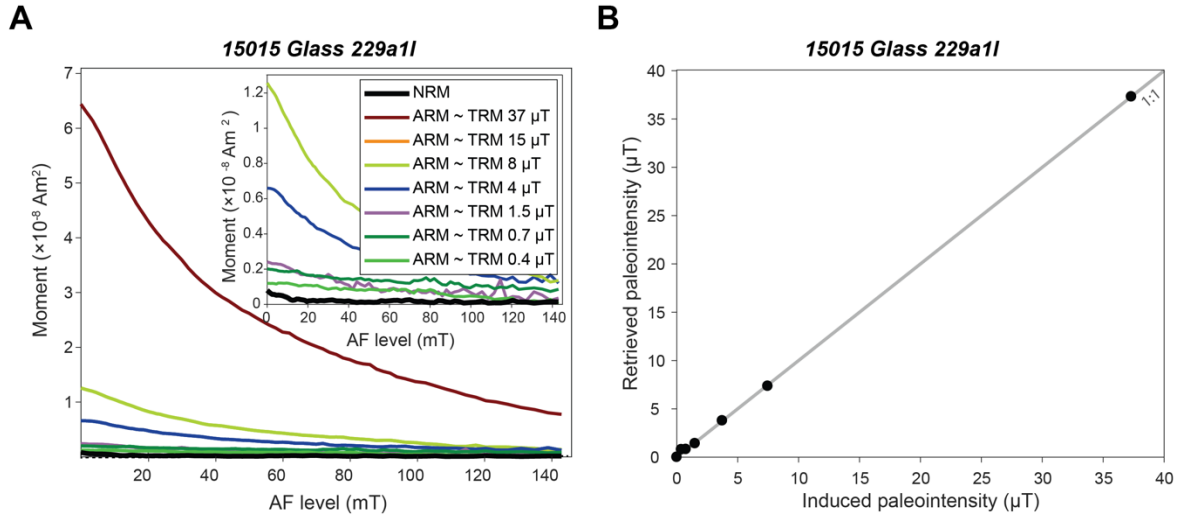


Fig. S21. Paleointensity fidelity tests for breccia 15015. (A) Alternating field (AF) demagnetization of natural remanent magnetization (NRM) compared to that of anhysteretic remanent magnetization (ARM) acquired in different DC bias fields for glass subsample 15015-229a11. Legend lists thermoremanent magnetization (TRM)-equivalent fields for ARMs acquired in a range of DC bias fields in an AF of 260 mT and assuming ARM/TRM = 1.34 (49) (see supplementary text section 4). Horizontal dashed line indicates noise level due to acquisition of spurious ARM due to imperfections in the AF waveform. (B) Recovered paleointensity versus induced paleointensity for different DC fields. Gray lines show the 1:1 line. See table S11B for paleointensity fidelity metrics associated with these experiments.

Table S12. Upper paleointensity limits on breccias using different paleointensity methods.

Breccia	ARM (μT)	IRM (μT)	Double-heating (μT)	AREMc (μT)
15465 glass	-0.58 to 0.77	-0.31 to 0.52	3.2 to 7.9	0.17
15465 demagnetized clast	-0.06	-0.13	-	0.06
15015 glass + clast	-0.02 to 0.21	-0.02 to 0.24	0.24 to 0.42	0.08

Note: The first column lists the lithologies for demagnetized subsamples. For 15465, we report all glass subsamples and the demagnetized clast 6-3; for 15015, we report all subsamples away from the bandsaw cuts (see fig. S15). The second to fourth columns list the range of mean paleointensities for high coercivity (HC)/high temperature (HT) components for these demagnetized subsamples (see tables S6 and S8). The subsample names for these paleointensities are listed in tables S6 and S8 along with their lithology. The fifth column lists the upper paleointensity limits based on the AREMc method. The subsample names and lithologies for the AREMc upper limits are listed in table S7.

however, as discussed in section 4.3, these are extreme upper limits and we can likely retrieve fields even weaker than this value. Overall, clast subsamples had better constrained upper limits compared with glass subsamples, consistent with their more optimal rock magnetic properties (section 6). Based on the best-constrained non-negative upper limit (from the AREMc method), we estimate that the paleointensity was no more than ~0.06 μT for breccia 15465 during its formation.

For both glass and clast-glass lithologies in breccia 15015, the ARM and IRM paleointensities are <0.19 μT and <0.24 μT, respectively. The AREMc method yielded an upper paleointensity limit of <0.08 μT. The double-heating experiments yielded upper limits of <0.35 and <0.35 μT, which are among the weakest paleointensities ever measured using thermal methods on planetary samples. The fidelity tests estimated a minimum recoverable field of 0.7 μT using the ARM

method which, as discussed above, is likely an overestimate. Hence, based on the best-constrained non-negative upper limit (from the AREMc method), we estimate that the paleofield intensity during breccia 15015 formation was below $\sim 0.08 \mu\text{T}$.

Section S5. VRM experiments

5.1. Introduction. To evaluate the origin of the LC/LT components in subsamples, we conducted experiments to estimate the amount of VRM that the breccias acquired in the geomagnetic field after they were returned to the Earth in 1971. The experiments were conducted on 15465 glass subsample 3-1 and 15015 glass subsample 229a1h, both of which had not been previously demagnetized. In the following sections, we describe the magnitude of the gained VRM in the Earth's field and during its subsequent decay in our magnetically shielded room.

5.1. Breccia 15465. 15465 glass subsample 3-1 (mass of 99 mg) was placed in the Earth's field for 23 days. It was then returned to the magnetically shielded room and its moment was measured repeatedly to determine the VRM gained and the VRM decay rate. This experiment was then repeated after AF demagnetizing the subsample to a 145 mT maximum AF to establish whether AF demagnetization influences the VRM decay rate. We found that VRM components of magnitude 3.6×10^{-10} and $4.3 \times 10^{-10} \text{ Am}^2$ (equivalent to 50% and 59% of the initial NRM and 109% and 130% of the LC component, respectively) were acquired during each experiment. For both experiments, it was found that the VRM decayed linearly with respect to the logarithm of time over most of the measured interval (fig. S22A). The measured decay rates over the linear intervals were $-7.35 \times 10^{-11} \text{ Am}^2 [\log(s)]^{-1}$ and $-5.10 \times 10^{-11} \text{ Am}^2 [\log(s)]^{-1}$ in the first and second experiments, respectively, equivalent to mass-normalized rates of $-7.42 \times 10^{-10} \text{ Am}^2 \text{ kg}^{-1} [\log(s)]^{-1}$ and $-5.15 \times 10^{-10} \text{ Am}^2 \text{ kg}^{-1} [\log(s)]^{-1}$. Therefore, the VRM decay rates for both the original NRM and AF-demagnetized state are comparable.

We can use this decay rate to estimate an upper limit on the amount of terrestrial VRM acquired by our 15465 matrix glass subsamples on Earth prior to our NRM analyses. The samples acquired VRM over the last 46 years in the Earth's field at JSC, but then much of this subsequently decayed during the ~ 8 -month period that they were stored in the MIT shielded room prior to the start of our paleomagnetic measurements. Conservatively assuming that the VRM acquisition and decay rates are the same and the sample was stationary at JSC, the gained VRM from NRM after 46 years would be $5.8 \times 10^{-10} \text{ Am}^2$ (80% of original NRM and 175% of LC magnitude) using the VRM decay rate from the first experiment. Considering the subsequent storage in the shielded room, we estimate that the net acquired VRM just prior to our paleomagnetic measurements was $4.0 \times 10^{-11} \text{ Am}^2$ (fig. S22B). This constitutes up to $\sim 60\%$ of the LC component for this subsample and up to 70% of the LC magnitude in the other 15465 subsamples. Therefore, the similar magnitudes of the VRM and LC component suggests that latter could plausibly have been gained in the Earth's field as a VRM. The comparable paleointensity of the LC component to that of the Earth's field (section 4) is further evidence for a VRM origin of the LC component in breccia 15465.

5.2. Breccia 15015. Subsample 229a1h (18.3 mg), which had not been previously demagnetized, was exposed to the Earth's field for 42 days before our VRM decay measurements. A VRM component of magnitude $2.5 \times 10^{-9} \text{ Am}^2$ (equivalent to 1200% of the initial NRM) was gained after 42 days. The VRM decay rate for this glass subsample observed after it was returned to the shielded

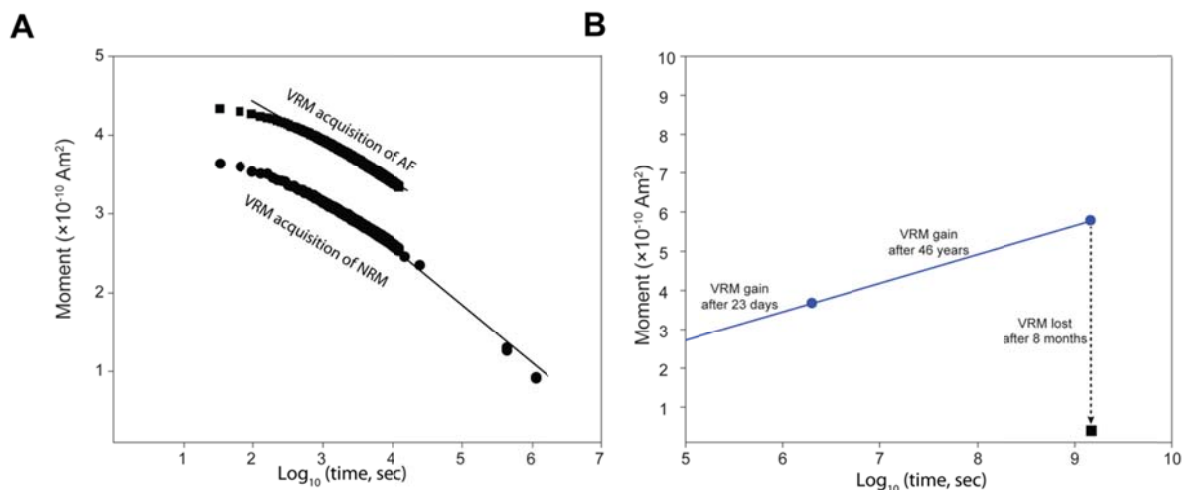


Fig. S22. VRM acquisition by 15465 glass. Shown are VRM experiments and calculations for subsample 3-1. (A) VRM decay as a function of the logarithm of time. Without any prior demagnetization, the sample was first exposed to the Earth's field for 23 days. Circles denote moment measurements of the VRM decay after being returned to the shielded room. The sample was then alternating field (AF)-demagnetized to a peak field of 145 mT and then again exposed for 17 days in the Earth's field. Squares denote moment measurements of the VRM decay after being returned to the shielded room. (B) Observed VRM gain after 23 days from the first experiment (left blue circle), extrapolated VRM after 46 years in the Earth's field (right blue circle), and estimated decayed VRM after storage in the MIT shielded room (black square).

room was $-4.31 \times 10^{-10} \text{ Am}^2 [\log(s)]^{-1}$ over the interval of approximate linearity (fig. S23), equivalent to a mass-normalized rate of $-2.39 \times 10^{-8} \text{ Am}^2 \text{ kg}^{-1} [\log(s)]^{-1}$. Based on this decay rate, the subsample would have gained a VRM of $3.6 \times 10^{-9} \text{ Am}^2$ after 46 years (1,760% of original NRM), which would then have declined to $4.3 \times 10^{-10} \text{ Am}^2$ after storage for 8 months in the shielded room (210% of original NRM). This VRM is larger than the range of original NRM and LC/LT components for most of 15015 subsamples far from the bandsaw edge (see section 3) which supports the possibility of a VRM origin for the LC/LT components in some subsamples (particularly those far from the JSC sawcut surface).

Section S6. Magnetization carriers

6.1. Methods. We characterized the composition and mineralogy of the ferromagnetic grains in breccias 15465 and 15015 using backscattered scanning electron microscopy (SEM) and wavelength dispersive spectroscopy (WDS) in the MIT Electron Microprobe Facility using a JEOL-JXA-8200 electron microprobe. For WDS, we analyzed Fe, Ni, S, Si, Ti, O, Cr, Al, W, Co, and P using a 15 kV, 10 nA beam with a diameter of 1 μm . For smaller grains (<5 μm in diameter), we acquired single-point WDS measurements, while for larger grains (diameters from 5 to 25 μm), we acquired WDS measurements along within-grain transects to search for compositional zoning and any exsolution textures.

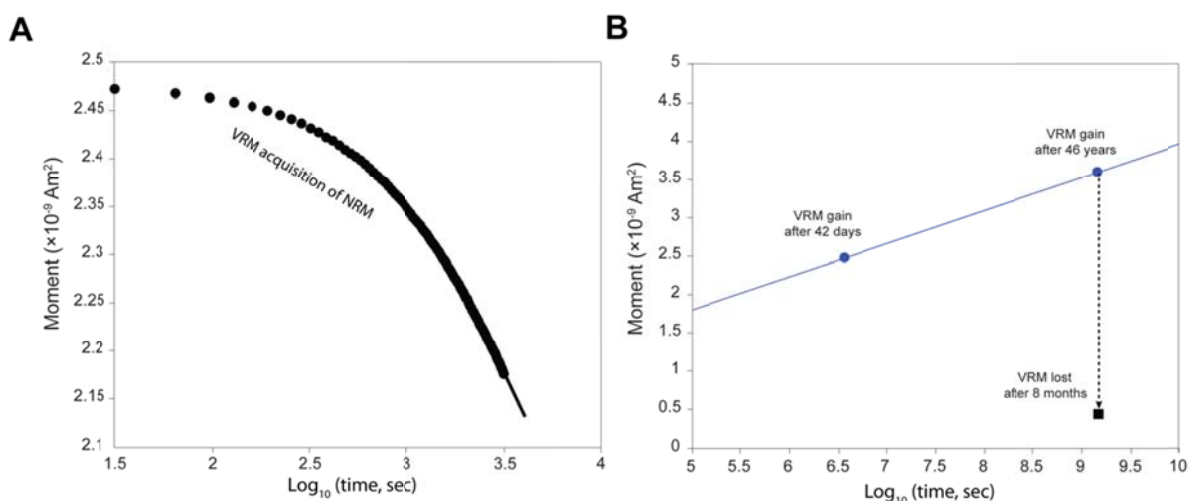


Fig. S23. VRM acquisition by 15015 glass. Shown are VRM experiments and calculations for subsample 229a1h. (A) VRM decay as a function of the logarithm of time. After an undemagnetized sample was left in the Earth's field for 42 days, the VRM decay was measured in the shielded room (circles). (B) Observed VRM gain after 42 days (left blue circle), extrapolated VRM after 46 years in the Earth's field (right blue circle) and estimated decayed VRM after storage in the MIT shielded room (black square).

We characterized the domain state of the ferromagnetic grains by acquiring magnetic hysteresis curves, first order reversal curves (FORCs) and conducting IRM acquisition, AF demagnetization of IRM and backfield IRM acquisition. Hysteresis curves and FORCs were measured in the Ross Laboratory in the MIT Department of Material Sciences and Engineering using a vibrating sample magnetometer (VSM) (varying the field from -0.56 to 1.13 T for 106 minor loops over a period of ~6 hours). IRM acquisition and demagnetization were conducted in the MIT Paleomagnetism Laboratory using the SRM.

The hysteresis curves yielded the saturation magnetization (M_s), saturation remanent magnetization (M_{rs}), and the coercive force (H_c). The coercivity of remanence (H_{cr}) was obtained as the AF level at which the IRM acquisition and backfield IRM intersected (30). We use the Dunlop-Day plot (M_{rs}/M_s versus H_{cr}/H_c) as a qualitative tool for assessing the magnetic domain state (82, 83), with a caveat that this plot was developed originally for magnetite-bearing rocks. The FORC curves were processed using FORCinel software v. 3.0 (84) with smoothing factors of 7 (horizontal) and 21 (vertical).

6.2. Breccia 15465

6.2.1. Electron microscopy. Our electron microscopy analyses show that the metal grains in 15465 matrix glass and the 20-mm diameter regolith breccia clast have sizes ranging from <1 to 30 μm in diameter (table S13 and fig. S24).

We found that two metal grains in the clast have homogenous, unzoned compositions of Fe_{100} and $\text{Fe}_{92-100}\text{Ni}_{0-8}$ (grains #5 and #6 in table S13), indicating the presence of kamacite and martensite. Given the latter grain's Ni content of ~8 mass %, its martensite-start and austenite-start temperatures should be ~600 $^{\circ}\text{C}$ and ~710 $^{\circ}\text{C}$ (85). The presence of kamacite and the narrow temperature interval (~100 $^{\circ}\text{C}$) over which the martensite grain formed from kamacite

indicate the clast should dominantly have acquired a TRM during primary cooling. During laboratory thermal demagnetization, kamacite should completely unblock by its 780°C Curie point, while martensite should transform to taenite at the austenite-finish temperature. This indicates that thermochemical alteration should begin to set in by ~710°C in our thermal paleointensity experiments.

In the matrix glass, we found one metal grain with a homogenous kamacite composition of Fe_{93%}Ni_{5%} composition (herewith “%” denotes wt. %), a second grain consisting of a two-phase assemblage of kamacite (Fe_{96-98%}Ni_{0-2%}) and troilite (FeS), and two other grains consisting of three-phase assemblages of kamacite (Fe_{94-97%}Ni_{4-5%}), schreibersite (Fe_{79-8%}2Ni_{8%}P_{10-13%}), and troilite (table S13). Assemblages with similar compositions have previously been found in lunar samples contaminated with meteoritic material, such as Apollo 12 soil [up to ~16 mass % P (86)] and the basalt 14310 [up to 12 mass % P (87)]. Given phase relations in the Fe-Ni-P ternary system (88), this assemblage should have last equilibrated at 750 ± 50 °C. Given its Ni-content, the schreibersite in 15465 should have a Curie temperature of ~440 °C (89). Because this is well below the 750 ± 50 °C equilibrium temperature, schreibersite should have recorded any paleofield in the form of a total TRM during primary cooling. Because the 750 ± 50 °C equilibrium temperature is also within error of kamacite’s 780°C Curie point, kamacite in the matrix glass also should have recorded a near-total TRM during primary cooling. Troilite is widely considered to be antiferromagnetic and so should not record NRM. Although it has been suggested that troilite may carry remanence (73), it has not yet been demonstrated that this remanence is instead from small inclusions of other ferromagnetic minerals (90) (e.g., metallic Fe, which very commonly co-crystallizes with FeS as observed in 15465).

Table S13. WDS of 15465 metal grains.

Grain	Lithology	Spot	Fe	Ni	Cr	Co	P	S	Si	Al	W	O	Ti	Total
1	Glass	1	96.9	3.9	0.0	0.6	1.1	0.0	0.0	0.0	0.0	0.6	0.0	103.1
		2	95.8	4.1	0.1	0.7	2.0	0.0	0.0	0.0	0.0	0.6	0.0	103.3
		3	94.7	4.2	0.0	0.7	2.6	0.0	0.0	0.0	0.4	0.7	0.0	103.3
		4	95.2	4.1	0.0	0.6	2.4	0.0	0.0	0.0	0.2	0.6	0.0	103.1
		5	94.6	4.2	0.1	0.7	2.0	0.0	0.0	0.0	0.1	0.7	0.0	102.4
		6	93.6	4.3	0.0	0.7	1.6	0.1	0.0	0.0	0.0	0.7	0.0	101.0
		7	83.3	6.1	0.0	0.7	10.0	0.2	0.0	0.0	0.2	0.6	0.0	101.1
		8	78.8	7.6	0.0	0.5	13.0	0.2	0.0	0.0	0.0	0.5	0.0	100.6
2	Glass	9	95.3	5.0	0.0	0.7	1.4	0.0	0.0	0.0	0.3	0.6	0.0	103.3
		10	81.6	8.0	0.0	0.6	12.0	0.5	0.0	0.0	0.0	0.5	0.0	103.2
		11	68.0	0.6	0.1	0.1	1.1	30.1	0.0	0.0	0.0	0.7	0.0	100.7
		12	80.9	8.1	0.0	0.6	11.8	0.8	0.0	0.0	0.0	0.7	0.0	102.9
		13	82.2	8.0	0.0	0.6	11.0	0.8	0.0	0.0	0.3	0.5	0.0	103.4
		14	70.6	0.8	0.0	0.2	0.6	27.2	0.0	0.0	0.0	0.9	0.0	100.3
		15	81.9	8.1	0.0	0.6	10.8	0.5	0.0	0.0	0.2	0.6	0.0	102.7
3	Glass	16	96.8	1.4	0.0	0.4	1.9	0.0	0.0	0.0	0.2	1.4	0.0	102.1
		17	67.5	0.2	0.1	0.1	2.5	27.6	0.0	0.0	0.0	0.5	0.0	98.5
		18	98.6	1.4	0.0	0.4	1.9	0.0	0.0	0.0	0.0	0.6	0.1	103.5
4	Glass	19	92.8	4.3	0.1	0.8	0.7	0.1	0.2	0.1	0.4	1.9	0.0	101.4
5	Clast	20	100.7	0.4	0.0	0.9	0.0	0.0	0.0	0.0	0.0	0.6	0.3	102.9
		21	101.3	0.4	0.0	0.8	0.0	0.0	0.0	0.0	0.0	0.6	0.2	103.3
		22	100.8	0.4	0.0	0.9	0.0	0.0	0.0	0.0	0.2	0.7	0.2	103.2
		23	100.1	0.4	0.0	0.9	0.0	0.0	0.0	0.0	0.0	0.6	0.1	102.1
6	Clast	24	91.4	8.2	0.0	0.5	0.1	0.0	0.1	0.0	0.0	0.5	0.0	100.8
		25	92.7	8.0	0.0	0.5	0.1	0.0	0.0	0.0	0.0	0.6	0.0	101.9
		26	91.2	8.8	0.0	0.5	0.1	0.0	0.1	0.0	0.2	0.7	0.0	101.6

Note: The first column lists the number of the grain depicted in fig. S24. The second column lists the grain’s host lithology. The third column lists the spot number as shown in fig. S24. The fourth to fifteenth columns list the element concentrations in mass percent.

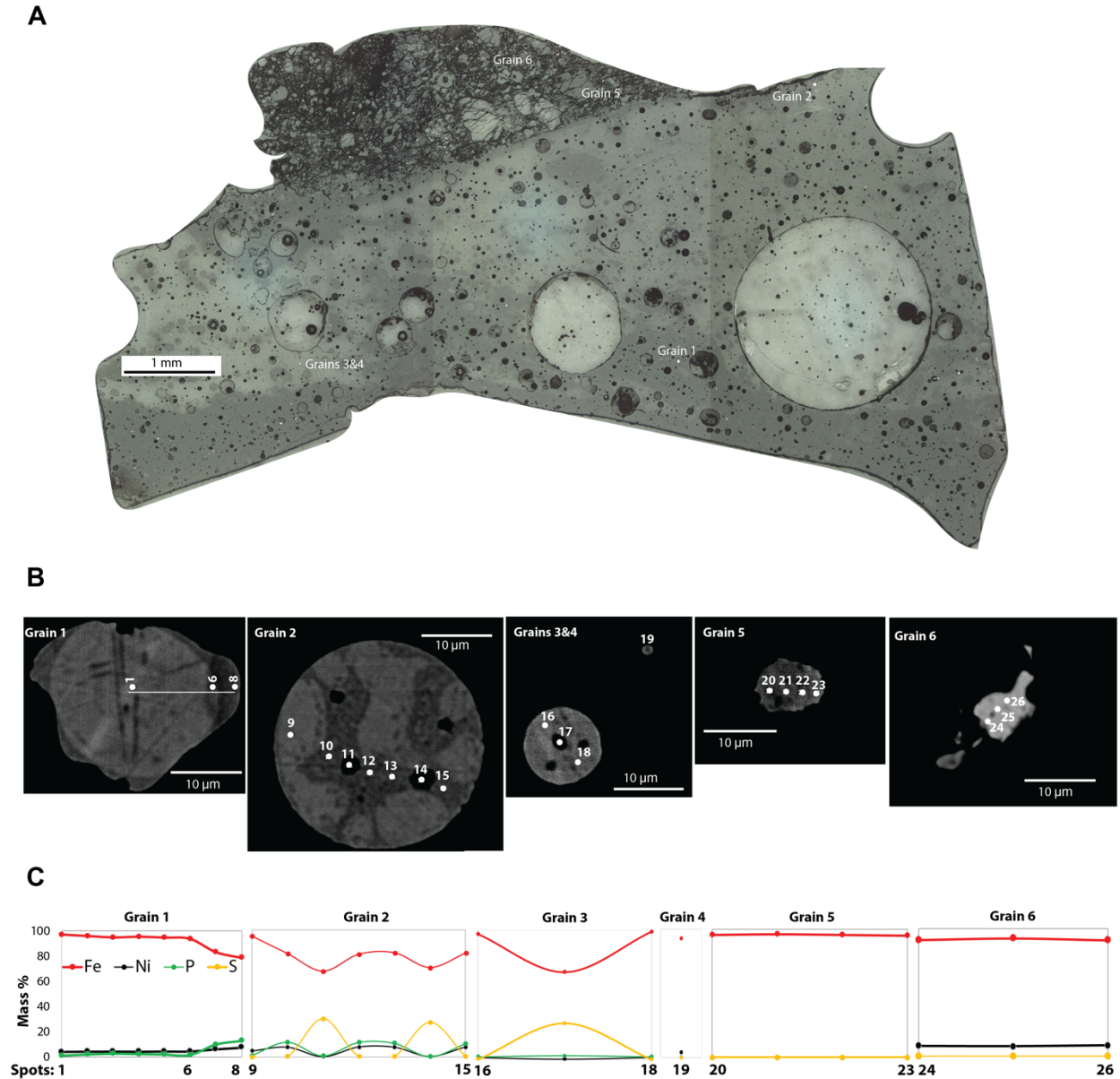


Fig. S24. Electron microprobe analysis of magnetization carriers in 15465. (A) Reflected plane-polarized light image of 30 μm thin section from parent split 15465,114 which we chipped from parent mass 44 at Johnson Space Center (JSC) (same thin section as imaged in fig. S1). Image shows a clast fragment (top part of the section) bonded to the matrix glass (bottom part). The clast in this section is sampled from the same parent clast on which we conducted our paleomagnetic experiments. The numbers indicate the metal grains which we have selected for detailed microprobe study. The small white spots are metal grains ($<30\ \mu\text{m}$). (B) Backscattered scanning electron microscopy (BSEM) images. (C) Wavelength dispersive spectroscopy (WDS) of the selected Fe grains in (A). Grains 1, 2, 3, and 4 are inside the matrix, while grains 5 and 6 are inside the clast. Numbers in (B, C) indicate the WDS measurement spot numbers. See table S13 for detailed measurements.

6.2.2. Hysteresis and FORC measurements. We conducted hysteresis measurements on glass sample 6-5 (mass of 33.1 mg) and clast sample 6-3 (mass of 55.7 mg) (fig. S25). Their bulk hysteresis parameters (table S14 and fig. S26) indicate that the clast has a mean single-domain (SD) to superparamagnetic (SP) grain size while the glass has a mean multi-domain (MD) grain size close to the pseudo-single domain (PSD) boundary. In the FORC diagram (fig. S27), the presence of a horizontal ridge extending to high coercivities (>200 mT) for both lithologies demonstrates the presence of a population of SD and PSD grains. In the glass, the cluster near zero-coercivity elongated along the B_u axis is consistent with the presence of MD grains; this low-coercivity cluster is largely absent from the clast, indicating it is dominantly SD to SV. Overall, the hysteresis and FORC data indicates that both lithologies, and especially the clast, have unusually good magnetic recording properties compared to most Apollo samples (25).

Table S14. Rock magnetic parameters for 15465 and 15015 subsamples.

Subsample	M_s (Am ²)	M_{rs} (Am ²)	H_c (mT)	H_{cr} (mT)
15465 Glass 6-5	17.9×10^{-6}	3.01×10^{-7}	5.43	93
15465 Clast 6-3	3.81×10^{-6}	3.22×10^{-7}	6.03	75
15015 Glass 229b2b	19.0×10^{-6}	2.61×10^{-6}	7.00	44

Note: The first column lists the subsample name and its lithology. The second column lists the saturation magnetization, M_s . The third column lists the saturation remanent magnetization, M_{rs} . The fourth column lists the coercivity H_c . The magnetic parameters in the second to fourth columns are obtained from the hysteresis curves in figs. S25 and S29. The fifth column lists the coercivity of remanence, H_{cr} , which is obtained from the intersection of the isothermal remanent magnetization (IRM) acquisition and demagnetization curves in figs. S25 and S29.

6.3. Breccia 15015

6.3.1. Electron microscopy

SEM studies of breccia 15015 of the surface matrix glass showed that this breccia contains PSD to SD grains (~4 to ~100 nm diameter) (91). Previous transmission electron microscopy (TEM) combined with x-ray electron dispersive spectroscopy (EDS) studies of fine metal particles in the glass showed that their Ni content varied between 1.0 to 3.8 mass % indicating they are in the form of kamacite (23). The fine grain sizes mean the matrix glass in this breccia is also an exceptionally good recorder among Apollo samples.

Our electron microscopy of larger metal grains (with diameters from 3-15 μ m) in 15015 matrix glass found that the four grains consist of a three-phase assemblage of kamacite (Fe_{94-97%}Ni_{1-3%}), schreibersite (Fe_{70-85%}Ni_{3%}P_{6-18%}), and troilite (table S15). Similar to the three-phase 15465 metallic grains described in section 6.2, these grains suggest meteoritic contamination of the breccia's parent materials. As with 15465, this assemblage should have last equilibrated at 750 ± 50 °C [see ref. (88)], while the schreibersite in 15015 should have a Curie temperature of ~440 °C (89). Because this is well below the 750 ± 50 °C equilibrium temperature, schreibersite should have recorded any paleofield in the form of a total TRM during primary cooling. Because the 750 ± 50 °C equilibrium temperature is within error of kamacite's 780°C Curie point, kamacite in the matrix glass also should have recorded a near-total TRM during primary cooling.

6.3.2. Magnetic hysteresis measurements. Since our paleomagnetic analyses and interpretations of 15015 did not rely on clast subsamples, we conducted hysteresis analyses only on glass

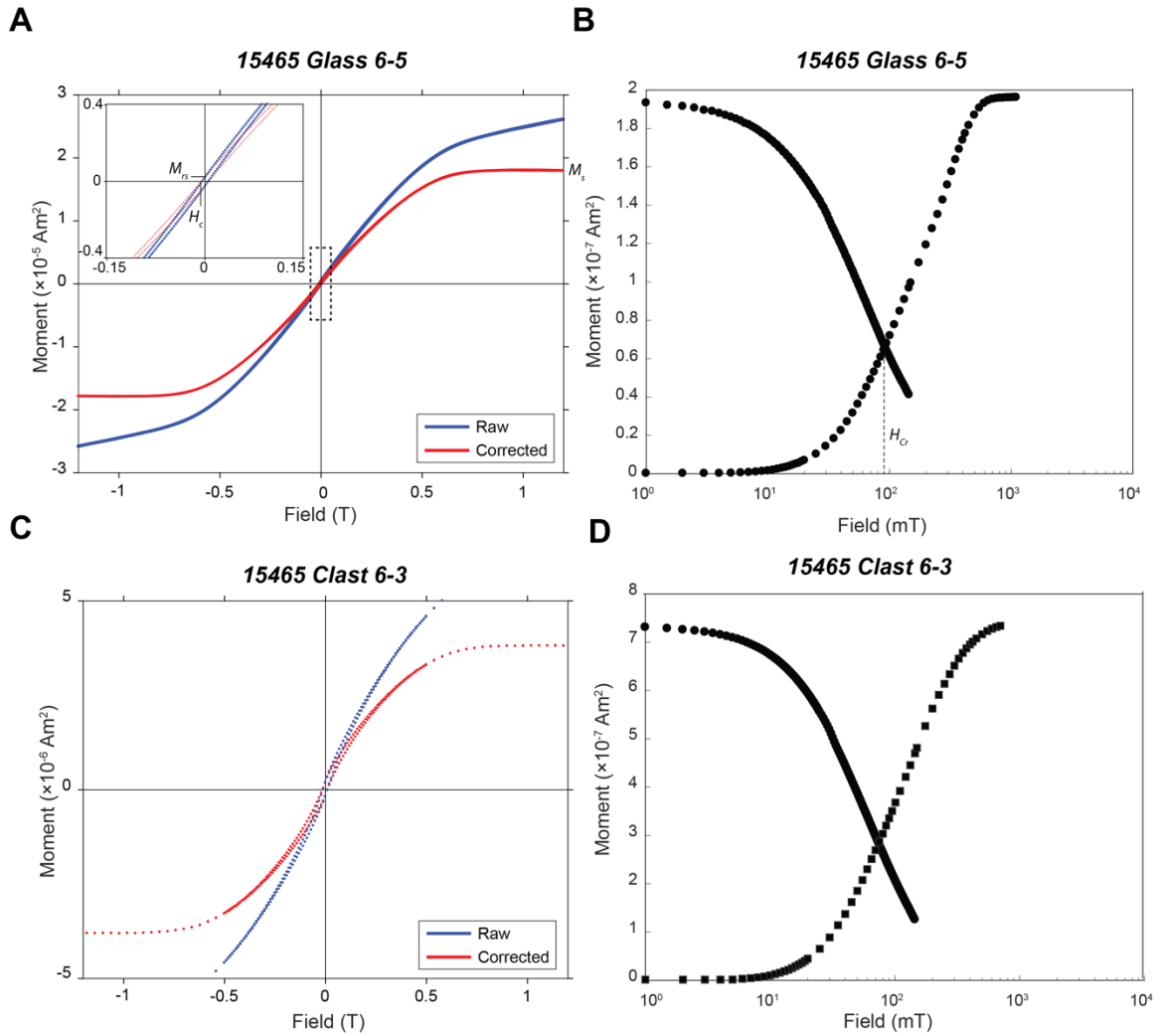


Fig. S25. Hysteresis and IRM acquisition/demagnetization curves for 15465 glass and clast subsamples. (A) Hysteresis curve for glass subsample 6-5. Blue dots are raw measurements and red points are corrected for the high-field paramagnetic slope. Inset shows a magnified view. (B) IRM acquisition and backfield IRM for glass subsample 4-1. These curves yield M_{rs} , M_s , H_c (from hysteresis curve) and H_{cr} (from backfield IRM curve) as indicated in table S14. (C) Hysteresis curve for clast subsample 6-3. (D) IRM acquisition and backfield IRM measured for clast subsample 6-3.

subsample 229b2b. Based on the measured hysteresis parameters for 15015 (table S14, figs. S26 and S29) and its FORC diagram (fig. S30), the matrix glass has a dominantly SD to SP metal grain size with grains with coercivities >100 mT. These measurements again indicate that the matrix glass in 15015 is an exceptional recorder.

Section S7. $^{40}\text{Ar}/^{39}\text{Ar}$, $^{38}\text{Ar}/^{37}\text{Ar}$, and $^{40}\text{Ar}/^{36}\text{Ar}$ chronometry

7.1 Overview. In this section, we discuss constraints on the age of magnetic records in 15465 and 15015 as well as on the lunar sample with the youngest confirmed record of the existence of the

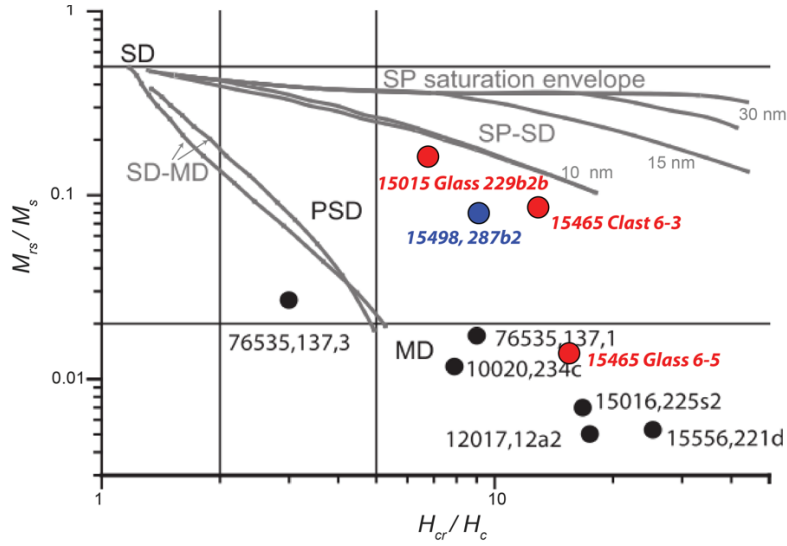


Fig. S26. Dunlop-Day plot showing the domain state of breccias compared to other lunar rocks analyzed in the MIT Paleomagnetism Laboratory. Shown is M_{rs}/M_s versus H_{cr}/H_c for 15465 and 15015 (red points), matrix glass in regolith breccia 15498 (blue point) (9), mare basalts (10020, 12017, 15016, and 15556) and a troctolite (76535) measured in the MIT Paleomagnetism Laboratory (25) (black points). Although this plot was designed for magnetite-bearing rocks (82, 83), we use it as a qualitative tool for metal-bearing lunar rocks. The vertical and horizontal lines classify the parameter space for SD (single-domain), pseudo-single domain (PSD), multi-domain (MD), and their mixtures. The gray curves indicate the superparamagnetic (SP) saturation envelopes for different grain sizes. See table S14 for hysteresis parameters for 15465 and 15015. Adapted from ref. (25).

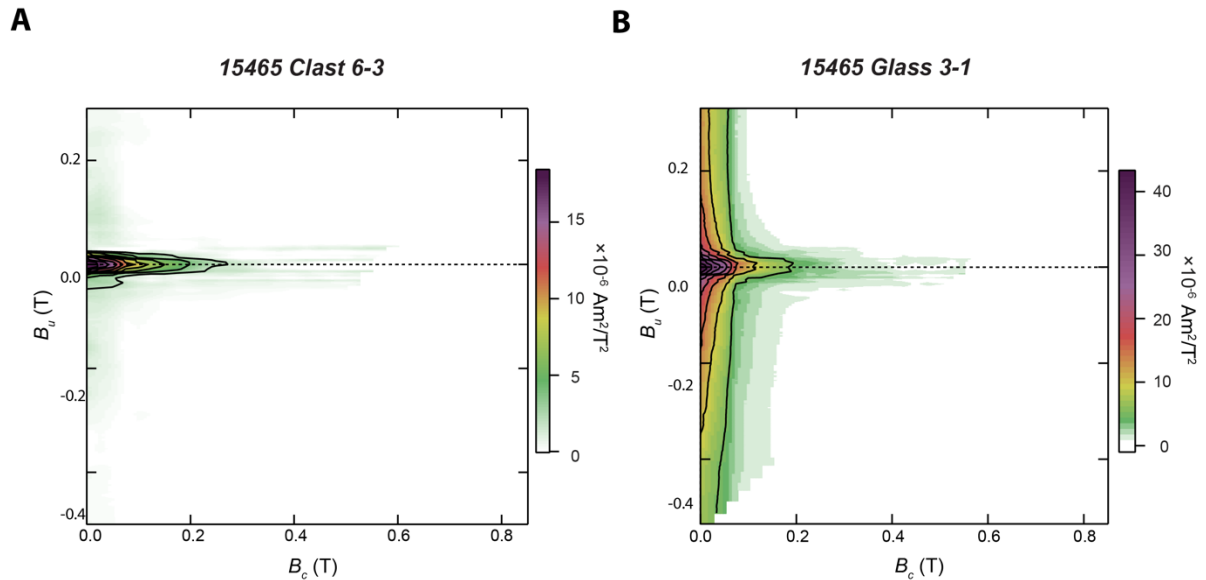


Fig. S27. FORC analysis of 15465 breccia subsamples. (A) 15465 clast subsample 6-3. (B) 15465 glass subsample 3-1. The vertical and horizontal axes represent the local interaction field (B_u) and magnetic coercivity (B_c), respectively. The color represents probability density of hysteron for a certain B_u and B_c . These diagrams were generated using the FORCinel v. 3.0 software package (84).

Table S15. WDS of 15015 metal grains.

Grain	Lithology	Spot	Fe	Ni	P	S	Total
1	Glass	1	96.4	2.4	1.0	0.0	99.8
		2	96.2	2.3	1.0	0.0	99.5
		3	84.6	3.1	11.3	0.8	99.8
		4	84.6	3.0	11.0	0.8	99.4
		5	96.1	2.3	0.8	0.0	99.2
		6	95.7	2.3	0.9	0.0	98.9
2	Glass	7	88.9	2.5	6.4	0.7	98.5
		8	85.5	2.2	6.6	3.9	98.2
		9	88.4	2.3	6.0	2.0	98.7
3	Glass	10	92.5	2.2	3.8	0.4	98.9
		11	84.3	3.5	10.5	1.0	99.3
		12	78.2	1.3	2.7	16.7	98.9
4	Glass	13	79.0	1.6	6.9	9.6	97.1
		14	85.7	2.2	9.8	0.2	97.9
		15	93.6	1.5	3.6	0.1	98.8

Note: The first column lists the number of the grain depicted in fig. S28. The second column lists the grain's host lithology. The third column lists the spot number as shown in fig. S28. The fourth to eights columns list the element concentrations in mass percent.

lunar dynamo, 15498. We employ a combination of three different Ar isotopic methods—radiometric dating via the $^{40}\text{Ar}/^{39}\text{Ar}$ method (92), $^{38}\text{Ar}/^{37}\text{Ar}$ cosmic ray exposure (CRE) age dating (93), and the trapped $^{40}\text{Ar}/^{36}\text{Ar}$ antiquity indicator (94, 95)—to constrain the age of the samples. For the trapped antiquity indicator, we use the age versus trapped $^{40}\text{Ar}/^{36}\text{Ar}$ relationship in equation (6) of ref. (95), which we augmented here by estimating 1- σ confidence intervals on the two fit parameters using a two-tailed Student's t test

$$t = (1.2107 \pm 0.0689)\ln(\text{Ar}_{\text{tr}}) + 0.7151 \quad (\text{S15})$$

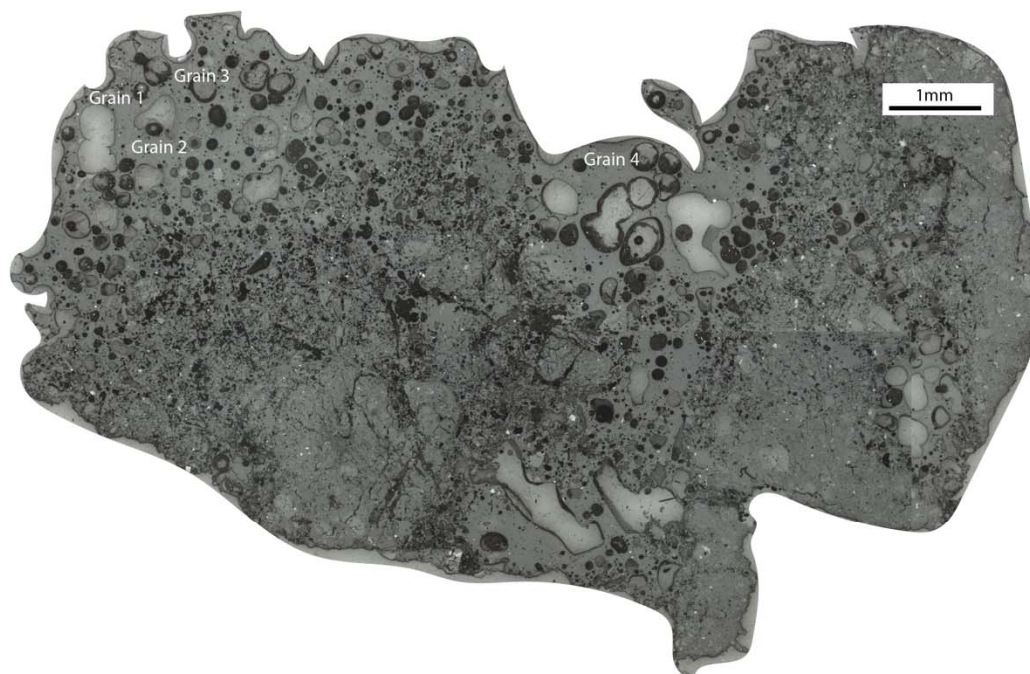
where t has units of Ga and Ar_{tr} is the trapped $^{40}\text{Ar}/^{36}\text{Ar}$ value.

We combine previously measured Ar measurements on 15465 and 15016 (section 7.2) with our new measurements (section 7.3) to infer the age of the magnetic records in these samples. The textures of these breccias indicate that their clasts must predate the event that assembled them and produced the melt glass matrix welding them together. Given that the magnetic record of zero-field conditions is held by the matrix glass and clast materials baked during breccia assembly, we estimate when this melt-generating breccia assembly event occurred for each sample (section 7.4). We end by reviewing the implications of previous $^{40}\text{Ar}/^{39}\text{Ar}$, $^{38}\text{Ar}/^{37}\text{Ar}$, and $^{40}\text{Ar}/^{36}\text{Ar}$ chronometry measurements for the assembly age of breccia 15498 (section 7.5).

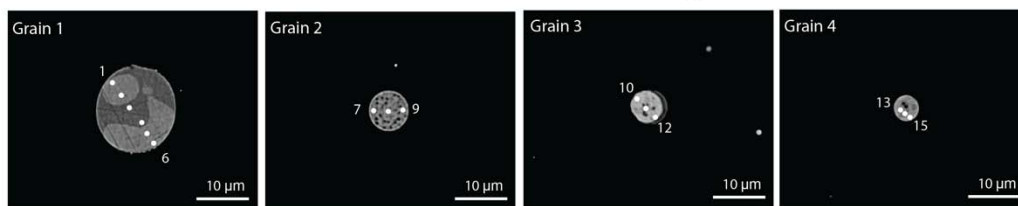
7.2. Previous analyses

7.2.1. Breccia 15465. $^{40}\text{Ar}/^{39}\text{Ar}$ ages of a diversity of clasts (KREEP basalt, norites, glass spheres, and fragments) define an isochron age of 3.91 ± 0.04 Ga, suggesting that these materials formed at or before this time (54). Such an old age for the KREEP basalts and norites is consistent with measured ages for these lithologies of 3.9–4.2 Ga from other Apollo samples (96). $^{40}\text{Ar}/^{39}\text{Ar}$ ages of feldspar crystals in mare basalt clasts yielded an apparent isochron age of 1.9 Ga (54); this is likely a minimum age for the crystallization of these clasts given the absence of mare volcanism at the Apollo site after ~ 3.3 Ga (96), such that they reflect degassing associated with reheating

A



B



C

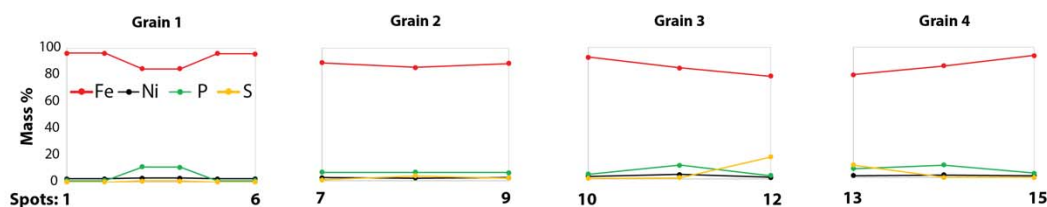


Fig. S28. Electron microprobe analysis of magnetization carriers in 15015. (A) Reflected plane-polarized light image of a 30 μm thin section from parent split 15015, 237. Image shows a clast-glass mixture, with dominant matrix glass at the top part of the section bonded to the clast. The numbers indicate the metal grains selected for detailed microprobe study. The small white spots in the reflected light section are the metal grains ($<30 \mu\text{m}$ in size). (B) Backscattered scanning electron microscopy (BSEM) images. (C) Wavelength dispersive spectroscopy (WDS) of the selected Fe grains in (A). Grains 1, 2, 3, and 4 are inside the matrix glass. Numbers in (B, C) indicate the WDS measurement spot numbers. See table S15 for detailed measurements.

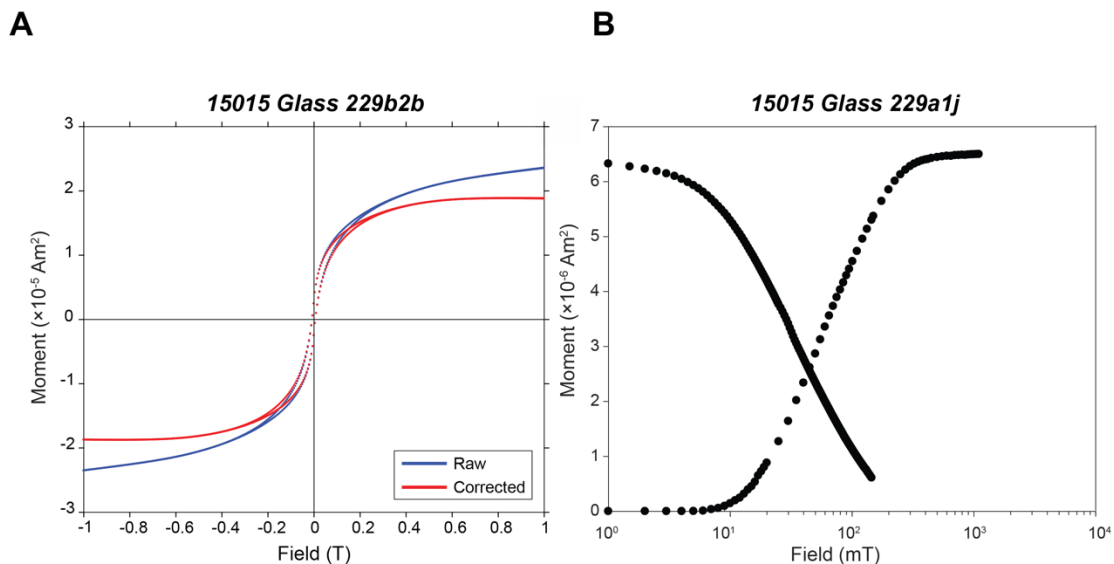


Fig. S29. Hysteresis and IRM acquisition/demagnetization curves for 15015 glass subsamples. (A) Hysteresis curve for glass subsample 229b2b. Blue dots are raw measurements and red points are corrected for high-field paramagnetic slope. (B) IRM acquisition and backfield IRM for 15015 glass subsample 229a1j.

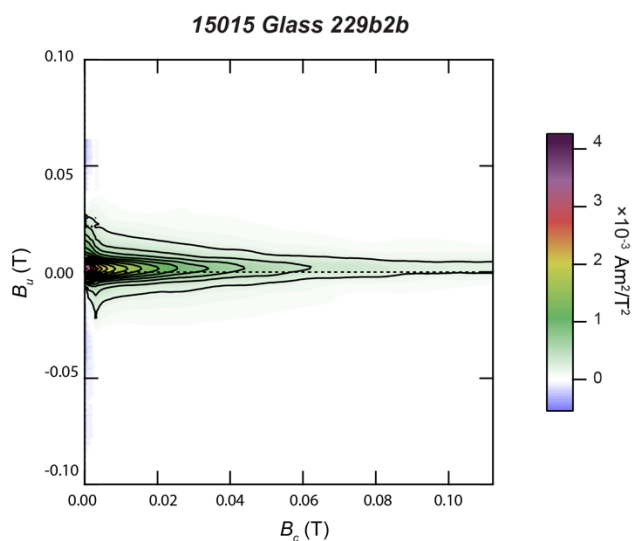


Fig. S30. FORC analysis for 15015 glass. The vertical and horizontal axes represent the local interaction field (B_u) and magnetic coercivity (B_c), respectively. The color represents probability density of hysteron for a certain B_u and B_c . This diagram was generated using the FORCinel v. 3.0 software package (84). Measurements conducted on subsample 229b2b.

from assembly of 15465. Further evidence for this reheating is provided by even younger 1.0 ± 0.5 Ga $^{40}\text{Ar}/^{39}\text{Ar}$ isochron ages measured for the glassy mesostases of these mare basalt clasts (54).

The matrix glass has itself been the subject of one previous $^{40}\text{Ar}/^{39}\text{Ar}$ study, which estimated a minimum age of 1.09 Ga (97). However, because no detailed description of the analyses or data is presented in the latter publication, we do not consider it to be a useful constraint on the glass formation age. Likewise, a trapped $^{40}\text{Ar}/^{36}\text{Ar}$ age of ~ 1.9 Ga was recently estimated for 15465 (40) based on previously published $^{40}\text{Ar}/^{36}\text{Ar}$ measurements (22), but the contribution of in-situ-produced radiogenic ^{40}Ar was not measured for this sample (22) and the lithology of the analyzed subsample was not described, such that the uncertainty on this age is difficult to quantify. Overall, the previous data, while not conclusive, suggest that the age of breccia assembly and formation of the associated melt glass matrix is almost certainly younger than ~ 2 Ga.

7.2.2. Breccia 15015. $^{40}\text{Ar}/^{39}\text{Ar}$ studies of a variolitic feldspathic basalt and a Fra Mauro (i.e., KREEP) basalt clast reported apparent ages of 3.4 and 3.7 Ga, respectively, at $>80\%$ ^{39}Ar release fractions, with steps at lower ^{39}Ar release fractions exhibiting younger apparent ages. This suggests that these clasts formed at ≥ 3.4 and ≥ 3.7 Ga and then were partially degassed at a later time, likely by the event which assembled and formed the breccia 15015 (57). Such old crystallization ages are consistent with the lithologies of these clasts [Apollo 15 KREEP basalts have Sm-Nd ages of 3.85 Ga (98)]. CRE ages for the variolitic feldspathic basalt clast suggest that it was pre-irradiated on the lunar surface for 800 My prior to its assembly into 15015; this indicates that the breccia must have formed after $3.4 - 0.8 = 2.6$ Ga (57). Consistent with the assembly occurring after this time, ref. (57) also reported $^{40}\text{Ar}/^{39}\text{Ar}$ isochron ages of ~ 0.8 and 1.2 Ga for two samples of the matrix glass. Furthermore, the trapped $^{40}\text{Ar}/^{36}\text{Ar}$ value of 1.17 ± 0.04 measured by ref. (57) for these same matrix glass samples independently indicate a breccia assembly age of 0.91 ± 0.20 Ga, calculated using equation (S15) where the uncertainties take into account both those for the trapped $^{40}\text{Ar}/^{36}\text{Ar}$ calibration and the measured trapped $^{40}\text{Ar}/^{36}\text{Ar}$ value. Finally, as with 15465, a trapped $^{40}\text{Ar}/^{36}\text{Ar}$ age of ~ 0.5 Ga was recently estimated for 15015 (40) based on previously published $^{40}\text{Ar}/^{36}\text{Ar}$ measurements (22), but again the uncertainty on this age is difficult to quantify because the contribution of the in-situ-produced radiogenic ^{40}Ar was not measured in the latter study and the sample lithology was not reported (22). Overall, these data indicate that 15015 likely formed after ~ 1 Ga.

7.3. Our ^{40}Ar and ^{38}Ar geochronology analyses

7.3.1. Overview of analyses. We conducted stepwise degassing $^{40}\text{Ar}/^{39}\text{Ar}$ and $^{38}\text{Ar}/^{37}\text{Ar}$ analyses using feedback-controlled laser heating on four, neutron-irradiated subsamples of breccias 15465 and 15015 at the Berkeley Geochronology Center following analytical procedures and irradiation conditions as described in refs. (4, 8, 46). The subsamples analyzed from 15465 were matrix glass 6-4-1 and clast 6-2 (fig. S7) and those from 15015 were matrix glass 229b1 and clast 229a1a (fig. S11). Although no large clasts were present in our matrix glass samples, we cannot completely exclude the possibility that they contain small clasts with inherited radiogenic ^{40}Ar that accumulated prior to the assembly of the breccia. Complete stepwise Ar release data, extraction temperatures, neutron irradiation conditions and assumed constants are reported in tables S16-S19, and release spectra calculated from these data are shown in figs. S31-S34.

We calculated apparent $^{40}\text{Ar}/^{39}\text{Ar}$ ages for each degassing step relative to the Hb3gr fluence monitor [age = 1081 Ma (47)] using the decay constants of ref. (47) and the isotopic abundances of ref. (48). In our calculations for $^{40}\text{Ar}/^{39}\text{Ar}$ step ages for the 15465 glass 6-4-1, 15465 clast 6-2, and 15015 glass 229b1, we corrected for the trapped ^{40}Ar using the ordinate-intercept $^{40}\text{Ar}/^{36}\text{Ar}$ ratios determined by error-weighted linear regressions in 3-isotope plots (figs. S35-S37). We assumed each sample's inherent ^{36}Ar (i.e., after applying small corrections for the ^{36}Ar produced during neutron irradiation and via cosmic ray interactions) was trapped prior to radiogenic ^{40}Ar accumulation and is indicated by the intercept ratio. Because the 15015 clast subsample 229a1a is itself a regolith breccia containing lunar materials of diverse origins and because it exhibits no significant correlation observed between $^{40}\text{Ar}/^{36}\text{Ar}$ and $^{39}\text{Ar}/^{36}\text{Ar}$, we do not apply a correction for trapped Ar in this sample. We also calculated the apparent cosmogenic ^{38}Ar exposure ages for each degassing step following the procedures described in ref. (46). The apparent $^{40}\text{Ar}/^{39}\text{Ar}$ age, cosmogenic ^{38}Ar age, and Ca/K release spectra for the four samples are shown in figs. S31-S34.

7.3.2. 15465.

7.3.2.1. Glass subsample. The Ar release spectra of glass 6-4-1 have concordant $^{40}\text{Ar}/^{39}\text{Ar}$ ages and cosmogenic ^{38}Ar exposure ages in the majority of the heating steps (fig. S31). Corrections to the $^{40}\text{Ar}/^{39}\text{Ar}$ step ages for the trapped ^{40}Ar using the intercept $^{40}\text{Ar}/^{36}\text{Ar}$ (0.88 ± 0.63) were ~10-20 % for glass 6-4-1 (fig. S35). This glass presents little evidence of diffusive loss of both ^{40}Ar and ^{38}Ar as shown by the concordance of step ages at low release fractions. Error-weighted means ages calculated from the steps released between ~6-87 % of the cumulative release fraction of ^{39}Ar are 437 ± 11 Ma and 432 ± 7 Ma for $^{40}\text{Ar}/^{39}\text{Ar}$ and cosmogenic ^{38}Ar data, respectively. Agreement between these two results indicates that the timing of glass formation was likely ~0.44 Ga. This age is consistent with the $0.56^{+0.83}_{-0.56}$ Ga breccia formation age implied by the trapped $^{40}\text{Ar}/^{36}\text{Ar}$ component in the glass, estimated using equation (S15) where the uncertainties again take into account both those associated with the trapped $^{40}\text{Ar}/^{36}\text{Ar}$ calibration and in the measured trapped $^{40}\text{Ar}/^{36}\text{Ar}$ value.

7.3.2.2. Clast subsample. The Ar release spectrum of clast 6-2 has systematically increasing apparent $^{40}\text{Ar}/^{39}\text{Ar}$ ages and cosmogenic ^{38}Ar exposure ages throughout the initial ~60% of the released gas (fig. S32); this is indicative of open system behavior and significant diffusive loss of ^{40}Ar and ^{38}Ar from these samples, likely due to a combination of heating when it was assembled into the breccia and by later solar heating at the lunar surface (46). Corrections to $^{40}\text{Ar}/^{39}\text{Ar}$ step ages for trapped ^{40}Ar using the intercept $^{40}\text{Ar}/^{36}\text{Ar}$ (2.36 ± 0.43) shown in fig. S36 were ~10-20 % for clast 6-2. The error-weighted mean which was calculated from the initial 5 heating steps yields an apparent $^{40}\text{Ar}/^{39}\text{Ar}$ age of 82 ± 1 Ma. The error-weighted mean calculated from the 9 highest temperature heating steps (amounting to 40% of the released ^{37}Ar) yields an apparent $^{40}\text{Ar}/^{39}\text{Ar}$ age of 3390 ± 64 Ma. We thus interpret the clast formation timing to be >3.39 Ga, similar to that of the previously dated clasts (see section 7.2).

7.3.3. 15015.

7.3.3.1. Glass subsample. The Ar release spectrum of glass 229b1 has relatively young, but concordant $^{40}\text{Ar}/^{39}\text{Ar}$ step ages in the initial 5 steps; then, a systematic increase in ages to concordant $^{40}\text{Ar}/^{39}\text{Ar}$ ages is observed in the 14 highest temperature steps (fig. S33). Corrections to the $^{40}\text{Ar}/^{39}\text{Ar}$ step ages for the trapped ^{40}Ar using the intercept $^{40}\text{Ar}/^{36}\text{Ar}$ value (1.09 ± 0.03) shown in fig. S37 were ~40-80% for glass 229b1. From the corrected ages, weighted means are 492 ± 8 Ma, calculated from the initial 5 steps, and 1723 ± 105 Ma, calculated from the

Table S16. $^{40}\text{Ar}/^{39}\text{Ar}$ degassing data for 15465 glass 6-4-1

COMPLETE $^{40}\text{Ar}/^{39}\text{Ar}$ INCREMENTAL HEATING RESULTS

#	Temp (°C)	^{40}Ar ± 1σ	^{39}Ar ± 1σ	^{38}Ar ± 1σ	^{37}Ar ± 1σ	^{36}Ar ± 1σ	$^{40}\text{Ar}^*$ (%)	$^{39}\text{Ar}_k$ (%)	$^{38}\text{Ar}_{\text{cos}}$ (%)	$^{38}\text{Ar}_{\text{trap}}$ (%)	$^{36}\text{Ar}_{\text{cos}}$ (%)	$^{36}\text{Ar}_{\text{trap}}$ (%)	Ca/K	$^{40}\text{Ar}/^{39}\text{Ar}$ Age ± 1σ (Ma)	Apparent ^{38}Ar Exposure Age ± 1σ (Ma)
1	450 °C	0.04 ± 0.01	0.002 ± 0.001	0.001 ± 0.0001	0.001 ± 0.000	0.006 ± 0.0004	86.2	100.0	n.d.	100.0	n.d.	100.0	0.6	434 ± 316	n.d. ± n.d.
2	450 °C	0.03 ± 0.01	0.002 ± 0.001	0.001 ± 0.0001	0.001 ± 0.000	0.004 ± 0.0004	89.6	100.0	39.7	58.2	7.7	92.3	0.6	292 ± 162	523 ± 667
3	500 °C	0.21 ± 0.01	0.008 ± 0.001	0.006 ± 0.0002	0.003 ± 0.000	0.026 ± 0.0006	89.3	100.0	10.4	87.9	1.4	98.6	0.7	487 ± 75	155 ± 76
4	500 °C	0.21 ± 0.01	0.013 ± 0.001	0.004 ± 0.0002	0.002 ± 0.000	0.019 ± 0.0005	92.1	100.0	17.2	79.2	2.6	97.4	0.3	317 ± 34	155 ± 57
5	550 °C	0.81 ± 0.01	0.036 ± 0.002	0.023 ± 0.0003	0.015 ± 0.000	0.104 ± 0.0009	89.0	100.0	16.2	82.0	2.4	97.6	0.8	424 ± 38	219 ± 30
6	550 °C	0.38 ± 0.01	0.013 ± 0.002	0.014 ± 0.0002	0.008 ± 0.000	0.060 ± 0.0008	86.5	100.0	17.8	81.1	2.6	97.4	1.3	523 ± 76	329 ± 91
7	600 °C	0.84 ± 0.01	0.030 ± 0.001	0.039 ± 0.0004	0.023 ± 0.000	0.179 ± 0.0013	81.6	99.9	13.5	85.6	1.9	98.1	1.5	470 ± 70	276 ± 39
8	601 °C	0.47 ± 0.01	0.020 ± 0.001	0.023 ± 0.0003	0.015 ± 0.000	0.099 ± 0.0011	82.1	100.0	18.1	80.8	2.7	97.3	1.4	403 ± 62	331 ± 56
9	650 °C	1.28 ± 0.01	0.046 ± 0.002	0.079 ± 0.0004	0.036 ± 0.000	0.354 ± 0.0019	76.2	99.9	16.0	83.3	2.3	97.7	1.5	445 ± 90	436 ± 45
10	651 °C	0.72 ± 0.01	0.030 ± 0.002	0.044 ± 0.0004	0.024 ± 0.000	0.197 ± 0.0012	76.4	99.9	15.7	83.5	2.3	97.7	1.6	393 ± 81	366 ± 52
11	699 °C	2.34 ± 0.01	0.064 ± 0.002	0.127 ± 0.0006	0.054 ± 0.001	0.615 ± 0.0018	77.1	99.9	8.9	90.5	1.2	98.8	1.7	570 ± 105	272 ± 32
12	700 °C	0.85 ± 0.01	0.039 ± 0.002	0.053 ± 0.0005	0.034 ± 0.000	0.234 ± 0.0016	76.3	99.9	18.2	80.9	2.7	97.3	1.7	355 ± 73	374 ± 43
13	750 °C	1.67 ± 0.01	0.068 ± 0.001	0.128 ± 0.0005	0.065 ± 0.001	0.573 ± 0.0015	70.3	99.9	16.2	83.1	2.3	97.7	1.9	369 ± 101	436 ± 29
14	750 °C	1.12 ± 0.01	0.045 ± 0.001	0.056 ± 0.0004	0.041 ± 0.000	0.235 ± 0.0012	82.1	99.9	21.3	77.7	3.3	96.7	1.8	429 ± 61	386 ± 31
15	799 °C	1.93 ± 0.01	0.082 ± 0.002	0.098 ± 0.0005	0.077 ± 0.001	0.394 ± 0.0015	82.8	99.9	25.8	73.1	4.2	95.8	1.8	408 ± 55	445 ± 23
16	800 °C	1.07 ± 0.01	0.051 ± 0.001	0.041 ± 0.0005	0.046 ± 0.000	0.144 ± 0.0010	88.9	99.9	35.3	63.1	6.4	93.6	1.8	395 ± 33	417 ± 28
17	850 °C	1.98 ± 0.01	0.081 ± 0.002	0.074 ± 0.0005	0.071 ± 0.000	0.273 ± 0.0012	88.5	99.9	32.9	65.8	5.8	94.2	1.7	453 ± 38	453 ± 23
18	850 °C	1.52 ± 0.01	0.050 ± 0.001	0.064 ± 0.0005	0.045 ± 0.000	0.264 ± 0.0012	85.2	99.9	23.2	75.8	3.6	96.4	1.8	527 ± 58	434 ± 31
19	900 °C	2.06 ± 0.01	0.091 ± 0.001	0.078 ± 0.0004	0.084 ± 0.001	0.279 ± 0.0011	88.8	99.9	35.2	63.4	6.4	93.6	1.8	419 ± 34	440 ± 17
20	898 °C	1.50 ± 0.01	0.062 ± 0.002	0.055 ± 0.0005	0.056 ± 0.000	0.201 ± 0.0011	88.9	99.9	33.2	65.4	5.9	94.1	1.8	450 ± 38	436 ± 28
21	949 °C	2.22 ± 0.01	0.103 ± 0.002	0.090 ± 0.0005	0.101 ± 0.001	0.305 ± 0.0011	88.8	99.9	38.9	59.7	7.4	92.6	1.9	402 ± 34	477 ± 23
22	949 °C	1.27 ± 0.01	0.052 ± 0.001	0.045 ± 0.0005	0.049 ± 0.000	0.154 ± 0.0010	90.1	99.9	39.2	59.4	7.5	92.5	1.8	457 ± 34	494 ± 32
23	997 °C	2.34 ± 0.01	0.090 ± 0.002	0.088 ± 0.0005	0.098 ± 0.001	0.294 ± 0.0015	89.7	99.9	40.2	58.5	7.8	92.2	2.1	479 ± 36	522 ± 23
24	997 °C	1.56 ± 0.01	0.022 ± 0.001	0.031 ± 0.0003	0.025 ± 0.000	0.104 ± 0.0009	94.6	99.9	39.8	59.3	7.6	92.4	2.2	1136 ± 57	731 ± 80
25	1047 °C	6.86 ± 0.02	0.099 ± 0.002	0.173 ± 0.0007	0.119 ± 0.001	0.667 ± 0.0024	91.8	99.9	29.6	69.7	5.0	95.0	2.4	1097 ± 55	649 ± 31
26	1048 °C	7.00 ± 0.02	0.042 ± 0.002	0.125 ± 0.0006	0.033 ± 0.000	0.561 ± 0.0021	93.1	99.9	16.6	83.0	2.4	97.6	1.5	1996 ± 78	776 ± 70

Isotope abundances given in 10^{-15} mol (spectrometer sensitivity is $\sim 1.12 \times 10^{-14}$ mols/nA),
and corrected for ^{37}Ar and ^{39}Ar decay, half-lives of 35.2 days and 269 years, respectively,
and for spectrometer discrimination per atomic mass unit of 1.004535 ± 0.002968 .

Isotope sources calculated using the reactor constants in ref. (47),
assuming $(^{38}\text{Ar}/^{36}\text{Ar})_{\text{cos}} = 1.54$, $(^{38}\text{Ar}/^{36}\text{Ar})_{\text{trap}} = 0.188$, and $(^{40}\text{Ar}/^{36}\text{Ar})_{\text{trap}} = 0.88 \pm 0.63$.

No corrections were made for cosmogenic ^{40}Ar .

Ages calculated using the decay constants and standard calibration of ref. (46) and calculated relative to Hb3gr fluence monitor (1081 Ma).

Corrections were made for reactor produced ^{38}Ar and ^{36}Ar in age calculations.

J-Value is 0.013048 ± 0.000130 .

Average analytical blanks are: $^{40}\text{Ar} = 0.015$; $^{39}\text{Ar} = 0.0001$; $^{38}\text{Ar} = 0.00002$; $^{37}\text{Ar} = 0.0001$; $^{36}\text{Ar} = 0.00007$ (nanoamps).

Temperature was controlled with approximately ± 10 °C precision and ± 10 °C accuracy; each heating duration was 600 seconds.

The apparent ^{38}Ar exposure ages are calculated for ^{38}Ar production in K-glass and plagioclase solely from Ca, K, Fe and Ti; other sources are assumed to be negligible.

n.d. is not determined

Table S17. $^{40}\text{Ar}/^{39}\text{Ar}$ degassing data for 15465 clast 6-2

COMPLETE $^{40}\text{Ar}/^{39}\text{Ar}$ INCREMENTAL HEATING RESULTS

#	Temp (°C)	^{40}Ar ± 1σ	^{39}Ar ± 1σ	^{38}Ar ± 1σ	^{37}Ar ± 1σ	^{36}Ar ± 1σ	$^{40}\text{Ar}^*$ (%)	$^{39}\text{Ar}_k$ (%)	$^{38}\text{Ar}_{\text{cos}}$ (%)	$^{38}\text{Ar}_{\text{trap}}$ (%)	$^{36}\text{Ar}_{\text{cos}}$ (%)	$^{36}\text{Ar}_{\text{trap}}$ (%)	Ca/K	$^{40}\text{Ar}/^{39}\text{Ar}$ Age ± 1σ (Ma)	Apparent ^{38}Ar Exposure Age ± 1σ (Ma)
1	399 °C	0.30 ± 0.01	0.098 ± 0.002	0.005 ± 0.0002	0.007 ± 0.000	0.009 ± 0.0004	94.02	99.99	46.5	29.0	83.5	83.5	0.1	66 ± 2	66 ± 10
2	399 °C	0.28 ± 0.01	0.093 ± 0.002	0.004 ± 0.0002	0.007 ± 0.000	0.009 ± 0.0004	93.03	100.00	29.4	41.0	8.1	91.9	0.1	65 ± 2	35 ± 8
3	450 °C	1.86 ± 0.01	0.495 ± 0.003	0.031 ± 0.0003	0.065 ± 0.000	0.057 ± 0.0007	94.05	99.99	52.2	28.4	18.4	81.6	0.3	81 ± 1	88 ± 5
4	449 °C	1.63 ± 0.01	0.452 ± 0.003	0.026 ± 0.0004	0.055 ± 0.000	0.049 ± 0.0007	94.07	99.99	48.8	29.9	16.7	83.3	0.2	78 ± 1	76 ± 5
5	500 °C	7.08 ± 0.01	1.572 ± 0.005	0.117 ± 0.0008	0.267 ± 0.001	0.204 ± 0.0015	94.62	99.99	57.4	26.2	21.2	78.8	0.3	98 ± 1	110 ± 4
6	500 °C	5.55 ± 0.02	1.139 ± 0.004	0.077 ± 0.0005	0.160 ± 0.001	0.150 ± 0.0009	94.68	99.99	51.0	30.9	16.9	83.1	0.3	106 ± 2	91 ± 4
7	549 °C	30.67 ± 0.06	4.350 ± 0.017	0.385 ± 0.0010	0.788 ± 0.003	0.822 ± 0.0029	94.67	99.99	52.2	34.1	15.8	84.1	0.4	151 ± 2	118 ± 4
8	549 °C	22.77 ± 0.03	2.169 ± 0.006	0.224 ± 0.0009	0.358 ± 0.001	0.599 ± 0.0024	94.43	99.99	42.7	45.5	10.4	89.6	0.3	220 ± 3	114 ± 4
9	601 °C	58.18 ± 0.08	3.763 ± 0.011	0.597 ± 0.0016	0.926 ± 0.002	1.752 ± 0.0036	93.54	99.98	41.8	50.5	9.2	90.8	0.5	313 ± 5	159 ± 4
10	601 °C	47.47 ± 0.05	2.131 ± 0.008	0.459 ± 0.0012	0.516 ± 0.002	1.637 ± 0.0035	92.31	99.98	30.4	63.9	5.5	94.5	0.5	430 ± 7	157 ± 5
11	649 °C	98.82 ± 0.11	3.526 ± 0.013	1.161 ± 0.0019	1.076 ± 0.003	4.497 ± 0.0089	89.73	99.98	26.0	70.2	4.4	95.6	0.6	513 ± 11	194 ± 6
12	651 °C	77.80 ± 0.08	1.921 ± 0.005	0.964 ± 0.0017	0.556 ± 0.002	4.131 ± 0.0092	87.82	99.98	18.6	79.0	2.8	97.2	0.6	689 ± 16	215 ± 8
13	700 °C	161.04 ± 0.13	3.122 ± 0.011	2.622 ± 0.0044	1.129 ± 0.003	11.746 ± 0.0179	83.17	99.97	15.5	83.1	2.2	97.8	0.7	804 ± 25	280 ± 13
14	700 °C	138.36 ± 0.11	1.666 ± 0.007	2.371 ± 0.0041	0.606 ± 0.002	11.244 ± 0.0146	81.09	99.97	10.4	88.7	1.4	98.6	0.7	1140 ± 37	320 ± 22
15	750 °C	310.77 ± 0.34	2.537 ± 0.013	7.904 ± 0.0096	1.028 ± 0.003	38.273 ± 0.0549	71.28	99.97	8.8	90.8	1.2	98.8	0.8	1375 ± 72	573 ± 46
16	750 °C	281.66 ± 0.27	1.416 ± 0.010	7.261 ± 0.0076	0.508 ± 0.002	35.870 ± 0.0448	70.22	99.98	6.9	92.9	0.9	99.1	0.7	1876 ± 92	764 ± 80
17	799 °C	657.19 ± 0.48	2.135 ± 0.016	23.278 ± 0.0168	0.792 ± 0.002	116.368 ± 0.0997	58.52	99.97	5.8	94.1	0.7	99.3	0.7	2187 ± 166	1343 ± 167
18	800 °C	420.45 ± 0.35	1.034 ± 0.011	11.553 ± 0.0112	0.342 ± 0.001	57.471 ± 0.0672	68.01	99.98	6.3	93.6	0.8	99.2	0.6	2762 ± 124	1558 ± 180
19	850 °C	694.82 ± 0.85	1.396 ± 0.014	20.647 ± 0.0134	0.546 ± 0.002	101.896 ± 0.0683	65.72	99.97	7.2	92.7	0.9	99.1	0.8	3005 ± 142	2233 ± 222
20	849 °C	431.72 ± 0.24	0.765 ± 0.011	10.273 ± 0.0123	0.281 ± 0.002	50.786 ± 0.0616	72.49	99.97	7.0	92.9	0.9	99.1	0.7	3339 ± 110	2012 ± 215
21	900 °C	757.02 ± 0.64	1.206 ± 0.014	23.607 ± 0.0134	0.527 ± 0.002	118.306 ± 0.0739	63.38	99.97	5.6	94.4	0.7	99.3	0.9	3298 ± 163	2202 ± 286
22	900 °C	424.18 ± 0.27	0.622 ± 0.010	11.670 ± 0.0085	0.270 ± 0.001	58.156 ± 0.0549	67.90	99.97	6.2	93.8	0.8	99.2	0.9	3530 ± 138	2344 ± 281
23	949 °C	818.09 ± 0.93	1.143 ± 0.014	33.044 ± 0.0325	0.620 ± 0.002	166.115 ± 0.1792	52.40	99.96	5.2	94.7	0.7	99.3	1.1	3209 ± 252	2828 ± 395
24	949 °C	400.89 ± 0.26	0.505 ± 0.010	14.211 ± 0.0123	0.304 ± 0.002	71.576 ± 0.0582	58.14	99.96	5.0	94.9	0.6	99.4	1.2	3526 ± 208	2534 ± 376
25	998 °C	1161.12 ± 1.11	0.933 ± 0.016	63.001 ± 0.0448	0.861 ± 0.002	319.750 ± 0.2352	35.36	99.94	4.2	95.8	0.5	99.5	1.8	3452 ± 519	n.d. ± n.d.
26	998 °C	374.57 ± 0.26	0.369 ± 0.009	16.690 ± 0.0112	0.318 ± 0.002	83.199 ± 0.1053	48.00	99.94	6.2	93.8	0.8	99.2	1.7	3608 ± 314	n.d. ± n.d.
27	1048 °C	886.72 ± 0.99	0.777 ± 0.014	54.250 ± 0.0515	1.247 ± 0.007	266.868 ± 0.3808	29.68	99.89	7.6	92.4	1.0	99.0	3.1	3058 ± 643	n.d. ± n.d.
28	1047 °C	174.75 ± 0.17	0.241 ± 0.007	7.689 ± 0.0070	0.459 ± 0.002	34.132 ± 0.0437	55.11	99.87	18.0	82.0	2.6	97.4	3.7	3303 ± 232	n.d. ± n.d.
29	1186 °C	632.99 ± 0.41	0.868 ± 0.015	27.823 ± 0.0213	3.067 ± 0.018	114.370 ± 0.1232	59.04	99.75	25.1	74.9	3.9	96.1	6.9	3421 ± 198	n.d. ± n.d.
30	1199 °C	1.65 ± 0.03	0.007 ± 0.003	0.030 ± 0.0009	0.008 ± 0.000	0.080 ± 0.0016	90.06	99.91	55.1	44.7	13.1	86.8	2.5	2482 ± 200	n.d. ± n.d.

Isotope abundances given in 10^{-15} mol (spectrometer sensitivity is $\sim 1.12 \times 10^{-14}$ mols/nA),
and corrected for ^{37}Ar and ^{39}Ar decay, half-lives of 35.2 days and 269 years, respectively,
and for spectrometer discrimination per atomic mass unit of 1.004535 ± 0.002968 .

Isotope sources calculated using the reactor constants in ref. (47),
assuming $(^{38}\text{Ar}/^{36}\text{Ar})_{\text{cos}} = 1.54$, $(^{38}\text{Ar}/^{36}\text{Ar})_{\text{trap}} = 0.188$, and $(^{40}\text{Ar}/^{36}\text{Ar})_{\text{trap}} = 2.36 \pm 0.43$.

No corrections were made for cosmogenic ^{40}Ar .
Ages calculated using the decay constants and standard calibration of ref. (46) and calculated relative to Hb3gr fluence monitor (1081 Ma).

Corrections were made for reactor produced ^{38}Ar and ^{36}Ar in age calculations.
J-Value is 0.013048 ± 0.000130 .

Average analytical blanks are: $^{40}\text{Ar} = 0.015$; $^{39}\text{Ar} = 0.0001$; $^{38}\text{Ar} = 0.00002$; $^{37}\text{Ar} = 0.0001$; $^{36}\text{Ar} = 0.00007$ (nanoamps).
Temperature was controlled with approximately ± 10 °C precision and ± 10 °C accuracy; each heating duration was 600 seconds.
The apparent ^{38}Ar exposure ages are calculated for ^{38}Ar production in K-glass and plagioclase solely from Ca, K, Fe and Ti; other sources are assumed to be negligible.
n.d. is not determined

Table S18. $^{40}\text{Ar}/^{39}\text{Ar}$ degassing data for 15015 glass 229b1

COMPLETE $^{40}\text{Ar}/^{39}\text{Ar}$ INCREMENTAL HEATING RESULTS

#	Temp (°C)	^{40}Ar ± 1σ	^{39}Ar ± 1σ	^{38}Ar ± 1σ	^{37}Ar ± 1σ	^{36}Ar ± 1σ	$^{40}\text{Ar}^*$ (%)	$^{39}\text{Ar}_k$ (%)	$^{38}\text{Ar}_{\text{cos}}$ (%)	$^{38}\text{Ar}_{\text{trap}}$ (%)	$^{36}\text{Ar}_{\text{cos}}$ (%)	$^{36}\text{Ar}_{\text{trap}}$ (%)	Ca/K	$^{40}\text{Ar}/^{39}\text{Ar}$ Age ± 1σ (Ma)	$^{40}\text{Ar}/^{39}\text{Ar}$ Age* ± 1σ (Ma)
1	449 °C	1.30 ± 0.01	0.029 ± 0.002	0.109 ± 0.0006	0.005 ± 0.000	0.583 ± 0.0023	51.1	100.0	0.0	100.0	0.0	100.0	0.3	830 ± 38	471 ± 27
2	449 °C	1.32 ± 0.01	0.027 ± 0.002	0.108 ± 0.0007	0.005 ± 0.000	0.563 ± 0.0021	53.7	100.0	1.2	98.5	0.1	99.9	0.4	890 ± 48	532 ± 34
3	499 °C	6.15 ± 0.02	0.131 ± 0.002	0.558 ± 0.0017	0.030 ± 0.000	2.987 ± 0.0069	46.9	100.0	0.0	100.0	0.0	100.0	0.5	864 ± 14	457 ± 16
4	499 °C	5.15 ± 0.01	0.113 ± 0.002	0.434 ± 0.0009	0.020 ± 0.000	2.316 ± 0.0071	50.8	100.0	0.0	100.0	0.0	100.0	0.4	844 ± 15	478 ± 15
5	550 °C	25.44 ± 0.04	0.474 ± 0.003	2.218 ± 0.0029	0.090 ± 0.001	11.816 ± 0.0146	49.3	100.0	0.0	100.0	0.0	100.0	0.4	960 ± 9	536 ± 15
6	550 °C	19.67 ± 0.03	0.283 ± 0.003	1.584 ± 0.0022	0.040 ± 0.000	8.412 ± 0.0123	53.3	100.0	0.0	100.0	0.0	100.0	0.3	1168 ± 13	714 ± 17
7	600 °C	48.57 ± 0.06	0.471 ± 0.005	4.323 ± 0.0049	0.079 ± 0.001	22.838 ± 0.0202	48.7	100.0	0.0	100.0	0.0	100.0	0.3	1541 ± 15	912 ± 24
8	600 °C	42.19 ± 0.06	0.283 ± 0.003	3.687 ± 0.0055	0.040 ± 0.000	19.573 ± 0.0179	49.4	100.0	0.0	100.0	0.0	100.0	0.3	1955 ± 19	1219 ± 30
9	649 °C	138.00 ± 0.11	0.484 ± 0.008	16.688 ± 0.0134	0.098 ± 0.001	87.907 ± 0.0627	30.6	100.0	0.0	99.9	0.0	100.0	0.4	2805 ± 27	1373 ± 66
10	650 °C	118.48 ± 0.10	0.290 ± 0.006	14.912 ± 0.0123	0.060 ± 0.001	78.957 ± 0.0683	27.3	100.0	0.0	100.0	0.0	100.0	0.4	3338 ± 36	1625 ± 86
11	700 °C	421.60 ± 0.32	0.549 ± 0.010	68.680 ± 0.0549	0.188 ± 0.001	360.241 ± 0.6944	6.9	100.0	0.6	99.4	0.9	99.9	0.7	4340 ± 34	954 ± 289
12	701 °C	257.39 ± 0.17	0.298 ± 0.011	39.751 ± 0.0314	0.105 ± 0.001	209.353 ± 0.1568	11.4	100.0	0.1	99.9	0.1	100.0	0.7	4534 ± 64	1490 ± 233
13	750 °C	637.46 ± 0.56	0.438 ± 0.016	102.890 ± 0.0459	0.254 ± 0.001	539.570 ± 0.4928	7.8	100.0	0.6	99.4	0.8	99.9	1.1	5415 ± 65	1644 ± 371
14	750 °C	356.88 ± 0.20	0.256 ± 0.012	56.183 ± 0.0358	0.131 ± 0.001	294.609 ± 0.2688	10.1	100.0	0.6	99.4	0.6	99.9	1.0	5341 ± 80	1883 ± 307
15	801 °C	415.49 ± 0.31	0.288 ± 0.010	65.655 ± 0.0448	0.167 ± 0.001	345.124 ± 0.3584	9.5	100.0	0.3	99.7	0.3	100.0	1.1	5399 ± 63	1852 ± 323
16	800 °C	329.56 ± 0.24	0.229 ± 0.008	52.325 ± 0.0605	0.123 ± 0.001	274.065 ± 0.1792	9.4	100.0	0.7	99.3	0.8	99.9	1.1	5398 ± 64	1844 ± 324
17	850 °C	529.26 ± 0.63	0.367 ± 0.012	85.923 ± 0.0482	0.209 ± 0.001	449.946 ± 0.4704	7.4	100.0	0.7	99.2	1.1	99.9	1.1	5400 ± 57	1580 ± 382
18	849 °C	378.16 ± 0.31	0.255 ± 0.012	61.849 ± 0.0415	0.128 ± 0.001	325.493 ± 0.2240	6.2	100.0	0.2	99.8	0.3	100.0	1.0	5447 ± 80	1425 ± 434
19	900 °C	482.71 ± 0.39	0.306 ± 0.011	80.597 ± 0.0370	0.203 ± 0.001	422.710 ± 0.3472	4.6	100.0	0.6	99.4	1.4	99.9	1.3	5557 ± 66	1209 ± 528
20	900 °C	324.19 ± 0.28	0.219 ± 0.012	53.859 ± 0.0336	0.125 ± 0.001	282.975 ± 0.1904	4.9	100.0	0.4	99.6	0.8	100.0	1.1	5442 ± 93	1203 ± 496
21	949 °C	383.92 ± 0.37	0.268 ± 0.011	65.298 ± 0.0448	0.214 ± 0.001	338.184 ± 0.3360	4.2	99.9	2.0	98.0	5.5	99.8	1.6	5389 ± 72	1052 ± 525
22	949 °C	249.83 ± 0.16	0.198 ± 0.007	41.296 ± 0.0325	0.131 ± 0.001	215.495 ± 0.2016	6.1	100.0	1.1	98.9	2.0	99.9	1.3	5168 ± 61	1258 ± 404
23	998 °C	474.29 ± 0.39	0.348 ± 0.015	77.359 ± 0.0392	0.314 ± 0.002	399.234 ± 0.2800	8.5	99.9	2.4	97.6	3.1	99.7	1.8	5302 ± 74	1668 ± 342
24	998 °C	253.72 ± 0.17	0.170 ± 0.011	40.281 ± 0.0314	0.158 ± 0.001	208.128 ± 0.1344	10.8	99.9	2.3	97.7	2.2	99.7	1.8	5457 ± 115	2051 ± 303
25	1021 °C	525.21 ± 0.46	0.239 ± 0.016	85.256 ± 0.0616	0.296 ± 0.002	439.707 ± 0.5376	9.0	99.9	2.5	97.5	3.0	99.7	2.4	6134 ± 118	2313 ± 391
26	1032 °C	419.12 ± 0.39	0.254 ± 0.009	68.078 ± 0.0280	0.216 ± 0.001	352.533 ± 0.2912	8.5	99.9	2.0	98.0	2.5	99.7	1.7	5636 ± 61	1890 ± 365

Isotope abundances given in 10^{-15} mol (spectrometer sensitivity is $\sim 1.12 \times 10^{-14}$ mols/nA),
and corrected for ^{37}Ar and ^{39}Ar decay, half-lives of 35.2 days and 269 years, respectively,
and for spectrometer discrimination per atomic mass unit of 1.004535 ± 0.002968 .

Isotope sources calculated using the reactor constants in ref. (47),
assuming $(^{38}\text{Ar}/^{36}\text{Ar})_{\text{cos}} = 1.54$, $(^{38}\text{Ar}/^{36}\text{Ar})_{\text{trap}} = 0.188$, and $(^{40}\text{Ar}/^{36}\text{Ar})_{\text{trap}} = 0$.

No corrections were made for cosmogenic ^{40}Ar .
Ages calculated using the decay constants and standard calibration of ref. (46) and calculated relative to Hb3gr fluence monitor (1081 Ma).
Corrections were made for reactor produced ^{38}Ar and ^{36}Ar in age calculations.

J-Value is 0.013048 ± 0.000130 .

Average analytical blanks are: $^{40}\text{Ar} = 0.015$; $^{39}\text{Ar} = 0.0001$; $^{38}\text{Ar} = 0.00002$; $^{37}\text{Ar} = 0.0001$; $^{36}\text{Ar} = 0.00007$ (nanoamps).

Temperature was controlled with approximately ± 10 °C precision and ± 10 °C accuracy; each heating duration was 600 seconds.

*Ages calculated assuming a trapped $^{40}\text{Ar}/^{40}\text{Ar} = 1.09 \pm 0.03$

n.d. is not determined

Table S19. $^{40}\text{Ar}/^{39}\text{Ar}$ degassing data for 15015 clast 229a1a.

COMPLETE $^{40}\text{Ar}/^{39}\text{Ar}$ INCREMENTAL HEATING RESULTS

#	Temp (°C)	^{40}Ar ± 1σ	^{39}Ar ± 1σ	^{38}Ar ± 1σ	^{37}Ar ± 1σ	^{36}Ar ± 1σ	$^{40}\text{Ar}^*$ (%)	$^{39}\text{Ar}_k$ (%)	$^{38}\text{Ar}_{\text{cos}}$ (%)	$^{38}\text{Ar}_{\text{trap}}$ (%)	$^{36}\text{Ar}_{\text{cos}}$ (%)	$^{36}\text{Ar}_{\text{trap}}$ (%)	Ca/K	$^{40}\text{Ar}/^{39}\text{Ar}$ Age ± 1σ (Ma)	Apparent ^{38}Ar Exposure Age ± 1σ (Ma)
1	399 °C	2.32 ± 0.01	0.076 ± 0.001	0.004 ± 0.0002	0.006 ± 0.000	0.001 ± 0.0003	100.00	99.99	77.7	n.d.	n.d.	n.d.	0.2	606 ± 12	108 ± 12
2	399 °C	2.20 ± 0.01	0.072 ± 0.001	0.003 ± 0.0002	0.006 ± 0.000	0.002 ± 0.0003	100.00	99.99	69.3	4.4	66.0	34.0	0.2	609 ± 12	92 ± 12
3	449 °C	10.38 ± 0.02	0.387 ± 0.003	0.020 ± 0.0003	0.051 ± 0.000	0.012 ± 0.0004	100.00	99.99	73.6	2.2	80.1	19.8	0.3	542 ± 6	100 ± 5
4	449 °C	9.81 ± 0.02	0.356 ± 0.002	0.017 ± 0.0003	0.046 ± 0.000	0.011 ± 0.0004	100.00	99.99	70.9	3.8	69.7	30.2	0.3	555 ± 6	92 ± 5
5	500 °C	33.63 ± 0.05	1.322 ± 0.006	0.067 ± 0.0005	0.234 ± 0.001	0.042 ± 0.0007	100.00	99.99	73.4	2.7	76.7	23.1	0.3	518 ± 5	96 ± 4
6	500 °C	28.72 ± 0.05	0.956 ± 0.004	0.051 ± 0.0004	0.153 ± 0.001	0.031 ± 0.0006	100.00	99.99	75.2	2.2	80.8	19.0	0.3	598 ± 6	106 ± 4
7	550 °C	121.32 ± 0.09	3.263 ± 0.010	0.235 ± 0.0009	0.738 ± 0.002	0.161 ± 0.0011	100.00	99.98	79.9	3.1	75.7	24.2	0.4	715 ± 6	141 ± 4
8	550 °C	86.55 ± 0.07	1.451 ± 0.006	0.158 ± 0.0008	0.359 ± 0.002	0.111 ± 0.0011	100.00	99.98	86.1	2.8	79.3	20.6	0.5	1041 ± 9	226 ± 5
9	600 °C	165.63 ± 0.12	2.091 ± 0.011	0.434 ± 0.0013	0.767 ± 0.003	0.306 ± 0.0015	100.00	99.97	92.1	2.1	84.6	15.4	0.7	1284 ± 10	415 ± 7
10	600 °C	119.43 ± 0.10	0.955 ± 0.005	0.331 ± 0.0010	0.350 ± 0.002	0.232 ± 0.0012	100.00	99.97	94.8	1.7	87.5	12.4	0.7	1750 ± 13	714 ± 13
11	650 °C	238.43 ± 0.16	1.362 ± 0.008	1.063 ± 0.0021	0.654 ± 0.003	0.730 ± 0.0025	100.00	99.97	97.4	1.1	91.9	8.1	0.9	2150 ± 15	1508 ± 25
12	649 °C	164.33 ± 0.11	0.631 ± 0.005	0.751 ± 0.0015	0.306 ± 0.001	0.515 ± 0.0024	100.00	99.97	98.0	1.0	92.5	7.5	1.0	2679 ± 17	2304 ± 40
13	700 °C	327.98 ± 0.16	1.047 ± 0.007	2.089 ± 0.0029	0.626 ± 0.004	1.411 ± 0.0036	100.00	99.96	98.7	0.7	94.7	5.3	1.2	2942 ± 18	3588 ± 69
14	701 °C	198.73 ± 0.17	0.479 ± 0.004	1.197 ± 0.0019	0.311 ± 0.002	0.798 ± 0.0024	100.00	99.95	99.0	0.5	96.2	3.8	1.3	3361 ± 20	n.d. ± n.d.
15	750 °C	364.69 ± 0.30	0.846 ± 0.006	2.624 ± 0.0034	0.634 ± 0.001	1.768 ± 0.0046	100.00	99.95	99.0	0.6	95.1	4.9	1.5	3420 ± 19	n.d. ± n.d.
16	750 °C	221.27 ± 0.11	0.465 ± 0.004	1.506 ± 0.0022	0.363 ± 0.002	0.994 ± 0.0027	100.00	99.95	99.3	0.3	97.5	2.5	1.5	3571 ± 20	n.d. ± n.d.
17	800 °C	390.14 ± 0.24	0.827 ± 0.007	2.807 ± 0.0053	0.663 ± 0.003	1.880 ± 0.0037	100.00	99.94	99.1	0.5	95.9	4.1	1.6	3560 ± 20	n.d. ± n.d.
18	799 °C	185.30 ± 0.16	0.367 ± 0.005	1.293 ± 0.0018	0.310 ± 0.002	0.864 ± 0.0026	100.00	99.94	99.2	0.5	96.1	3.9	1.7	3664 ± 26	n.d. ± n.d.
19	850 °C	224.78 ± 0.13	0.458 ± 0.004	1.785 ± 0.0031	0.424 ± 0.002	1.196 ± 0.0033	100.00	99.94	99.2	0.5	95.9	4.1	1.8	3621 ± 22	n.d. ± n.d.
20	849 °C	95.58 ± 0.07	0.198 ± 0.004	0.735 ± 0.0014	0.172 ± 0.001	0.503 ± 0.0018	100.00	99.94	98.8	0.8	93.5	6.4	1.7	3598 ± 34	n.d. ± n.d.
21	899 °C	122.30 ± 0.10	0.306 ± 0.006	1.154 ± 0.0021	0.266 ± 0.002	0.832 ± 0.0024	100.00	99.94	98.1	1.6	88.2	11.8	1.7	3305 ± 33	n.d. ± n.d.
22	900 °C	54.67 ± 0.07	0.147 ± 0.003	0.534 ± 0.0014	0.122 ± 0.001	0.386 ± 0.0017	100.00	99.94	98.0	1.7	87.6	12.3	1.6	3195 ± 33	n.d. ± n.d.
23	948 °C	94.30 ± 0.08	0.299 ± 0.004	1.159 ± 0.0020	0.261 ± 0.001	0.858 ± 0.0028	100.00	99.94	97.7	2.0	85.5	14.5	1.7	2954 ± 24	n.d. ± n.d.
24	949 °C	43.45 ± 0.06	0.149 ± 0.002	0.565 ± 0.0016	0.127 ± 0.001	0.414 ± 0.0017	100.00	99.94	97.8	1.9	86.4	13.6	1.7	2841 ± 26	n.d. ± n.d.
25	998 °C	90.55 ± 0.09	0.383 ± 0.004	1.510 ± 0.0020	0.338 ± 0.001	1.093 ± 0.0026	100.00	99.94	98.0	1.7	87.7	12.3	1.7	2547 ± 19	n.d. ± n.d.
26	997 °C	42.57 ± 0.06	0.183 ± 0.003	0.782 ± 0.0019	0.174 ± 0.001	0.551 ± 0.0023	100.00	99.93	98.4	1.3	90.5	9.5	1.9	2520 ± 23	n.d. ± n.d.
27	1047 °C	110.33 ± 0.11	0.519 ± 0.004	3.059 ± 0.0054	0.673 ± 0.002	2.072 ± 0.0043	100.00	99.91	99.1	0.7	94.8	5.2	2.5	2403 ± 18	n.d. ± n.d.
28	1048 °C	34.49 ± 0.07	0.142 ± 0.002	1.011 ± 0.0016	0.222 ± 0.001	0.690 ± 0.0020	100.00	99.89	99.1	0.8	94.1	5.9	3.1	2586 ± 27	n.d. ± n.d.
29	1125 °C	217.81 ± 0.25	0.806 ± 0.005	10.307 ± 0.0093	2.121 ± 0.006	7.144 ± 0.0123	100.00	99.82	98.9	1.0	92.4	7.6	5.2	2733 ± 17	n.d. ± n.d.
30	1123 °C	29.40 ± 0.05	0.100 ± 0.003	1.265 ± 0.0022	0.264 ± 0.002	0.867 ± 0.0029	100.00	99.82	99.1	0.8	93.6	6.4	5.2	2853 ± 200	n.d. ± n.d.

Isotope abundances given in 10^{-15} mol (spectrometer sensitivity is $\sim 1.12 \times 10^{-14}$ mols/nA),
and corrected for ^{37}Ar and ^{39}Ar decay, half-lives of 35.2 days and 269 years, respectively,
and for spectrometer discrimination per atomic mass unit of 1.004535 ± 0.002968 .

Isotope sources calculated using the reactor constants in ref. (47),
assuming $(^{38}\text{Ar}/^{36}\text{Ar})_{\text{cos}} = 1.54$, $(^{38}\text{Ar}/^{36}\text{Ar})_{\text{trap}} = 0.188$, and $(^{40}\text{Ar}/^{36}\text{Ar})_{\text{trap}} = 0$.

No corrections were made for cosmogenic ^{40}Ar .

Ages calculated using the decay constants and standard calibration of ref. (46) and calculated relative to Hb3gr fluence monitor (1081 Ma).

Corrections were made for reactor produced ^{38}Ar and ^{36}Ar in age calculations.

J-Value is 0.013048 ± 0.000130 .

Average analytical blanks are: $^{40}\text{Ar} = 0.015$; $^{39}\text{Ar} = 0.0001$; $^{38}\text{Ar} = 0.00002$; $^{37}\text{Ar} = 0.0001$; $^{36}\text{Ar} = 0.00007$ (nanoamps).

Temperature was controlled with approximately ± 10 °C precision and ± 10 °C accuracy; each heating duration was 600 seconds.

The apparent ^{38}Ar exposure ages are calculated for ^{38}Ar production in K-glass and plagioclase solely from Ca, K, Fe and Ti; other sources are assumed to be negligible.

n.d. is not determined

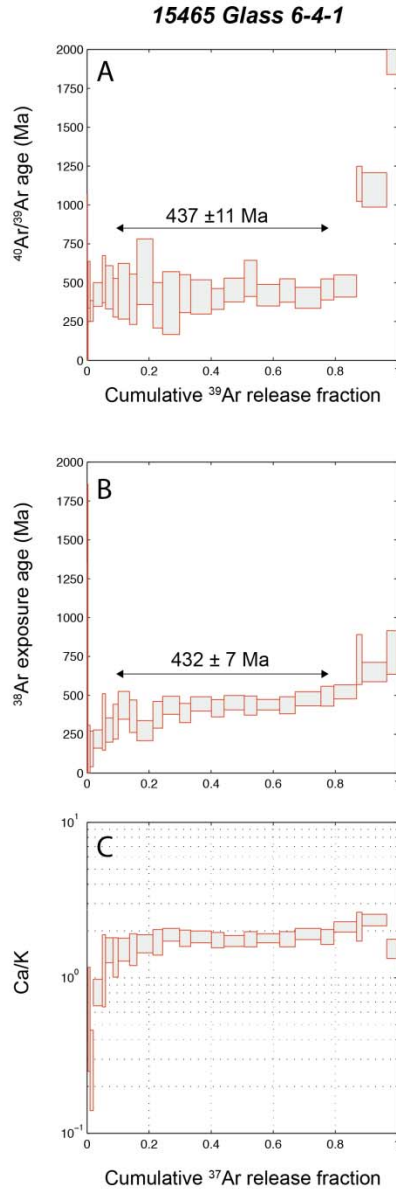


Fig. S31. Ar release spectra for 15465 glass subsample 6-4-1. (A) Apparent $^{40}\text{Ar}/^{39}\text{Ar}$ age. (B) Apparent cosmogenic ^{38}Ar exposure age. (C) Ca/K spectra. The $^{40}\text{Ar}/^{39}\text{Ar}$ age spectrum is plotted against the cumulative release fraction of ^{39}Ar , and the other two spectra against ^{37}Ar . Dimensions of boxes indicate $\pm 1\text{-}\sigma$ (vertical) and the fraction of ^{39}Ar or ^{37}Ar released (horizontal). The $^{40}\text{Ar}/^{39}\text{Ar}$ step ages were calculated assuming a trapped component with the $^{40}\text{Ar}/^{36}\text{Ar}$ ratio determined from the 3-isotope plot (fig. S35). Ca/K ratios were calculated from the $^{37}\text{Ar}_{\text{Ca}}/^{39}\text{Ar}_{\text{K}}$ ratio assuming that the relative production ratio for Ca to K is 1:1.96. Shifts in this apparent ratio help distinguish between the dominant source phases of Ar during thermal extractions.

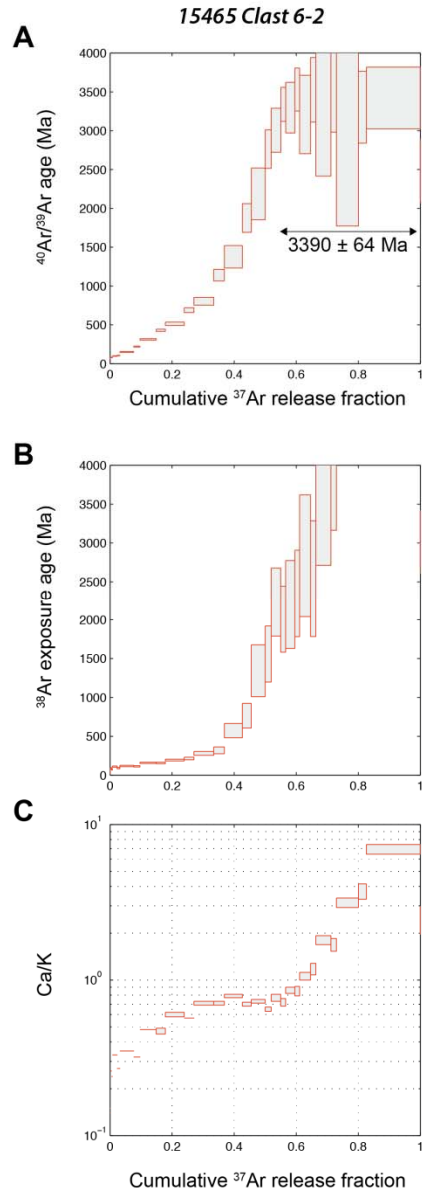


Fig. S32. Ar release spectra for 15465 clast subsample 6-2. (A) Apparent $^{40}\text{Ar}/^{39}\text{Ar}$ age. **(B)** Apparent cosmogenic ^{38}Ar exposure age. **(C)** Ca/K spectra. The three spectra are plotted against the cumulative release fraction of ^{37}Ar . Dimensions of boxes indicate $\pm 1\text{-}\sigma$ (vertical) and the fraction of ^{39}Ar or ^{37}Ar released (horizontal). The $^{40}\text{Ar}/^{39}\text{Ar}$ step ages were calculated assuming a trapped component with the $^{40}\text{Ar}/^{36}\text{Ar}$ ratio determined from the 3-isotope plot (fig. S36). Ca/K ratios were calculated from the $^{37}\text{Ar}_{\text{Ca}}/^{39}\text{Ar}_{\text{K}}$ ratio assuming that the relative production ratio for Ca to K is 1:1.96. Shifts in this apparent ratio help distinguish between dominant source phases of Ar during thermal extractions.

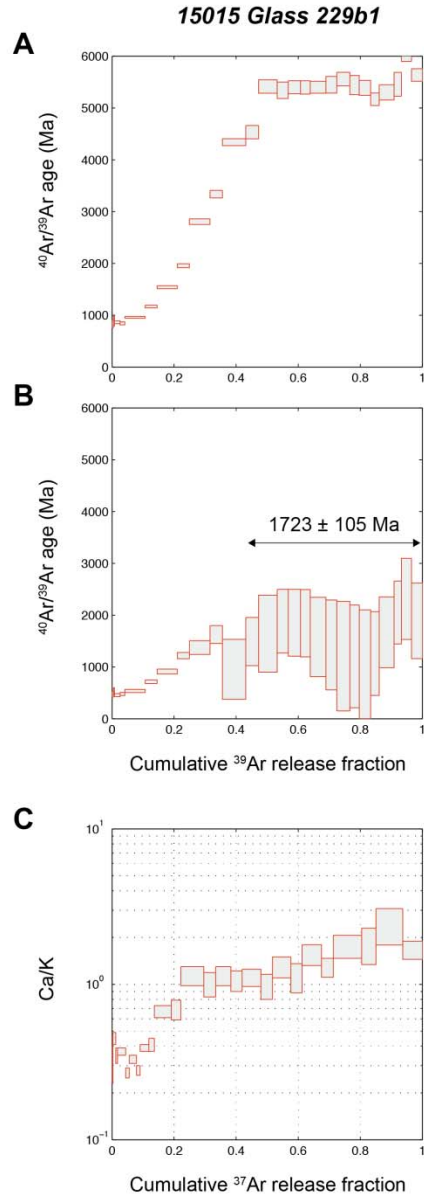


Fig. S33. Ar release spectra for 15015 glass subsample 229b1. (A) Apparent $^{40}\text{Ar}/^{39}\text{Ar}$ age assuming no trapped Ar component. (B) Apparent $^{40}\text{Ar}/^{39}\text{Ar}$ age assuming a trapped Ar component. (C) Ca/K spectra. The $^{40}\text{Ar}/^{39}\text{Ar}$ age spectra are plotted against the cumulative release fraction of ^{39}Ar , and Ca/K spectrum against ^{37}Ar . Dimensions of boxes indicate $\pm 1\text{-}\sigma$ (vertical) and the fraction of ^{39}Ar or ^{37}Ar released (horizontal). The $^{40}\text{Ar}/^{39}\text{Ar}$ step ages in panel B were calculated assuming a trapped component with the $^{40}\text{Ar}/^{36}\text{Ar}$ ratio determined from the 3-isotope plot (fig. S37). Ca/K ratios were calculated from the $^{37}\text{Ar}_{\text{Ca}}/^{39}\text{Ar}_{\text{K}}$ ratio assuming that the relative production ratio for Ca to K is 1:1.96. Shifts in this apparent ratio help distinguish between dominant source phases of Ar during thermal extractions.

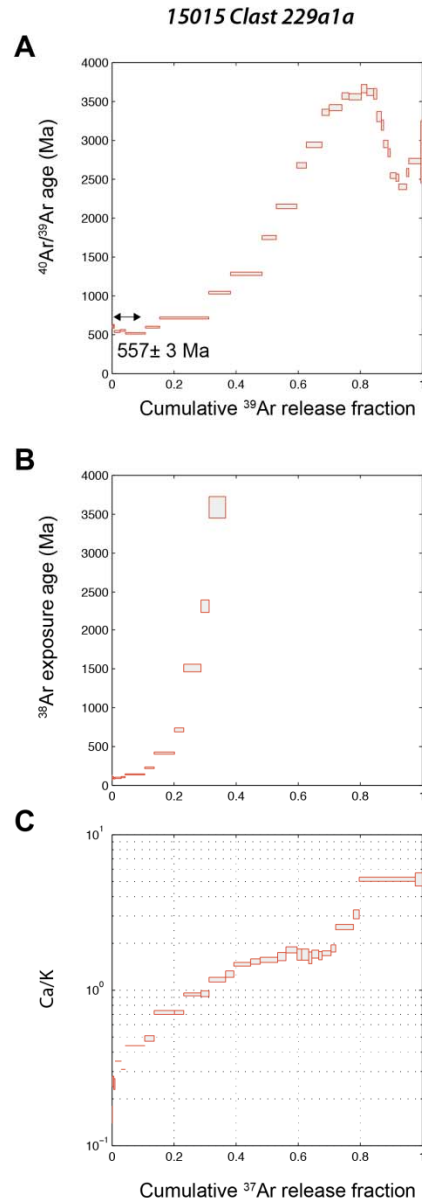


Fig. S34. Ar release spectra for 15015 clast subsample 229a1a. (A) Apparent $^{40}\text{Ar}/^{39}\text{Ar}$ age. (B) Apparent cosmogenic ^{38}Ar exposure age. (C) Ca/K spectra. The $^{40}\text{Ar}/^{39}\text{Ar}$ age spectrum is plotted against the cumulative release fraction of ^{39}Ar , and the other two spectra against ^{37}Ar . Dimensions of boxes indicate $\pm 1\text{-}\sigma$ (vertical) and the fraction of ^{39}Ar or ^{37}Ar released (horizontal). The $^{40}\text{Ar}/^{39}\text{Ar}$ step ages were calculated assuming no significant trapped Ar. Ca/K ratios were calculated from the $^{37}\text{Ar}_{\text{Ca}}/^{39}\text{Ar}_{\text{K}}$ ratio assuming that the relative production ratio for Ca to K is 1:1.96. Shifts in this apparent ratio help distinguish between dominant source phases of Ar during thermal extractions.

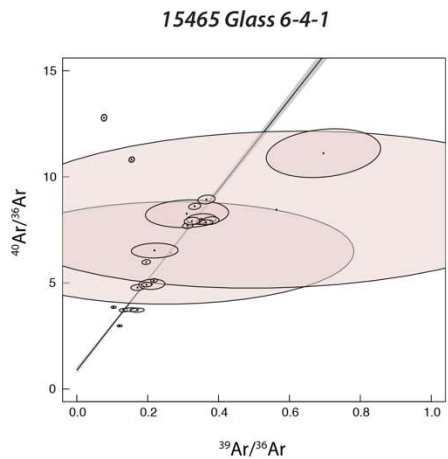


Fig. S35. Ar three-isotope plot for 15465 glass subsample 6-4-1. The figure shows the observed $^{40}\text{Ar}/^{36}\text{Ar}$ and $^{39}\text{Ar}/^{36}\text{Ar}$ ratios for each heating step. Error ellipses were calculated using IsoplotR (99). The line is a maximum likelihood error-weighted regression; points shown in grey were excluded from the regression. Although over-dispersed, these data yield an intercept of $^{40}\text{Ar}/^{36}\text{Ar} = 0.88 \pm 0.63$.

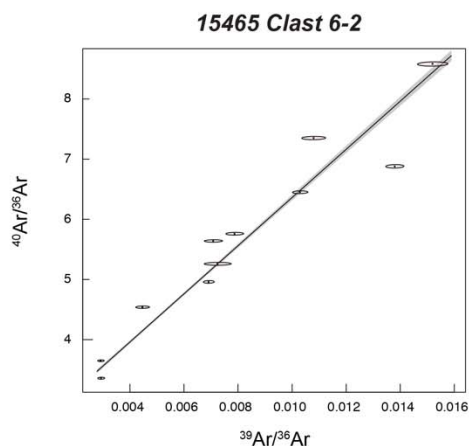


Fig. S36. Ar three-isotope plot for 15465 clast subsample 6-2. The figure shows the observed $^{40}\text{Ar}/^{36}\text{Ar}$ and $^{39}\text{Ar}/^{36}\text{Ar}$ ratios for each heating step. Error ellipses were calculated using IsoplotR (99). The line is a maximum likelihood error-weighted regression to the 11 highest-temperature steps. Though over-dispersed, these data yield an intercept of $^{40}\text{Ar}/^{36}\text{Ar} = 2.36 \pm 0.43$.

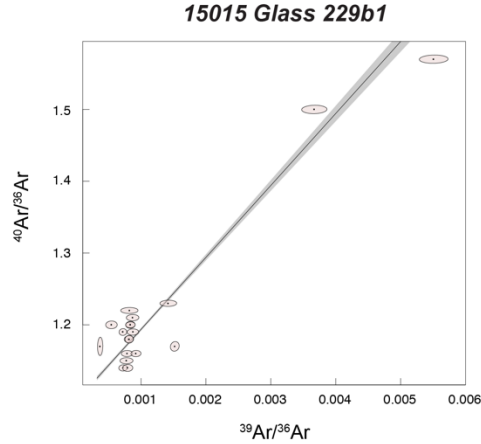


Fig. S37. Ar three-isotope for 15015 glass subsample 229b1. The figure shows the observed $^{40}\text{Ar}/^{36}\text{Ar}$ and $^{39}\text{Ar}/^{36}\text{Ar}$ ratios for each heating step. Error ellipses were calculated using IsoplotR (99). The line is a maximum likelihood error-weighted regression to the 17 highest-temperature steps. Though over-dispersed, these data yield an intercept of $^{40}\text{Ar}/^{36}\text{Ar} = 1.09 \pm 0.03$.

14 highest temperature steps. Due to the possibility that the glass was subsequently partially degassed by solar heating, we interpret the glass formation timing to be between 0.5-1.7 Ga. This age is consistent with the more precise age of 820 ± 30 Ma implied by the trapped $^{40}\text{Ar}/^{36}\text{Ar}$ component in the 15015 glass [age was estimated using the calibration of ref. (95)].

7.3.3.2. Clast subsample. The Ar release spectrum of clast sample 229a1a has systematically increasing apparent $^{40}\text{Ar}/^{39}\text{Ar}$ ages and cosmogenic ^{38}Ar exposure ages throughout the initial ~80% of released gas (fig. S34). For the reasons discussed above, we do not apply a correction for trapped Ar in this sample. The $^{40}\text{Ar}/^{39}\text{Ar}$ step ages range from ~500 Ma to ~3600 Ma, whereas the cosmogenic ^{38}Ar exposure ages systematically increase from ~100 Ma up to unreasonably high apparent values. The error-weighted mean calculated from the initial 6 concordant heating steps (amounting to the initial 15% of gas released) yields an apparent $^{40}\text{Ar}/^{39}\text{Ar}$ age of 557 ± 3 Ma, which we interpret to approximately constrain the timing of a clast reheating event.

7.4. Synthesis of 15465 and 15015 age data. Combining the existing geologic, petrographic, and geochemical studies with the previously published Ar data (section 7.2) as well as our new measurements (section 7.3) enables us to determine the timing of our paleointensity constraints from the matrix glasses of breccias 15465 and 15015. Given the igneous origin of matrix glass and evidence for subsequent shock processing, the null field magnetic records must date back to the time when the samples cooled through their maximum critical magnetization acquisition temperatures (i.e., 780 °C, the Curie point of kamacite; see main text). As discussed in section 2.2, this would have occurred when the breccias were assembled and welded together by the neo-formed matrix melt glass (62-64). Textural data and experimental formation of artificial regolith breccias by impact experiments on lunar soils indicate that the time at which the breccias were assembled and the formation of the matrix glass were synchronous.

An extreme upper limit on the time of the breccia assembly event is given by the youngest crystallization age for clasts in the samples. The presence of mare basalt clasts in 15015 (57) and

15465 (21, 56) and the close similarity between the composition of these breccias and soils near their sampling sites (20, 57) indicate they contain Apollo 15-like mare basalt clasts, meaning that the breccias were certainly assembled after the period of volcanic activity (i.e., <3.3 Ga) (96). For 15465, the remarkable agreement between the $^{40}\text{Ar}/^{39}\text{Ar}$ plateau age, trapped $^{40}\text{Ar}/^{36}\text{Ar}$ age, and CRE age for the matrix glass (fig. S38, grey rows in table S20) strongly supports its formation and the assembly of the breccia at a weighted mean age of 0.44 ± 0.01 Ga. For 15015, the $^{40}\text{Ar}/^{39}\text{Ar}$ ages measured as a part of this study and by ref. (57) and trapped $^{40}\text{Ar}/^{36}\text{Ar}$ ages of the matrix glass (fig. S39, table S21) consistently indicate that it formed and recorded magnetic field conditions sometime between 0.5 and 1.7 Ga. For the best-defined four 15015 glass dates ($^{40}\text{Ar}/^{39}\text{Ar}$ and trapped $^{40}\text{Ar}/^{36}\text{Ar}$) (grey rows in table S21), the weighted mean age is 0.91 ± 0.11 Ga (calculated following the same procedure as other trapped $^{40}\text{Ar}/^{36}\text{Ar}$ ages above). In conclusion, our best estimate of the age of NRM records from the time of breccia formation are 0.44 ± 0.01 and 0.91 ± 0.11 for 15465 and 15015, respectively.

7.5. The age of NRM in breccia 15498. The youngest known robust record of the lunar dynamo is currently the $\sim 5 \pm 2$ μT paleointensity value from the glassy matrix in regolith breccia 15498 (9). An extreme upper limit on the age of NRM in 15498 is provided by the 3.3 Ga $^{40}\text{Ar}/^{39}\text{Ar}$ age of Apollo 15-like mare basalt clasts in the sample (9). Furthermore, trapped $^{40}\text{Ar}/^{36}\text{Ar}$ analyses of 15498 (40) suggest a matrix glass formation age of $1.32^{+0.59}_{-0.52}$ Ga, where again the uncertainties take into account both those associated with the measured trapped $^{40}\text{Ar}/^{36}\text{Ar}$ value and the parameters in equation (S15). A caveat with the latter is again that the contribution of the in-situ-produced radiogenic ^{40}Ar was not reported and the sample lithology was not reported (22).

Recently reported $^{40}\text{Ar}/^{39}\text{Ar}$ analyses of a ~ 3.3 Ga mare basalt clast in 15498 indicate that a major thermal disturbance to $\sim 450\text{--}675$ $^{\circ}\text{C}$ occurred between 1.75 ± 0.75 Ga (9). In particular, modeling of the $^{40}\text{Ar}/^{39}\text{Ar}$ age spectrum without the first release step yielded a best-fit disturbance age of 1.0 Ga, while including this step yielded a best-fit disturbance age of 2.5 Ga (9). Omission of the first step is supported by two reasons: (a) it is the step most likely to be influenced by subsequent diffusive loss from the uncertain effects of daytime-heating on the lunar surface over the last <600 My and (b) the resulting inferred lithification age is within error of the sample's $1.32^{+0.59}_{-0.52}$ Ga trapped $^{40}\text{Ar}/^{36}\text{Ar}$ lithification age (40).

To obtain the best estimate of the age of 15498, we take the mean of the $^{40}\text{Ar}/^{39}\text{Ar}$ age of 1.75 ± 0.75 Ga and $1.32^{+0.59}_{-0.52}$ trapped $^{40}\text{Ar}/^{36}\text{Ar}$ ages weighted by the inverse square of their uncertainties. This yields an age of 1.47 ± 0.45 Ga (± 1 standard deviation).

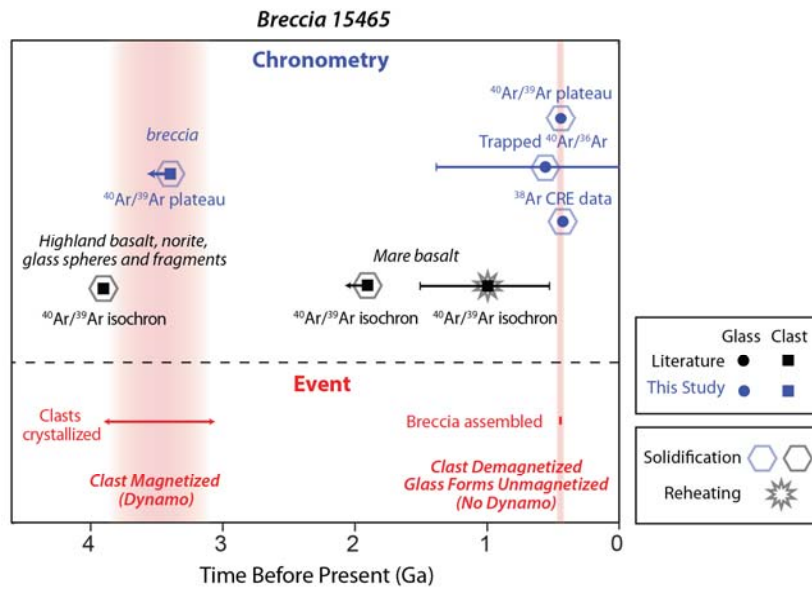


Fig. S38. Geologic and magnetization history of breccia 15465. Top panel shows the various $^{40}\text{Ar}/^{39}\text{Ar}$, $^{38}\text{Ar}/^{37}\text{Ar}$, and $^{40}\text{Ar}/^{36}\text{Ar}$ chronometry constraints from previous studies (black) and this study (blue). Circles and squares denote ages of matrix glass and clast samples, respectively. Lithologies of clasts are labeled next to each point. Points surrounded by pentagons are interpreted to be primary solidification ages while points surrounded by stars are inferred to be reheating ages. See table S20 for data sources and details. Bottom panel shows inferred geologic events and associated formation and remagnetization times of magnetic records in clasts and the matrix glass.

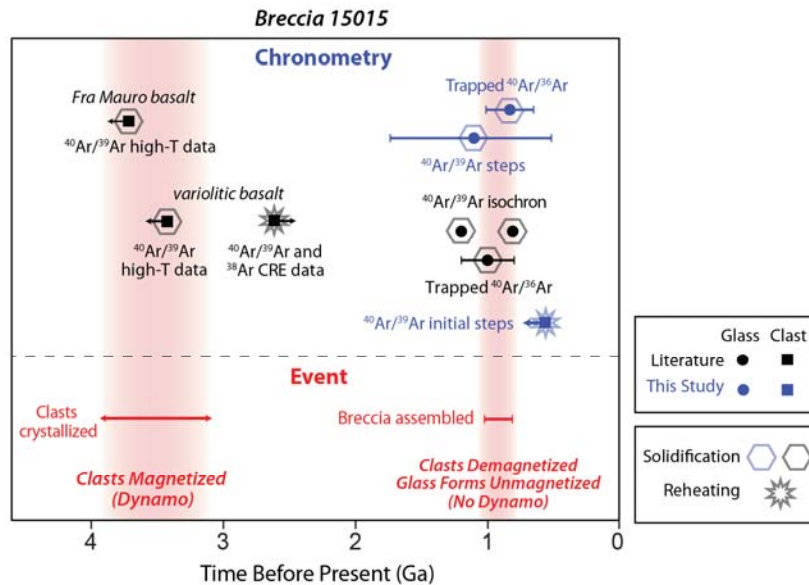


Fig. S39. Geologic and magnetization history of breccia 15015. Top panel shows the various $^{40}\text{Ar}/^{39}\text{Ar}$, $^{38}\text{Ar}/^{37}\text{Ar}$, and $^{40}\text{Ar}/^{36}\text{Ar}$ chronometry constraints from previous studies (black) and this study (blue). Circles and squares denote ages of matrix glass and clast samples, respectively. Lithologies of clasts are labeled next to each point. Points surrounded by pentagons are interpreted to be primary solidification ages while points surrounded by stars are inferred to be reheating ages. See table S21 for data sources and details. Bottom panel shows inferred geologic events and associated formation and remagnetization times of magnetic records in clasts and the matrix glass.

Table S20. $^{40}\text{Ar}/^{39}\text{Ar}$, $^{40}\text{Ar}/^{36}\text{Ar}$, and $^{38}\text{Ar}/^{36}\text{Ar}$ analyses of breccia 15465.

Lithology	Subsample	Method	Age (Ga)	Event	Reference
Glass	115,6-4-1	$^{40}\text{Ar}/^{39}\text{Ar}$ plateau ¹	0.44 ± 0.01	Glass formation	This study
Glass	115,6-4-1	Trapped $^{40}\text{Ar}/^{36}\text{Ar}$ ²	$0.56^{+0.83}_{-0.56}$	Glass formation	This study
Glass	115,6-4-1	^{38}Ar CRE data ³	0.43 ± 0.01	Glass exposure	This study
Clast	115,6-2	$^{40}\text{Ar}/^{39}\text{Ar}$ plateau ⁴	>3.39	Clast formation	This study
Glass	Unknown	$^{40}\text{Ar}/^{39}\text{Ar}$ ⁵	$>1.09?$	Glass formation	(98)
Clasts (feldspar in basalt)	7	$^{40}\text{Ar}/^{39}\text{Ar}$ isochron ⁶	>1.9	Clast formation	(55)
Clasts (mesostasis of basalt)	7	$^{40}\text{Ar}/^{39}\text{Ar}$ isochron ⁶	1.0 ± 0.5	Clast reheating	(55)
Clasts (highland basalt, norite, glass spheres and fragments)	7	$^{40}\text{Ar}/^{39}\text{Ar}$ isochron ⁶	3.91 ± 0.04	Clast formation	(55)
?	89	Trapped $^{40}\text{Ar}/^{36}\text{Ar}$ ⁷	$1.92^{+0.52}_{-0.59}?$	Glass formation	(22, 41)
Best estimate for glass formation and breccia assembly ⁸			0.44 ± 0.01		

Notes: The first column lists the lithology, the second column lists the 15465 subsample identity, the third column lists the dating method, the fourth column lists the inferred radiometric, cosmic ray exposure (CRE), or model age, the fourth column lists the inferred event being dated, and the fifth column lists the reference. Shaded data are considered to provide the most robust constraints on the date of formation and magnetic field constraint from the matrix glass and baked portions of clast. Uncertainties in new Ar ages reported in this study are 1- σ confidence intervals.

¹Mean $^{40}\text{Ar}/^{39}\text{Ar}$ plateau age over ~6-87% of released ^{39}Ar .

²Ordinate-intercept in plot of $^{40}\text{Ar}/^{36}\text{Ar}$ versus $^{39}\text{Ar}/^{36}\text{Ar}$ for linear regression to data points with $^{39}\text{Ar}/^{36}\text{Ar}$ values below 0.8. Uncertainties consider those associated with calibration of time versus trapped $^{40}\text{Ar}/^{36}\text{Ar}$ [see equation (S15)] as well as in measurements of the trapped $^{40}\text{Ar}/^{36}\text{Ar}$ value.

³Mean ^{38}Ar CRE age over ~6-84% of released ^{37}Ar .

⁴Mean $^{40}\text{Ar}/^{39}\text{Ar}$ plateau age over ~56-100% of released ^{37}Ar .

⁵No detailed data are reported in this study. Therefore, we do not consider this value as a robust constraint on the matrix glass formation.

⁶Laser probe bulk isochron.

⁷Uncertainties consider those associated with calibration of time versus trapped $^{40}\text{Ar}/^{36}\text{Ar}$ [see equation (S15)] as well as $\pm 30\%$ uncertainty in measured trapped $^{40}\text{Ar}/^{36}\text{Ar}$ value. Because the latter was estimated in the absence of $^{39}\text{Ar}/^{36}\text{Ar}$ measurements on the same subsample, the correction for in situ radiogenic ^{40}Ar is unknown and so these uncertainties are likely underestimates.

⁸Mean of three shaded dates weighted by the inverse of the square of the uncertainties (71).

Table S21. $^{40}\text{Ar}/^{39}\text{Ar}$, $^{40}\text{Ar}/^{36}\text{Ar}$, and $^{38}\text{Ar}/^{36}\text{Ar}$ analyses of breccia 15015.

Lithology	Subsample	Method	Age (Ga)	Event	Reference
Glass	229b1	$^{40}\text{Ar}/^{39}\text{Ar}$ steps ¹	1.1 ± 0.6	Glass formation	This study
Glass	229b1	Trapped $^{40}\text{Ar}/^{36}\text{Ar}$ ²	$0.82^{+0.19}_{-0.18}$	Glass formation	This study
Clast	229a1a	$^{40}\text{Ar}/^{39}\text{Ar}$ initial steps ³	>0.56	Clast reheating	This study
Glass	15,23c & 15,26	$^{40}\text{Ar}/^{39}\text{Ar}$ isochron ⁴	1.0 ± 0.2	Glass formation	(57)
Glass	15,23c & 15,26	Trapped $^{40}\text{Ar}/^{36}\text{Ar}$ ⁵	0.91 ± 0.20	Glass formation	(57)
Clast (variolithic basalt)	15,5b	$^{40}\text{Ar}/^{39}\text{Ar}$ and ^{38}Ar CRE data ⁶	<2.6	Breccia assembly	(57)
Clast (variolithic basalt)	15,5b	$^{40}\text{Ar}/^{39}\text{Ar}$ high- T ⁷	>3.4	Clast crystallization	(57)
Clast (Fra Mauro basalt)	15,23b	$^{40}\text{Ar}/^{39}\text{Ar}$ high- T ⁷	>3.7	Clast crystallization	(57)
?	67	Trapped $^{40}\text{Ar}/^{36}\text{Ar}$ ⁸	$0.50 \pm ?$	Glass formation	(22, 40)
Best estimate for glass formation and breccia assembly ⁹			0.91 ± 0.11		

Notes: The first column lists the lithology, the second column lists the 15015 subsample identity, the third column lists the dating method, the fourth column lists the inferred radiometric, cosmic ray exposure (CRE), or model age, the fourth column lists the inferred event being dated, and the fifth column lists the reference. Shaded data are considered to provide the most robust constraints on the date of formation and magnetic field constraint from the matrix glass. Uncertainties in new Ar ages reported in this study are 1- σ confidence intervals.

¹Grand mean $^{40}\text{Ar}/^{39}\text{Ar}$ age calculated from mean of ages calculated over 0-8% of released ^{39}Ar and mean of last 43-100% of released ^{39}Ar . Uncertainty is taken as equal to half the age difference between these two mean ages.

²Ordinate-intercept in plot of $^{40}\text{Ar}/^{36}\text{Ar}$ versus $^{39}\text{Ar}/^{36}\text{Ar}$ for linear regression to data points with $^{39}\text{Ar}/^{36}\text{Ar}$ values below 0.006. Uncertainties consider those associated with calibration of time versus trapped $^{40}\text{Ar}/^{36}\text{Ar}$ [see equation (S15)] as well as in measurements of the trapped $^{40}\text{Ar}/^{36}\text{Ar}$ value.

³Mean of ⁴⁰Ar/³⁹Ar ages over first 15% of released ³⁹Ar.

⁴Mean age for two glass subsamples, with uncertainty equal to half the age difference between these ages.

⁵Uncertainties consider those associated with calibration of time versus trapped ⁴⁰Ar/³⁶Ar [see equation (S15)] as well as in measurements of the trapped ⁴⁰Ar/³⁶Ar value.

⁶Upper limit on breccia assembly age computed by subtracting ³⁸Ar CRE age of 0.8 Gy from ⁴⁰Ar/³⁹Ar age of 3.4 Ga inferred from high-temperature steps [see discussion in ref. (57)].

⁷Range of ⁴⁰Ar/³⁹Ar ages calculated over ~80-100% of released ³⁹Ar.

⁸Because this trapped ⁴⁰Ar/³⁶Ar was estimated in the absence of ³⁹Ar/³⁶Ar measurements on the same subsample, the correction for ⁴⁰Ar is uncertain and these uncertainties are difficult to quantify.

⁹Mean of four shaded dates weighted by the inverse of the square of the uncertainties (71).

Table S22. Modern paleointensity analyses of Apollo samples.

Sample	Age (Ga)	±1σ (Ga)	Paleointensity (μT)	1σ (Ga)	Method	Ref.
76535	4.249	0.012	40	-20/+40	ARM/IRM	(7)
71505 ¹	3.7	0.1	95	-48/+95	ARM/IRM	(5)
71567 ²	3.8	0.1	111	-56/+111	ARM/IRM	(5)
70017 ³	3.772	0.0145	42	-21/+42	ARM/IRM	(5, 100)
10020	3.706	0.013	66	-33/+66	ARM/IRM	(4)
10017 ⁴	3.297	0.260	71	-36/+71	ARM/IRM	(50)
10049	3.556	0.008	77	-39/+71	ARM/IRM	(50)
60015	< 3.34		< 5		ARM/IRM Thermal	(35)
15597	3.3	0.2	< 7		ARM/IRM	(8)
15556	3.233	0.007	< 75		ARM/IRM	(25, 46)
15016	3.281	0.008	< 37		ARM/IRM	(25, 46)
12017 basalt	3.345	0.005	< 37		ARM/IRM	(10)
12022	3.194	0.025	< 4		ARM/IRM	(8)
						(9)
15498	1.47	0.45	5	±2	ARM/IRM Thermal	This study
15015	0.91	0.11	< 0.08		Thermal	This study
15465	0.44	0.01	< 0.06		Thermal	This study
12017 glass	< 0.007		< 7		ARM/IRM	(10)

Notes: The first column lists the Apollo sample, the second column lists the NRM age as inferred from ⁴⁰Ar/³⁹Ar chronometry, the third column lists 1-σ age confidence interval, the fourth column lists paleointensity, the fifth column lists 1-σ paleointensity confidence interval, and the sixth column lists the paleointensity method and the seventh column lists the reference for the age and paleointensity data.

¹This sample has not been radiometrically dated. Because it is a Apollo 17 type B basalt (101), its age is assigned based on published radiometric ages for other Type B basalts (100, 102).

²This sample has not been radiometrically dated. Because it is a Apollo 17 type A basalt (19), its age is assigned based on published radiometric ages for other Type B basalts (100, 102).

³Using age of ref. (103) as recalculated by ref. (100)

⁴Minimum age is measured 10017 plateau age and maximum age is plateau age of similar sample 10049.

The end of the lunar dynamo

Saied Mighani, Huapei Wang, David L. Shuster, Cau? S. Borlina, Claire I. O. Nichols and Benjamin P. Weiss

Sci Adv **6** (1), eaax0883.

DOI: 10.1126/sciadv.aax0883

ARTICLE TOOLS

<http://advances.sciencemag.org/content/6/1/eaax0883>

SUPPLEMENTARY MATERIALS

<http://advances.sciencemag.org/content/suppl/2019/12/20/6.1.eaax0883.DC1>

REFERENCES

This article cites 86 articles, 10 of which you can access for free
<http://advances.sciencemag.org/content/6/1/eaax0883#BIBL>

PERMISSIONS

<http://www.sciencemag.org/help/reprints-and-permissions>

Use of this article is subject to the [Terms of Service](#)

Science Advances (ISSN 2375-2548) is published by the American Association for the Advancement of Science, 1200 New York Avenue NW, Washington, DC 20005. The title *Science Advances* is a registered trademark of AAAS.

Copyright © 2020 The Authors, some rights reserved; exclusive licensee American Association for the Advancement of Science. No claim to original U.S. Government Works. Distributed under a Creative Commons Attribution NonCommercial License 4.0 (CC BY-NC).